

REPORT DOCUMENTATION PAGE

Form Approved OMB No. 0704-0188

Public reporting burden for this collection of information is estimated to average 1 hour per response, including the time for reviewing instructions, searching existing data sources, gathering and maintaining the data needed, and completing and reviewing the collection of information. Send comments regarding this burden estimate or any other aspect of this collection of information, including suggestions for reducing this burden to Washington Headquarters Services, Directorate for Information Operations and Reports, 1215 Jefferson Davis Highway, Suite 1204, Arlington, VA 22202-4302, and to the Office of Management and Budget, Paperwork Reduction Project (0704-0188), Washington, DC 20503.

1. AGENCY USE ONLY (Leave blank)		2. REPORT DATE August 1997	3. REPORT TYPE AND DATES COVERED Final Report	
4. TITLE AND SUBTITLE Cryogenic Aluminum Armature Bar For High Power Generators			5. FUNDING NUMBERS F6170896W0294	
6. AUTHOR(S) Dr Lidia Chubraeva				
7. PERFORMING ORGANIZATION NAME(S) AND ADDRESS(ES) Institute for Electrotechnical Problems (NIIElectromash) Moskovsky av., 100 St Petersburg 196084 Russia			8. PERFORMING ORGANIZATION REPORT NUMBER N/A	
9. SPONSORING/MONITORING AGENCY NAME(S) AND ADDRESS(ES) EOARD PSC 802 BOX 14 FPO 09499-0200			10. SPONSORING/MONITORING AGENCY REPORT NUMBER SPC 96-4082	
11. SUPPLEMENTARY NOTES				
12a. DISTRIBUTION/AVAILABILITY STATEMENT Approved for public release; distribution is unlimited.			12b. DISTRIBUTION CODE A	
13. ABSTRACT (Maximum 200 words) This report results from a contract tasking Institute for Electrotechnical Problems (NIIElectromash) as follows: The contractor shall fabricate an aluminum cryogenic armature bar for high power generators, fabricate a specialized test fixture for evaluation of the armature bar and assemble the armature bar in the test fixture and test in approp cryogens to determine performance at a variety of temperatures. Test currents and voltages shall be applied to the armature and losses will be determined for ohmic and eddy current. Contractor shall deliver the test bar to EOARD, UK.				
14. SUBJECT TERMS Physics			15. NUMBER OF PAGES 93	
			16. PRICE CODE N/A	
17. SECURITY CLASSIFICATION OF REPORT UNCLASSIFIED	18. SECURITY CLASSIFICATION OF THIS PAGE UNCLASSIFIED	19. SECURITY CLASSIFICATION OF ABSTRACT UNCLASSIFIED	20. LIMITATION OF ABSTRACT UL	

19971002 136

**Institute of Electrotechnical Problems
Department of Non-Conventional Electrical Machines
St.-Petersburg, Russia**

**CRYOGENIC ALUMINUM ARMATURE BAR
FOR HIGH POWER GENERATORS**

Contract Number F6170896W0294 (SPC-96-4082)

Final Report

August 1997

By:

L.I.Chubraeva

**D.V.Sirotko
V.A.Tutaev
A.V.Kalmykov
I.N.Popov**

**V.B.Bakhmetjev
Ju.B.Kurshinsky
L.N.Bogojavlenskaja
E.N.Mezentseva**

**Prepared for
Department of Air Force
USA**

CONTENTS

Introduction.....	3
1. Fabrication of a helical winding model with continuously wound phases.....	5
1.1. Losses in electrical joints of a helical armature winding.....	5
1.2. Co-relation of the losses in the bars and electrical joints at cryogenic temperatures.....	7
1.3. Design and main features of the winding model.....	9
2. Experimental investigation of the armature winding model...	15
2.1. High-voltage tests of model winding and resistance tests.....	15
2.2. Investigation of the 3D magnetic field distribution.....	18
3. Fabrication of aluminum cryogenic armature bar and test fixture for the Contract delivery.....	25
3.1. Fabrication of the armature bar of composite high-purity aluminum wires and control of short-circuits.....	25
3.2. Fabrication of armature bar versions manufactured of copper and high-purity aluminum wires.....	30
3.3. Description of the armature of the high-speed electrical generator.....	32
3.4. Description of the delivery test fixture.....	34
4. Experimental investigation of cylindrical model with the bars.....	38
4.1. Principles of the cooling scheme being investigated.....	38
4.2. Test-bed configuration.....	41
4.3. Experimental investigation of the armature bars at cryogenic temperatures.....	48
5. Experimental investigation of the disc model bars.....	63
5.1. Specific features of heat conduction in multifilamentary wires..	63
5.2. Armature bar cooling by means of heat conductivity.....	68
5.3. Researches of a thermal behavior of aluminum armature bar for at pulse loads of different shape.....	82
Conclusion.....	91
References.....	93

INTRODUCTION

Development of an armature, composed of the wires with low electrical resistance (hyperconducting or superconducting) for high power cryogenic generator is associated with several main problems. Decrease of the total amount of electrical losses in the winding is one of them. These losses incorporate the Ohmic, eddy current and circulating current ones. Application of the helical winding geometry allows to decrease the Ohmic and eddy losses due to decreased volume of the wires as compared to other winding geometries like conventional lap or saddle-shaped. Application of composite high-purity aluminum wires with small diameter of individual filaments results in still lower eddy-current losses. The circulating currents within the composite wires are relatively low due to double twist of the elementary filaments and high electrical resistivity of the matrix material. The circulating currents within the armature bar are suppressed by a special transposing of the composite wires. The problem was under investigation in the previous contract with EOARD (Contract Number F61700894WO769). As a result there was developed an aluminum armature bar with high current density and low eddy losses at high current frequency.

Initially the helical armature winding is composed of individual bars, soldered with each other at both ends of the winding. The losses in electrical joints may be relatively high, thus decreasing the total efficiency of the generator. The losses in the low-temperature winding may be lower if the number of these electrical joints is decreased. In the above mentioned work there was proposed the helical winding manufacturing technology with only one half of the amount of electrical connections as compared with initial helical winding. It comes now clear that a still better technological process may be developed, which is extremely important for both hyperconducting and superconducting windings.

A new model armature winding was manufactured, based on new technological process. The winding has continuously wound phases and no electrical joints on the total phase length. As a result still lower electrical losses may be obtained due to both improved electrical resistance of the cryogenic winding and absence of eddy-current losses in the soldered end-clips.

To study electrical and thermal behavior of the cryogenic aluminum armature bars for high power generators there was developed and tested a fragment of an armature winding with the support structure and four different samples of the armature bars. After electrical tests at cryogenic temperature with loss evaluation the test fixture was delivered to EOARD.

When manufacturing the armature winding of the bars, consisting of a combination of different metals and insulating materials (conducting metal and

matrix metal, wire insulation, epoxy, bar insulation and epoxy, etc.) one is to take into account the difference in thermal conductivity along the bar length and cross-section. As a result it is important to develop the armature bar design, which is optimized not only from the point of view of electrical losses but thermal behavior as well. It is to be based on investigation of heat conductivity of the bar in axial direction along its length. Theoretical calculations were verified by experimental investigations.

High power electrical generator is often operating in a pulse load mode. It is therefore important to evaluate the behavior of high-purity aluminum bars in case they are loaded by a pulse current. The results of experimental investigations will allow to develop an alternator with minimized size and mass parameters.

1. FABRICATION OF A HELICAL WINDING MODEL WITH CONTINUOUSLY WOUND PHASES

1.1. Losses in electrical joints of a helical armature winding

One of the disadvantages of a helical armature winding technology is necessity of armature bar electrical connection at the end clips. It is less serious in case of copper winding operating at ambient temperature, but it comes out to be a problem if the winding is manufactured of a wire with low electrical resistance: hyperconducting or superconducting one. Increased quantity of electrical joints may influence substantially the final value of electrical resistance of the armature winding phase, thus resulting in increased Ohmic losses. Moreover the very connection itself is a source of increased eddy losses as it is subjected to the influence of components of magnetic field (Fig.1.1,a).

As the axial component of magnetic field in the end clip zone is negligibly small, only two components B_x and B_y are being discussed. The eddy current losses caused by these components may be determined as:

$$P_e^y = \frac{1}{24} B_y^2 \gamma \omega^2 b^2 V, \quad (1.1)$$

$$P_e^x = \frac{1}{24} B_x^2 \gamma \omega^2 h^2 V, \quad (1.2)$$

the sum of the losses equals

$$P_e = \frac{\gamma \omega^2}{24} (B_x^2 h^2 + B_y^2 b^2) V_j \quad (1.3)$$

with γ - specific electric conductivity of the joint material,

ω - current frequency,

$V = b_j h_j l_j$ - volume of the joint,

$h_j = 2h$, h - thickness of the armature bar.

In conventional helical winding the amount of electrical connections on both sides of the armature equals (Fig.1.1,b)

$$N_c = z + 2m, \quad (1.4)$$

where z - number of armature bars in both layers of the winding, m - number of phases in the armature winding.

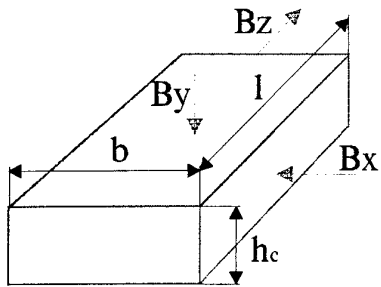


Fig.1.1,a. Schematic geometry of electrical joint.

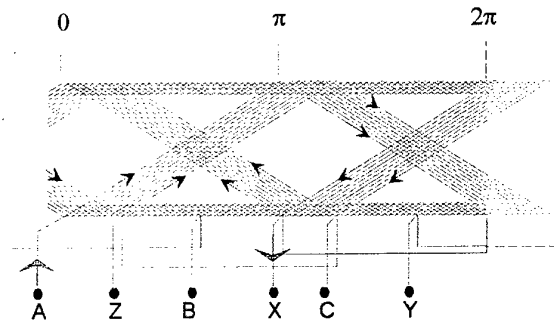


Fig.1.1,b. Electrical scheme of a helical winding.

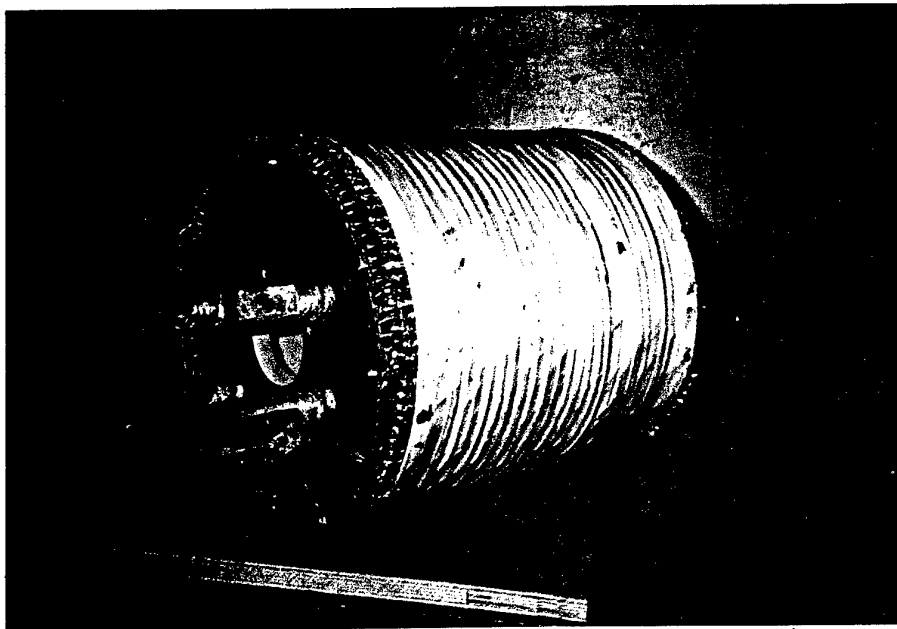


Fig. 1.2. Helical armature winding model with decreased amount of interphase joints.

The researches carried out in the previous contract with EOARD (Contract Number F61700894WO769) allowed to develop and test an improved version of a helical armature winding, whose end clip connections were decreased in 2 times (the winding model is presented in Fig.1.2):

$$N_c = (z+2m)/2 . \quad (1.5)$$

It means the total amount of eddy-current losses in electrical joints equals approximately ($z \gg m$) either

$$P_{\Sigma c} = P_c z , \quad (1.6)$$

or

$$P_{\Sigma c} = P_c z / 2 . \quad (1.7)$$

Now a new step is being proposed which allows to have minimal number of interphase connections: either in between two semi-phases, or to exclude them along the armature phase length at all. It means there will be no electrical joints between the individual armature bars or loops and no increased size of electrical connection itself at the end clip.

The winding is to be manufactured of rigid copper wires and it represents a new step in developing the technology applicable not only for the multifilamentary strands, but for the rigid HTSC wire.

1.2. Co-relation of the losses in the bars and electrical joints at cryogenic temperatures

The losses in the armature winding consist of the three components: Ohmic losses, eddy current losses and circulating current losses. They may be subdivided into two components: losses in the armature bars and losses in electrical joints. (The latter are described in Para 1.1.).

Assuming zero circulating current losses, we obtain for the Ohmic losses in the bar and in the joint:

$$P_{ob} = j_b^2 \tilde{\rho}_b V_b , \quad (1.8)$$

$$P_{oj} = j_j^2 \rho_j V_j . \quad (1.9)$$

Taking into account that

$$j_j = j_b \frac{S_b}{S_j}, \quad V_j = S_j l_j, \quad V_b = S_b l_b \quad (1.10)$$

and assuming on the first stage that

$$\rho_j = \rho_e = \rho; \quad (1.11)$$

we have

$$P_{ob} = j_b^2 \rho V_b, \quad (1.12)$$

$$P_{oj} = j_b^2 \frac{S_b^2}{S_j^2} \rho V_j, \quad (1.13)$$

$$l_b = \frac{l_b^*}{\sin \alpha} = \frac{l_b^*}{\sin \frac{b}{t}}, \quad (1.14)$$

t - twist pitch,

and co-relation of Ohmic losses in the joint and in the bar equals

$$\frac{P_{oj}}{P_{ob}} = \frac{S_b l_j}{S_j l_b}. \quad (1.15)$$

The co-relation of eddy current losses may be presented as:

$$P_{eb} = \frac{1}{32} \gamma \omega^2 d^2 V_b (B_{xb}^2 + B_{yb}^2 + B_{zb}^2), \quad (1.16)$$

$$P_{ej} = \frac{1}{24} \gamma \omega^2 V_j (B_{yj}^2 b^2 + B_{xj}^2 h^2), \quad (1.17)$$

$$\frac{P_{ej}}{P_{eb}} = \frac{3 S_j l_j (B_{yj}^2 b^2 + B_{xj}^2 h^2)}{4 S_b l_b d^2 (B_{xb}^2 + B_{yb}^2 + B_{zb}^2)}. \quad (1.18)$$

In the case of the considered high-purity armature bars and helical armature winding of the 5 MVA class high-speed alternator we have the following correlation of the losses:

$$\frac{P_{oj}}{P_{ob}} \cdot 100 \% = 6 \% , \tag{1.19}$$

$$\frac{P_{ej}}{P_{eb}} \cdot 100 \% = 184 \% .$$

Taking into account the optimal relation between the Ohmic and eddy losses at cryogenic temperatures we then obtain that the losses an the joints are equal to at least

$$\sum P_j = \frac{184+6}{2} \sum P_b = 95 \% \sum P_b , \tag{1.20}$$

being a substantial part of the total losses in the armature winding.

It explains serious attention which is being paid to the problem of continuous winding laying down without subdividing it into individual bars.

1.3. Design and main features of the winding model

To develop the design of helical winding with continuously wound phases and to try out the technological process of its manufacturing the model winding was fabricated. The initial wire was a rigid copper one, with limited bending radius, to make the new technological process applicable for both superconductors, especially the high-temperature ones, and high-purity aluminum. Since such a winding has no soldered electrical joints, its resistance is lower and the losses inherent for these joints are absent.

The major distinction of model helical winding manufacturing is locating the bars on the outer and inner surfaces of the support structure. This design improves drastically cooling of the bars compared with the original helical winding having reduced number of interturn connections, where the lower layer bars were cooled by means of coolant flowing along the axial ducts made in the support structure and between the winding layers. Thanks to the absence of axial cooling ducts the winding manufacturing technology is significantly simplified. Figure 1.3 shows schematically the main difference in the end clip design for a helical winding

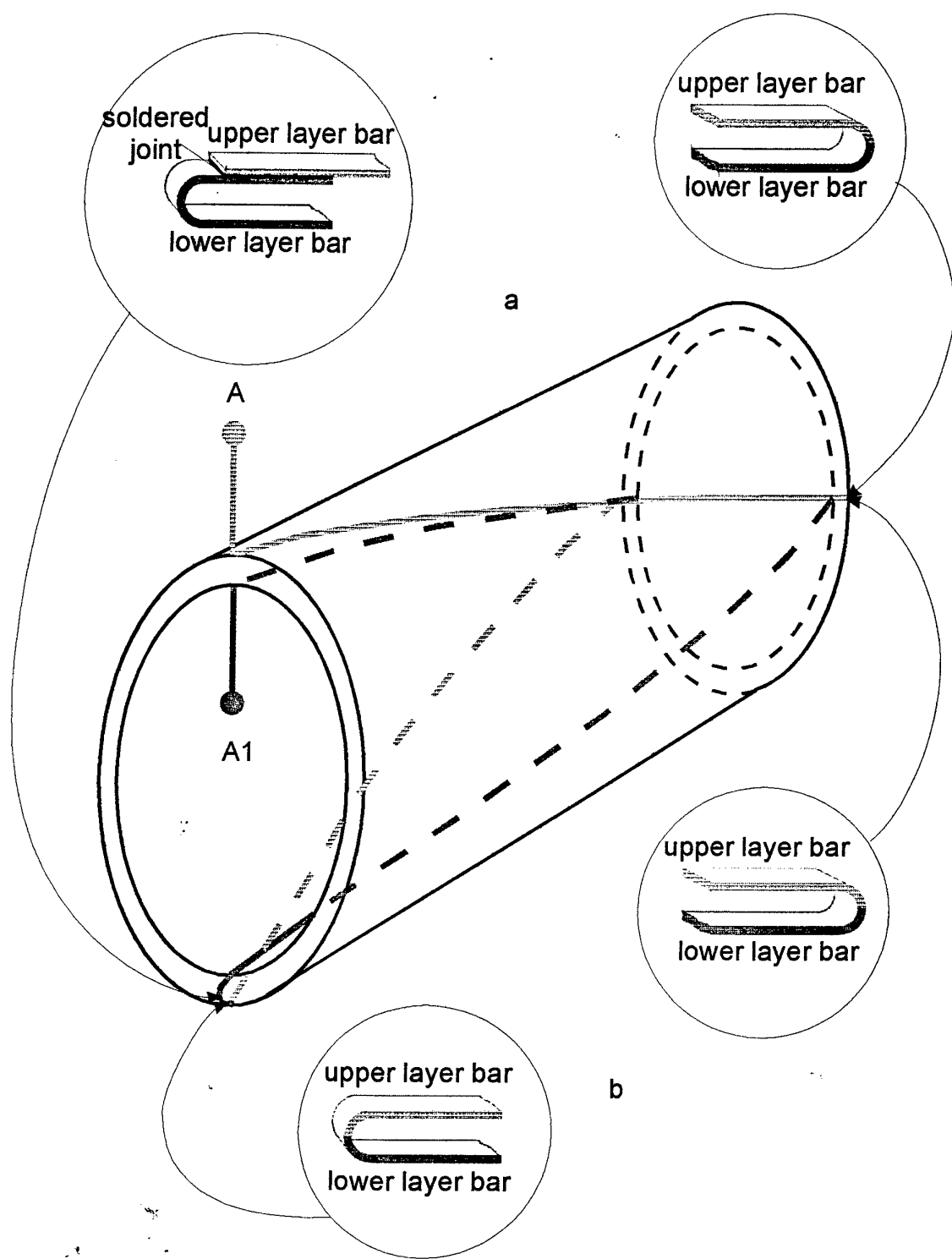


Fig. 1.3. Schematic view of the end clip for the initial helical winding (a) and for a proposed new technology (b).

having reduced number of interturn connections and a helical winding with continuous phase winding process.

Another feature of the proposed winding is the absence of soldered joints, what makes its manufacturing process easier and gives the opportunity to employ mechanization of some operations when laying the bars. Moreover, the winding insulating properties are improved due to no interturn solders and additional insulation barriers in the area of soldered joints are no longer needed.

Support structure of the winding is a cylinder of pressed paper manufactured by means of technology that provides high mechanical strength comparable to that of a glass-cloth-base laminate. It is as well reasonable to employ paper as a support structure material from the viewpoint of possibility of proper impregnating the whole winding with epoxy compound. The support structure thickness is to be chosen in accordance with the minimum bending radius of winding conductor; for the winding presented it is 11 mm. Two ring-shaped templates were fabricated for winding bar laying in; these rings had axial slots made on their outer and inner surfaces for laying upper layer and lower layer bars correspondingly. Radial slots on ring end faces made it possible to make transitions between the winding layers and to secure the turns during the winding process. The number of slots on each ring-shaped template is equal to the total number of winding turns. At the opposite end faces of the ring-shaped templates there were the ring-shaped grooves giving the opportunity to center the templates relatively to the support structure. The rings are fastened to the support structure with cold-hardening epoxy compound.

The current-carrying element was a single-filament copper conductor with 7.1 mm^2 cross-section in cotton insulation. Electrical scheme of the manufactured winding is presented in Fig.1.4.

During the phase winding down, after each group of turns with their number equal to the number of poles has been laid, it was necessary to make transition from one winding layer to another with a shift to the next slot (in our case the winding was a cross-over one). In order to do this with minimum bending of the conductor some radial teeth in the ring located on the side of winding leads were removed. The number of removed teeth in each phase was:

$$Z_u = \frac{N_a}{p} - 2, \quad (1.21)$$

where N_a - stands for the number of phase turns connected in series, and p - for the number of pole pairs.

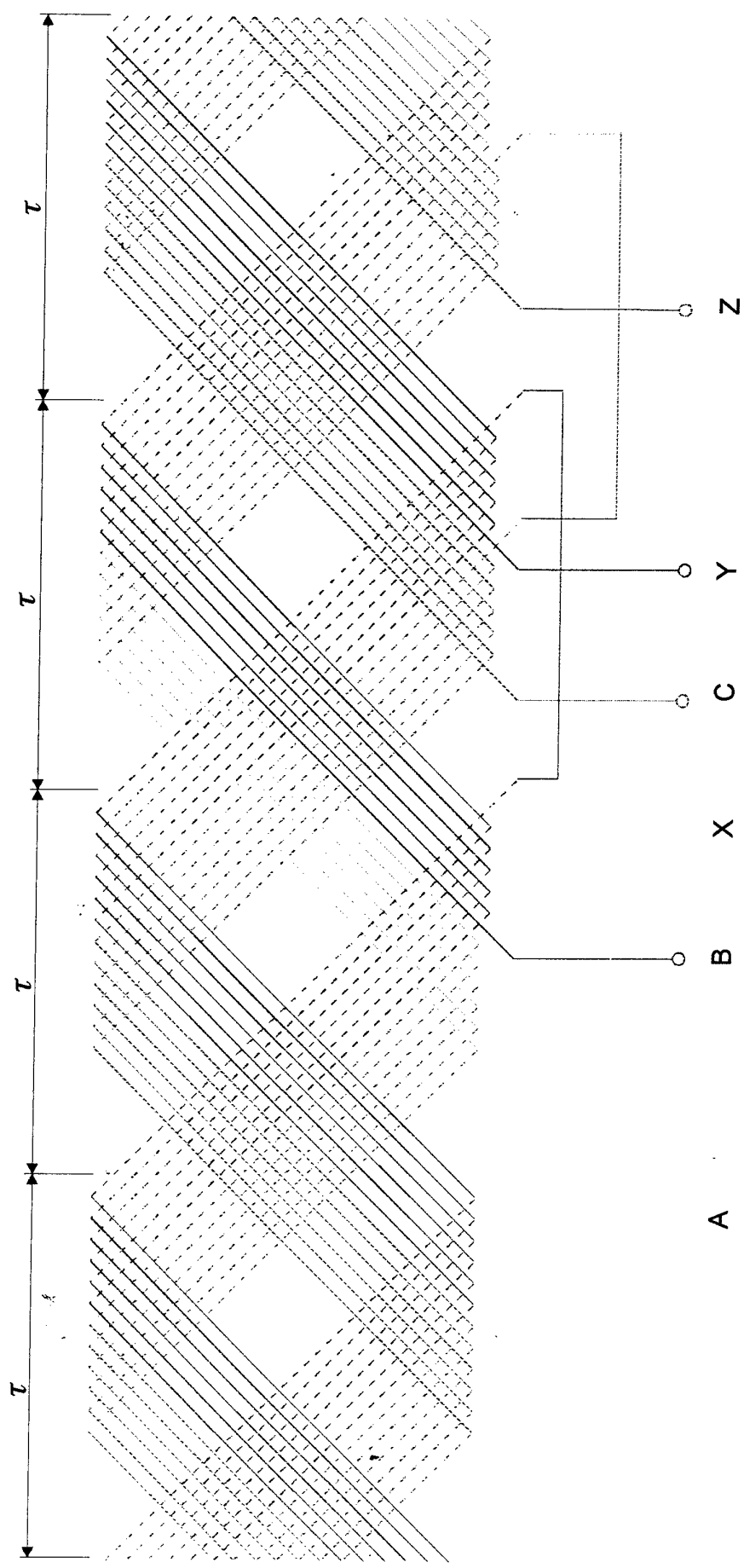


Fig. 1.4. Electrical scheme of model helical winding with continuously wound phases.

For winding of each phase a special shuttle was produced, onto which a phase wire was wound. In the manufactured winding the length of phase wire was 20 m. Width of the shuttle was determined by conductor cross-section and its admissible bending radius. Shuttle length should be equal to the length of winding semiturn, so that the conductor should not be subjected to additional bending during laying. Shown in Fig.1.5 are the support structure with the ring-shaped templates and the shuttle with the wound phase wire. Figure 1.6 presents the manufactured winding (for better visualization there is no outer bandage on the winding surface). The winding phases are painted in different colors (A - yellow, B - green, C - red) in accordance with the acting Russian Standards.

Main parameters of the helical winding model are given in Table 1-1. It is worth noting here that the developed winding model may be applied in a high-speed alternator of 1-2 MVA class.

Table 1-1

Parameter	Value
Winding outer diameter, m	0.235
Winding inner diameter, m	0.195
Active length, m	0.325
Number of phases	3
Number of poles	4
Number of phase turns connected in series	24
Winding bar cross-section, mm ²	7.1
Support structure weight, kg	1
Weight of winding with support structure, kg	5
Length of phase conductor, m	20
Phase resistance, Ω	55.6×10^{-3}
Phase inductance, H	44×10^{-6}
Maximum deviation of phase resistance, %	3.5
Maximum deviation of phase inductance, %	2.1

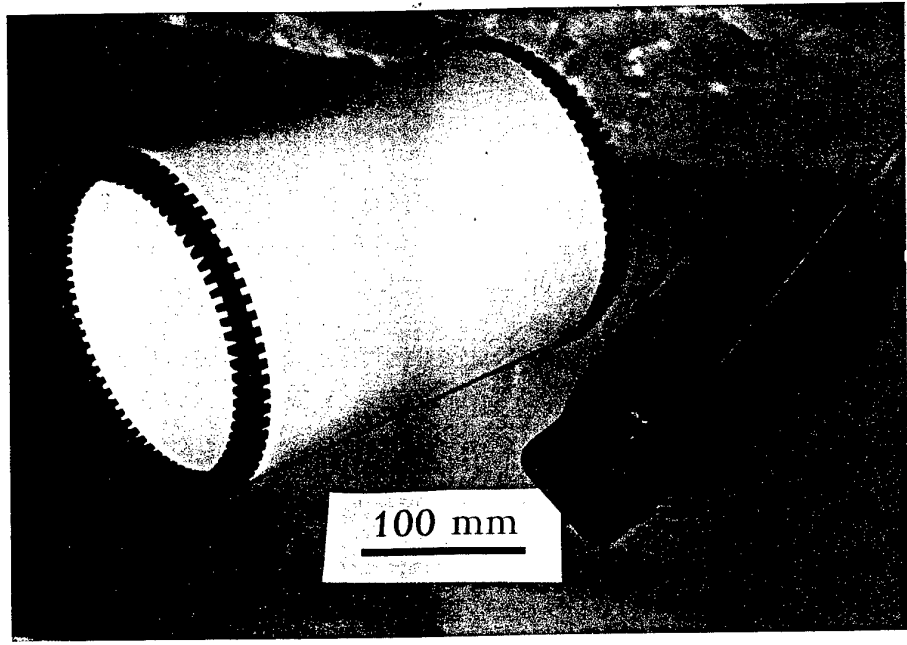


Fig. 1.5. Support cylinder for the model helical winding with the ring templates and the shuttle.

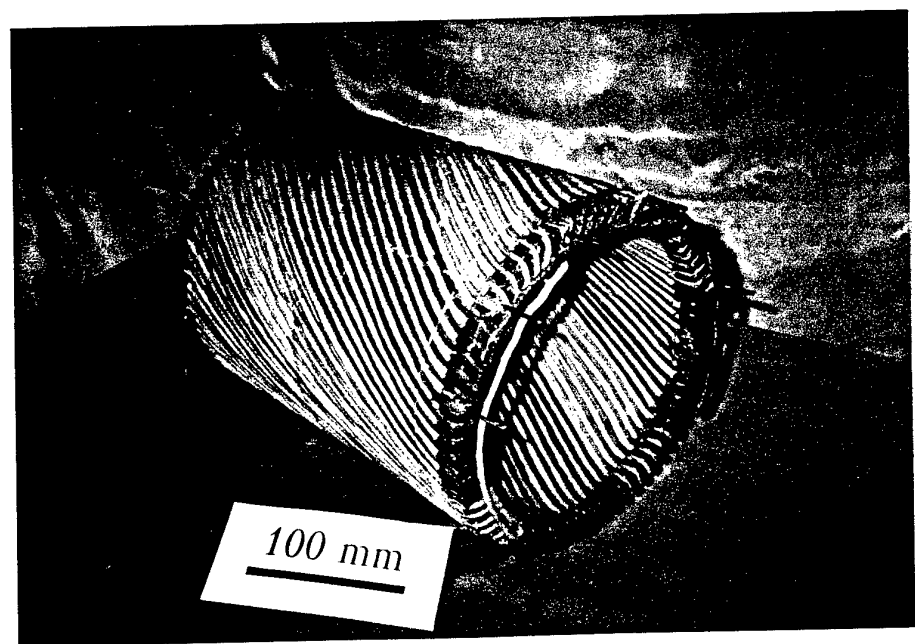


Fig. 1.6. Helical armature winding with continuously wound phases.

2. EXPERIMENTAL INVESTIGATION OF THE ARMATURE WINDING MODEL

2.1. High-voltage tests of model winding and resistance tests

Manufacturing of a model helical winding made it possible to assess the insulating properties of the design and to bring to light its weak points.

First, let us consider insulation gaps and stresses arising in the interphase area inside one layer, since interbar voltage is maximum here. Voltage between the bars in the interphase area is determined through the vector diagram presented in Fig.2.1,a, wherefore it follows that the voltage value between bars of different phases may be written down as:

$$U_{pf} = \sqrt{\frac{3}{2}} U_f = 7.07 \text{ kV}, \quad (2.1)$$

Let us assume the maximum line voltage to be 10 kV. The banding rope impregnated with epoxy compound serves as insulation in the interphase area. The simplified estimation of the maximum field strength can be made using the equation:

$$E_{max} = \frac{0.45 U_{af}}{r \ln \frac{r+0.5S}{r}} \approx 2 \text{ kV/mm}, \quad (2.2)$$

where $r = 3 \text{ mm}$, $S = 9 \text{ mm}$. Computation model is presented in Fig.2.1,b.

The assessed field strength is much lower than the breakdown strength values for epoxy compounds at liquid nitrogen temperatures, which are about 100 - 120 kV/mm.

Similarly, we can determine voltage between the crossing conductors of different layers falling into different phases. This voltage is of the same order. However, since the interlayer insulation comprises the support structure about 11 mm thick and impregnated with epoxy compound it is obvious that the insulation in this area provides pretty well the insulation strength of the winding.

Insulation of the interturn end clip area has the same electric strength margin as the interphase insulation inside one layer, and hence it needs no special consideration.

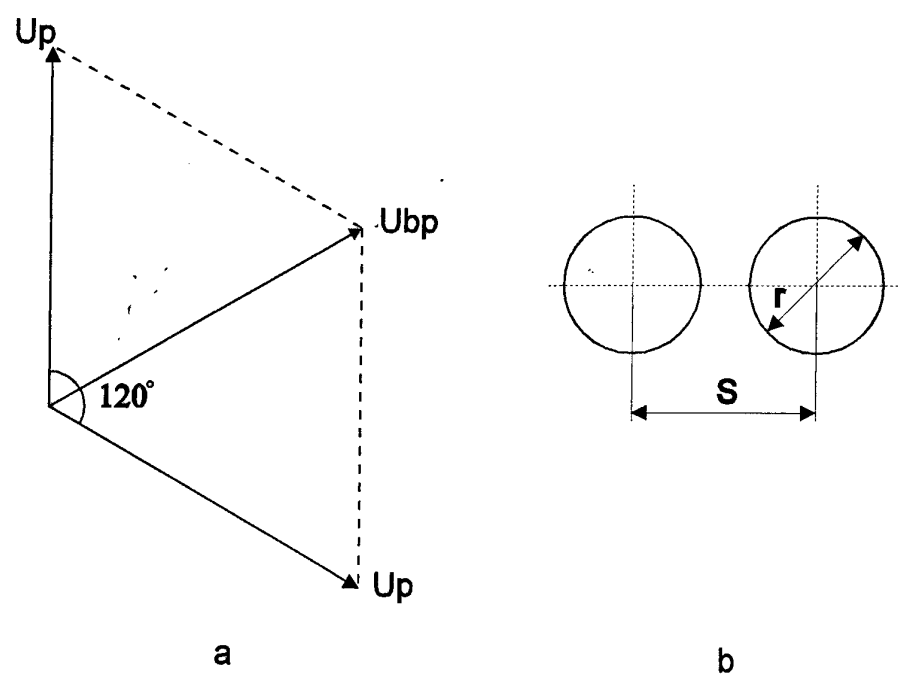


Fig. 2.1. Vector diagram to determine interbar voltage in the interphase area (a), and computation model for obtaining the field strength between the bars of model helical winding (b).

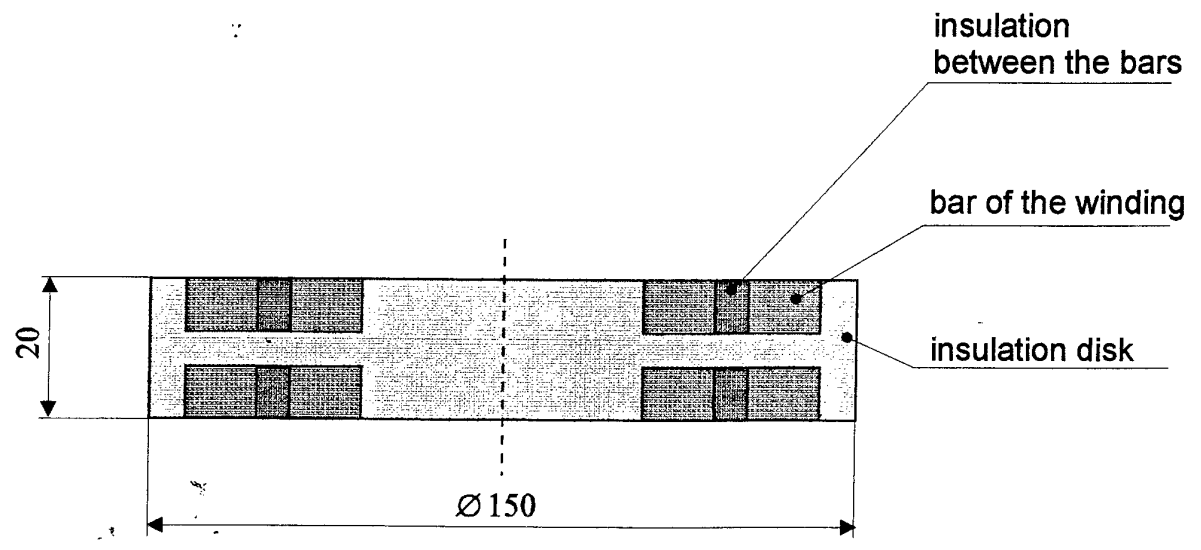


Fig. 2.2. Schematic view of the model for testing the insulation of interphase area inside one layer.

To check the electric strength margin of the manufactured model winding, a mock-up simulating the design features of interphase area inside the layer was produced and tested in liquid nitrogen with high voltage of industrial frequency.

Presented schematically in Fig.2.2 is the model for insulation testing of the interphase area inside one layer. This model was subjected to the voltage equal to double line voltage, i.e. 20 kV. The model sample withstood this voltage during 5 minutes (whereas according to the standard testing time is 1 minute) with no visual signs of corona discharge in liquid nitrogen. Then the voltage was increased to 25 kV and maintained for 1 minute. No symptoms of corona were observed. After that the voltage was raised up to 30 kV, and in 10 seconds there occurred a flash-over. Repeated tests at continuous voltage build-up yielded the same result - flash-over took place at 30 kV, preceded by active corona discharge in liquid nitrogen at 28 kV.

Analysis of flash-over regions showed that the mechanism of flash-over is like this: break-down of thin upper layer of compound above the conductors - intensive corona discharge in liquid nitrogen - transition of liquid nitrogen into gaseous state - break-down of chain of gas bubbles along the lines of field intensity.

Thus, the tests demonstrated:

1. Insulation in the slot area has the required strength margin and withstands the enhanced test voltage $2 U_{pf}$.
2. To improve reliability of insulation system in interphase areas inside the layer it is necessary to make additional insulation barriers projecting above the bar surface.

The tests prove that in the present form the winding model is capable of operating at the voltage of 10 kV, and after the insulation of interphase areas inside the layer is improved the value of operating voltage can be higher. Electrical strength margin can be increased with no substantial changes in winding manufacturing technology, but due to formation of additional insulation barriers above the bar surface.

The electrical resistance measurements were carried out at DC. The winding phases were fed by stabilized DC current. To decrease possible errors electronic millivoltmeter with high entrance resistance was used. The phase inductances were measured by AC bridge with basic frequency 1000 Hz. The result of tests are given in Table 1-1.

2.2. Investigation of the 3D magnetic field distribution

The pattern of winding magnetic field 3-dimensional distribution at 50 Hz frequency was investigated and measured by means of electromagnetic induction transducers. All the relationships were taken at the phase current of 200A and star-type phase connection. Field distribution was determined both along the outer winding surface and along the inner surface. The results of this investigation is presented on Fig.2.3-2.8.

During magnetic field measurements the peripheries of the inner and outer surfaces of the winding were subdivided into 15 parts. On each part the three components were measured along the winding length. To decrease the error from the pick-up signal the electronic millivoltmeter was used with high entrance resistance. Zero point of axial coordinates in the Fig. 2.3-2.8 refers to the terminal side of the winding.

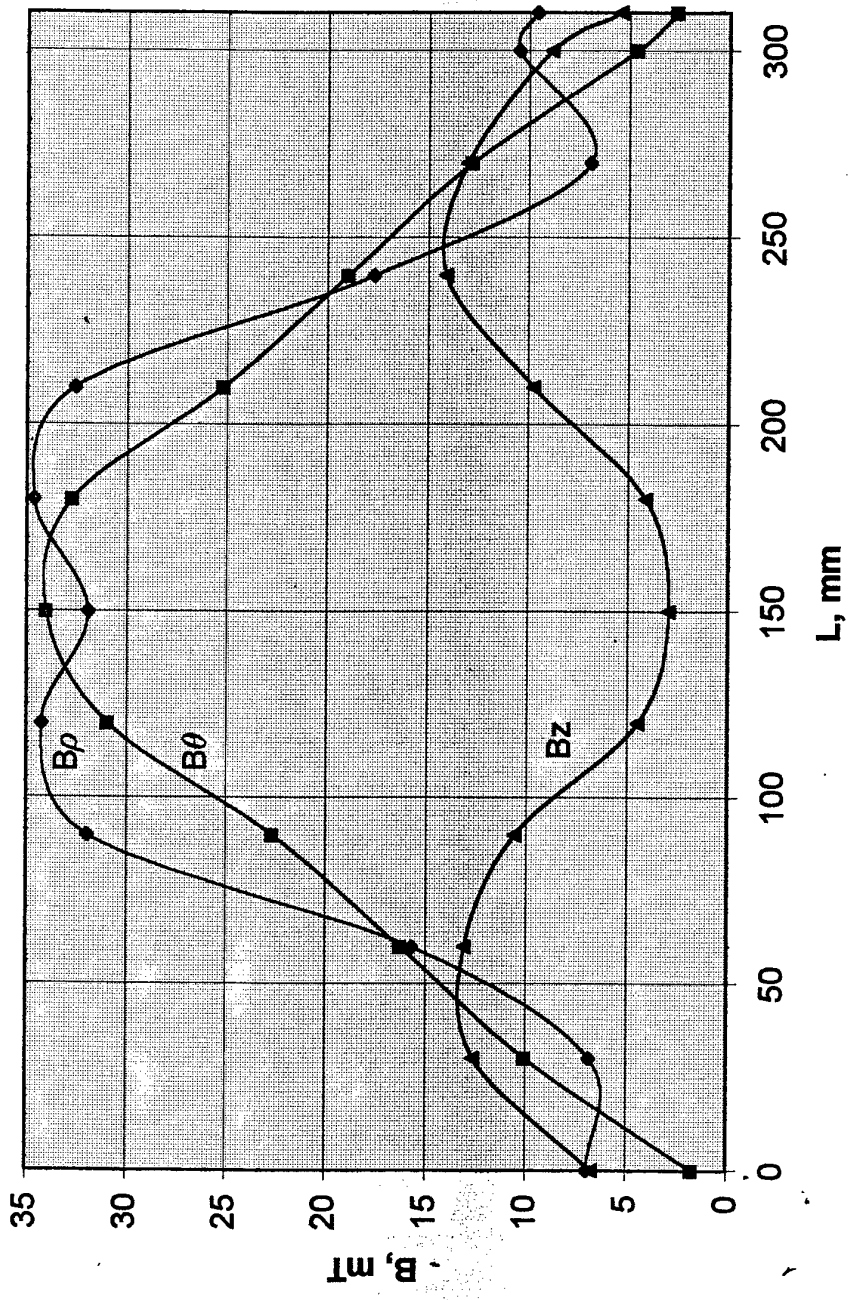


Fig. 2.3. Distribution of magnetic induction along the length of inner surface of helical winding.

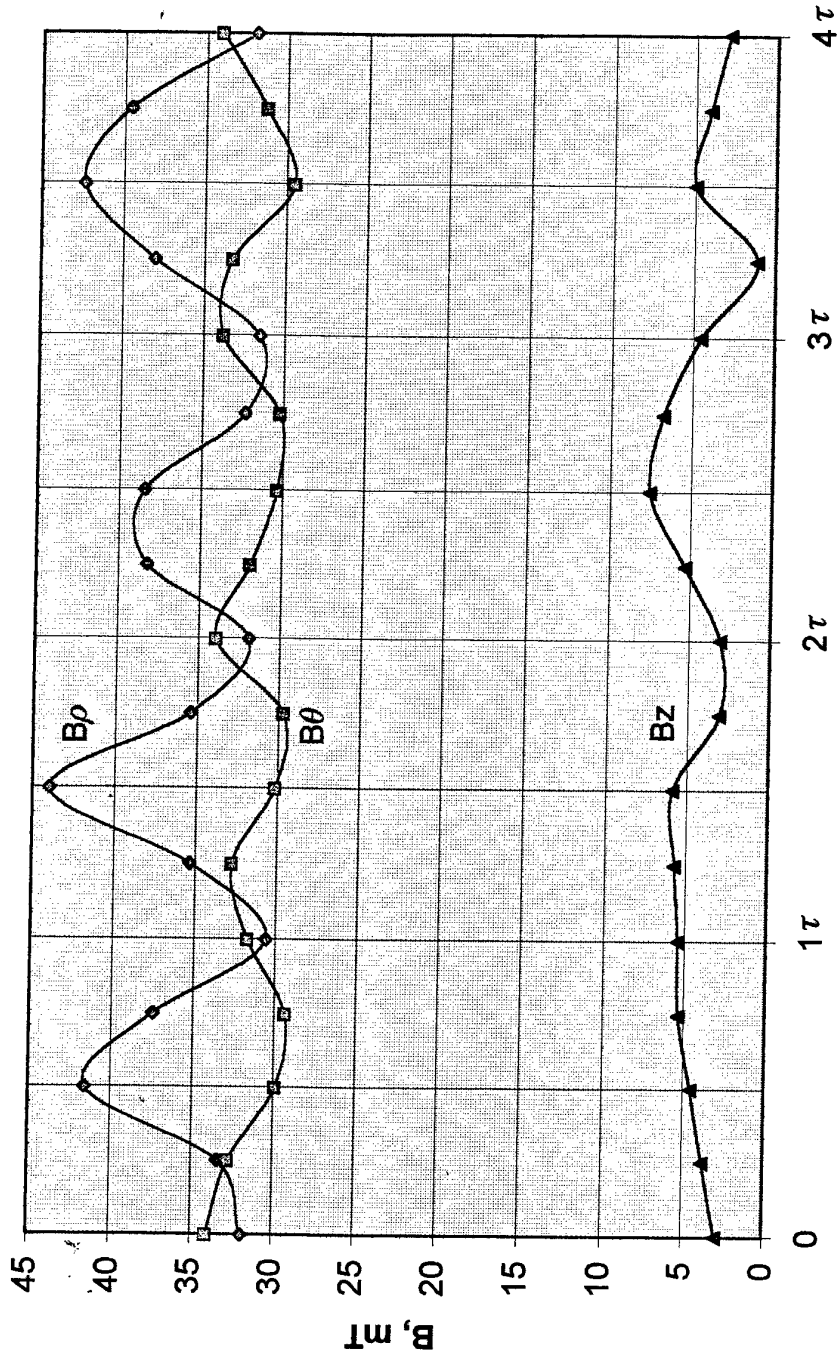


Fig. 2.4. Distribution of magnetic induction on the inner surface of the helical winding.

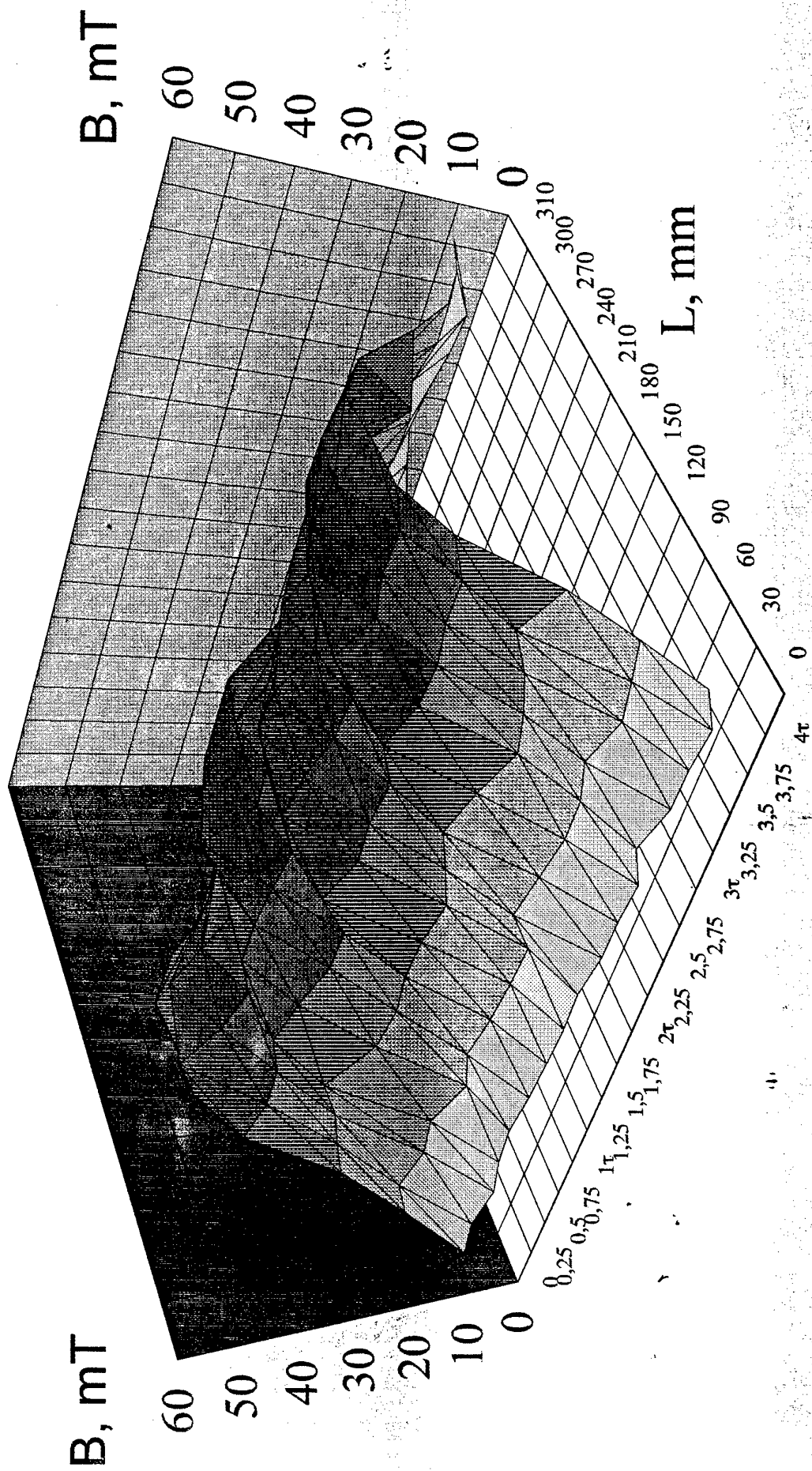


Fig. 2.5. Distribution of 3D magnetic induction on the inner surface of helical winding.

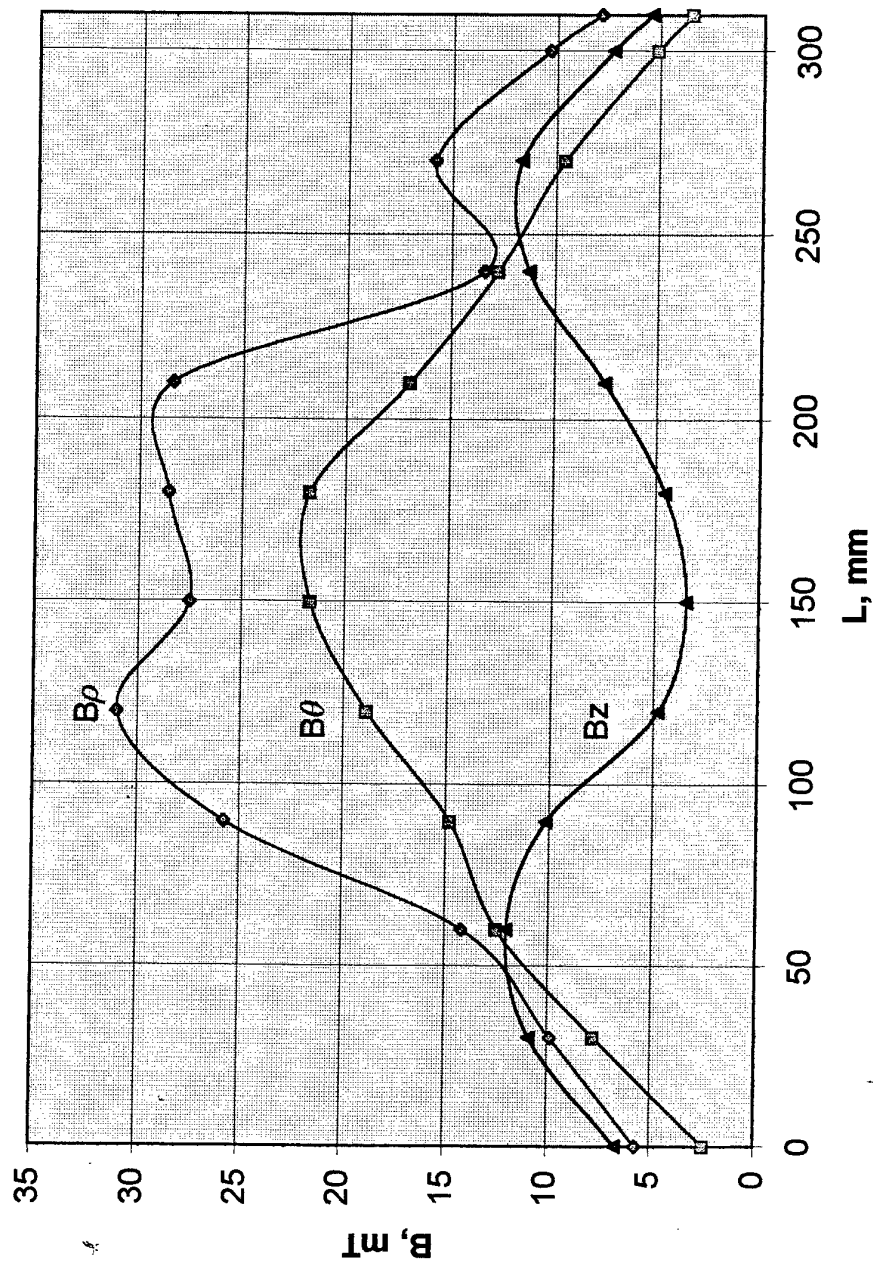


Fig. 2.6. Distribution of magnetic induction along the length of outer surface of helical winding.

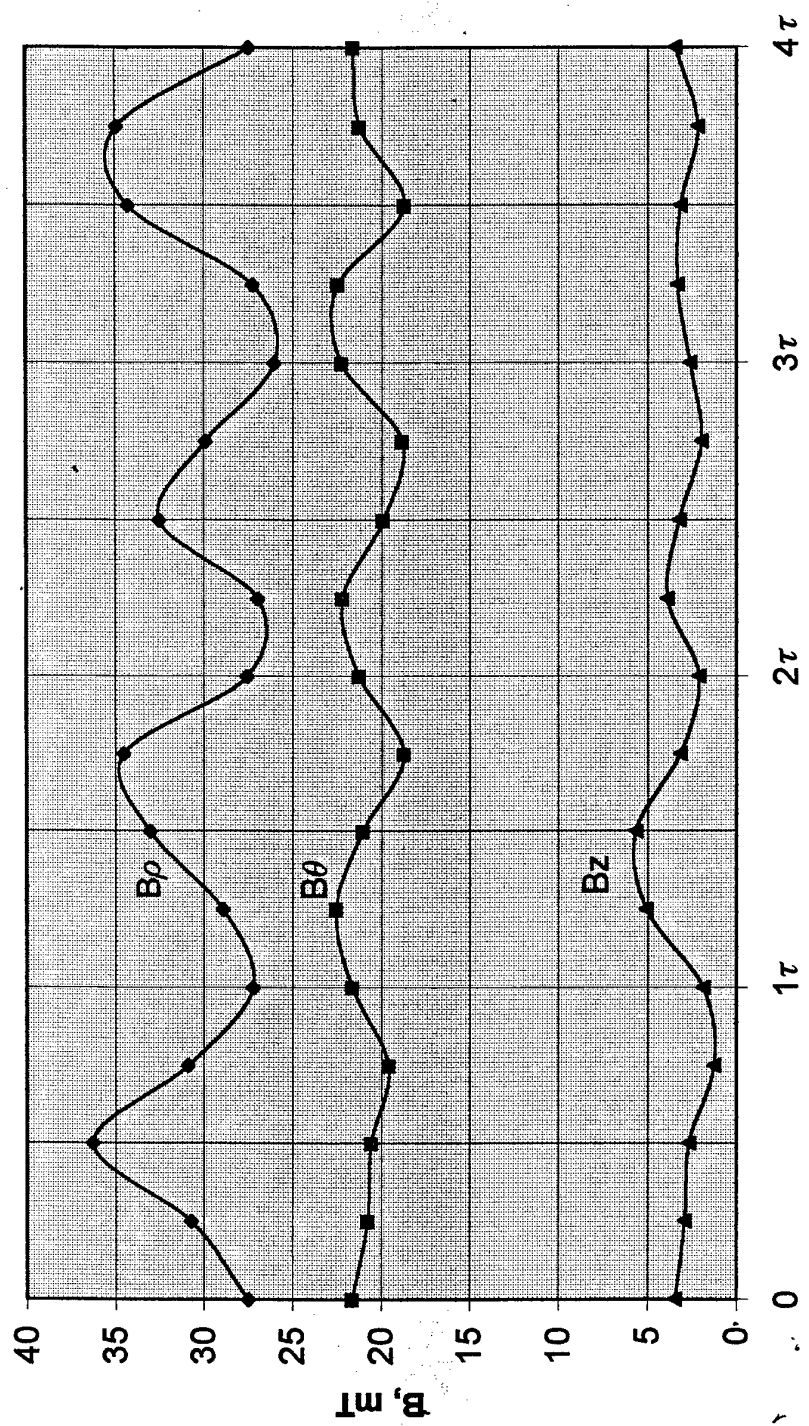


Fig. 2.7. Distribution of magnetic induction on the outer surface of the helical winding.

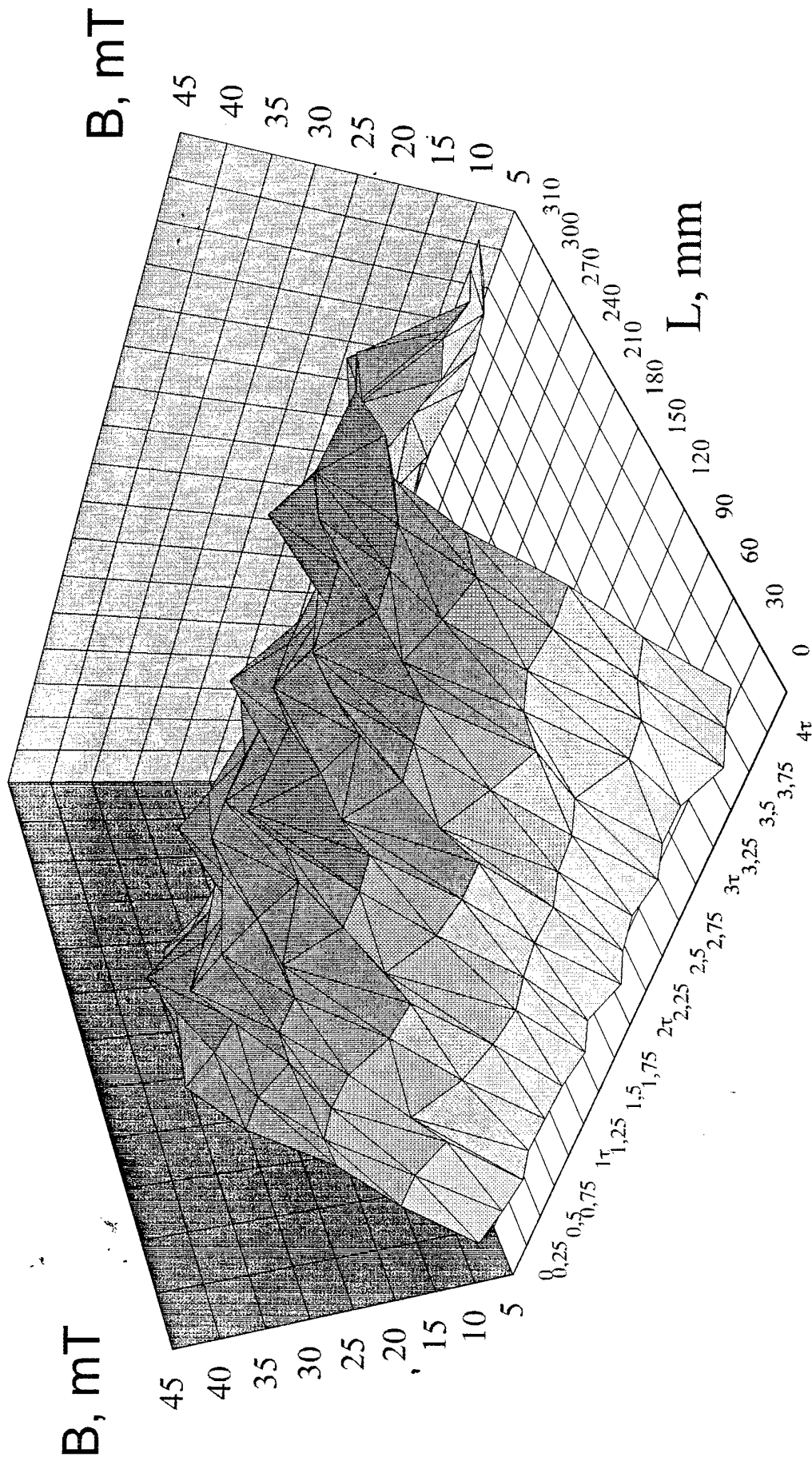


Fig. 2.8. Distribution of 3D magnetic induction on the outer surface of helical winding.

3. FABRICATION OF ALUMINUM CRYOGENIC ARMATURE BAR AND TEST FIXTURE FOR THE CONTRACT DELIVERY

3.1. Fabrication of the armature bar of composite high-purity aluminum wires and control of short-circuits

The bar was manufactured of composite high-purity aluminum wires 0.3 mm in diameter with 49 filaments, formed by 7×7 twist, of approximately 30 μm diameter, packing factor 0.65, matrix material - Al-Mn, matrix specific resistance $3.4 \cdot 10^{-8}$ Ohm·m, with outer enamel insulation 10 μm thick and break-down voltage 25 V. The cross-section of the initial composite wire is presented in Fig.3.1.

Two composite high-purity aluminum wires of 0.3 mm diameter are twisted with a twist pitch of 10 mm. Two double strands are then twisted with a pitch 20 mm. Twenty four strands of 2×2 wires are transposed in a square multifilamentary wire with a pitch of 30 mm and final size 4.6×4.6 mm².

The wire size and transposition scheme are chosen so as to minimize the losses in the armature winding. There exist three types of losses in the armature winding of a synchronous generator: ohmic losses, determined by the specific resistance of the winding material, current density value and volume of the winding material; eddy current losses, produced by the alternating magnetic fields acting in the winding region, and circulating current losses, caused by the imperfection of the transposition scheme of the elementary wires inside the armature bar. There may be an extra component of current eddy losses due to the alternating currents flowing inside the elementary wires, but they are negligibly small for the wire diameters being discussed. The eddy and circulating current losses are produced by both excitation winding and armature winding magnetic fields.

The positions, occupied by an individual 2×2 strand (one of 24 in the multifilamentary wire) during the transposition in the discussed multifilamentary wire within the transposition pitch are presented in Fig. 3.2. The character of compensation of the circulating currents for the developed transposition scheme is shown in Fig. 3.3.

To evaluate the circulating EMF compensation the magnetic field components acting along the armature bar width and height are artificially subdivided into two components each: self field and external field. It is therefore assumed that the self field component changes its sign and external field component is constant either along width or height of the transposed wire. In our case the three components are significant for the circulating EMF: radial component of self field

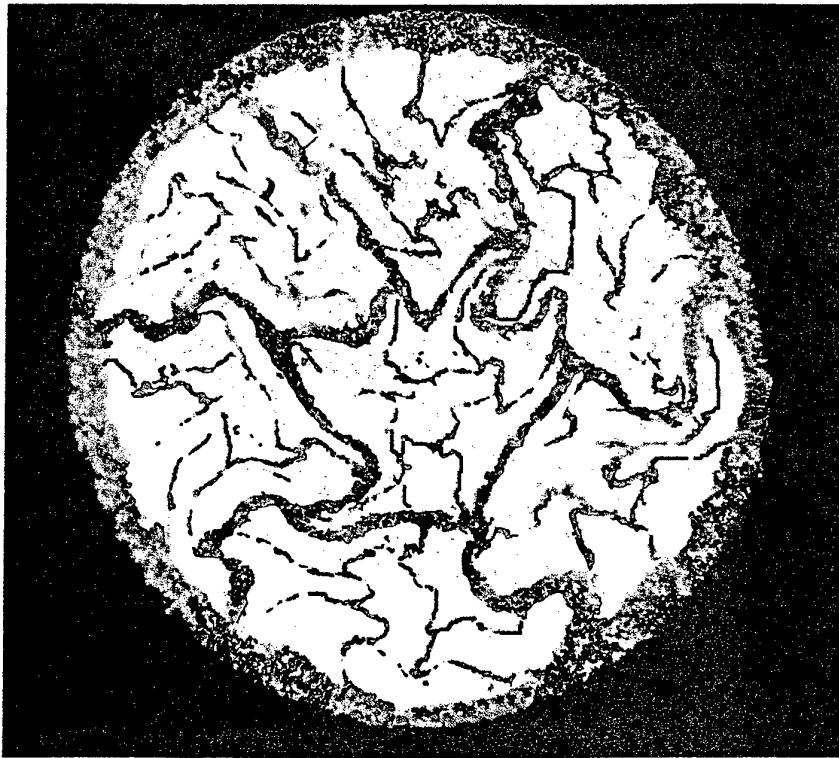


Fig.3.1. Cross-section of the composite high-purity aluminum wire.

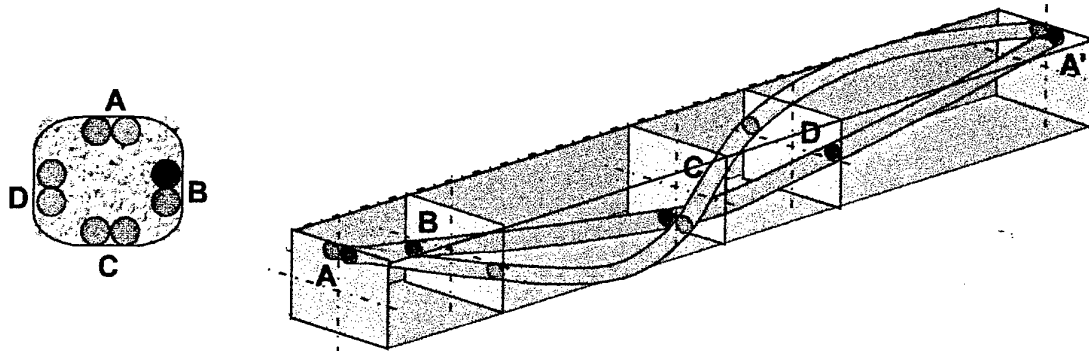


Fig.3.2. Positions, occupied by individual strands within the transposition pitch.

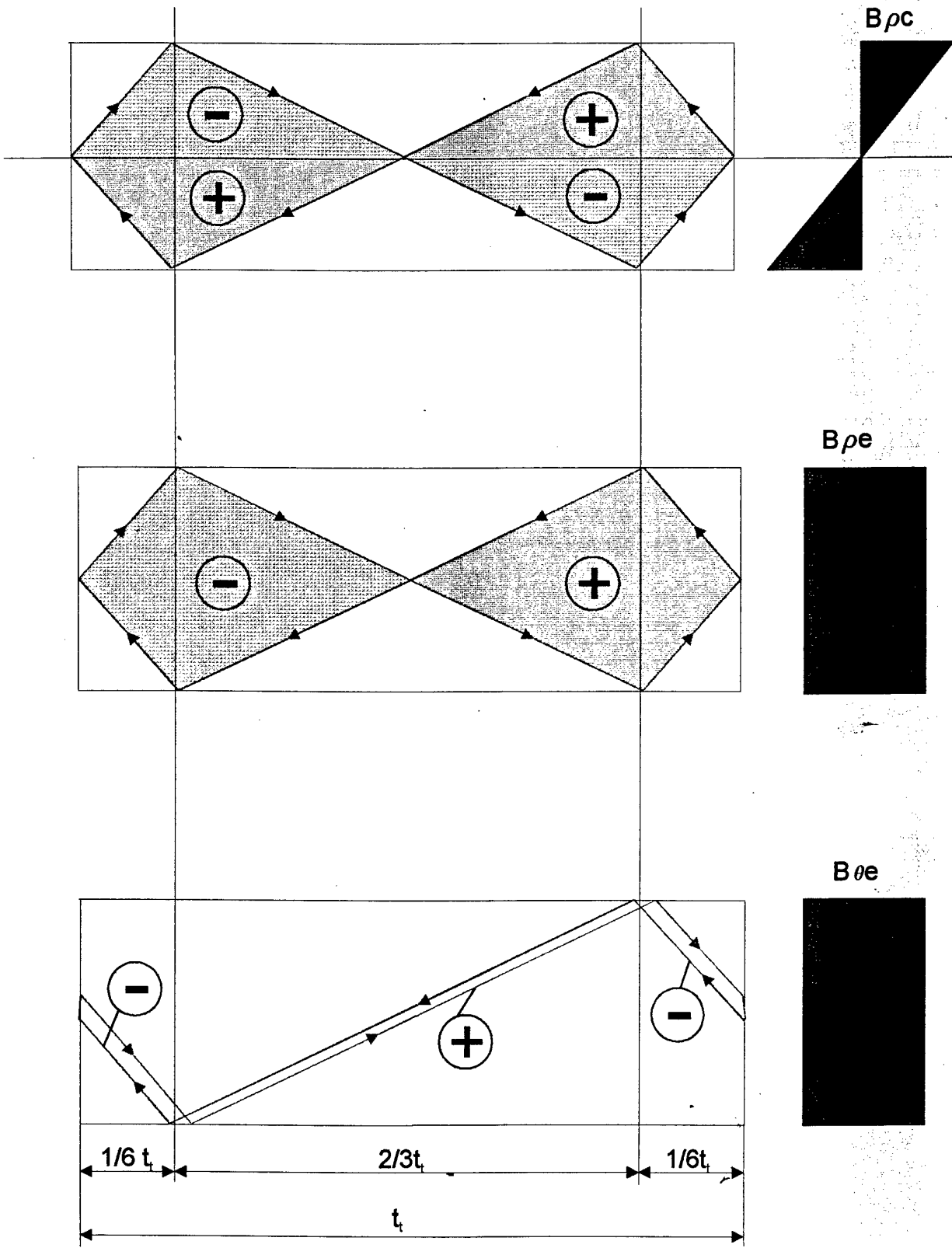


Fig. 3.3. Compensation of circulating EMF acting between the strands in the transposed multifilamentary armature bar.

$B_{\rho c}$ and radial and tangential components of external field $B_{\rho e}$ and $B_{\theta e}$. Figure 3.3 shows the circulating current losses are excluded due to the applied transposition scheme from all the component of magnetic fields acting along the transposition pitch. It is therefore extremely important not to spoil the picture by presence of short circuits between the wires along the ber length.

As for the eddy current decreasing the following principles are applied. Let us consider a winding, in which the circulating current losses are negligibly small. It is possible in case of multi-stage transposition schemes development for the winding bar manufacturing. The sum of the ohmic and eddy-current losses then equals

$$P_{\Sigma} = (J^2 \rho + k \frac{d^2}{\rho}) V, \quad (3.1)$$

where J - current density, ρ - resistivity, d - filament diameter, V - wire volume, k_1 - coefficient of eddy-current losses.

The volume of the wire depends on the current density:

$$V = \frac{k_2}{J}, \quad (3.2)$$

therefore the losses may be determined as:

$$P_{\Sigma} = k_2 \rho J + k_1 k_2 \frac{d^2}{\rho J}. \quad (3.3)$$

With the temperature decrease the first component in the right side of the equation decreases and the second component - increases. The minimum value of losses may be obtained when

$$\frac{dP}{d\rho} = 0, \quad (3.4)$$

or it may be represented as:

$$\rho J = \sqrt{k_1} d = 1.11 f B d, \quad (3.5)$$

where $k_1 = \frac{1}{32} \omega^2 d^2$, $\omega = 2\pi f$, f - frequency, B - magnetic flux density.

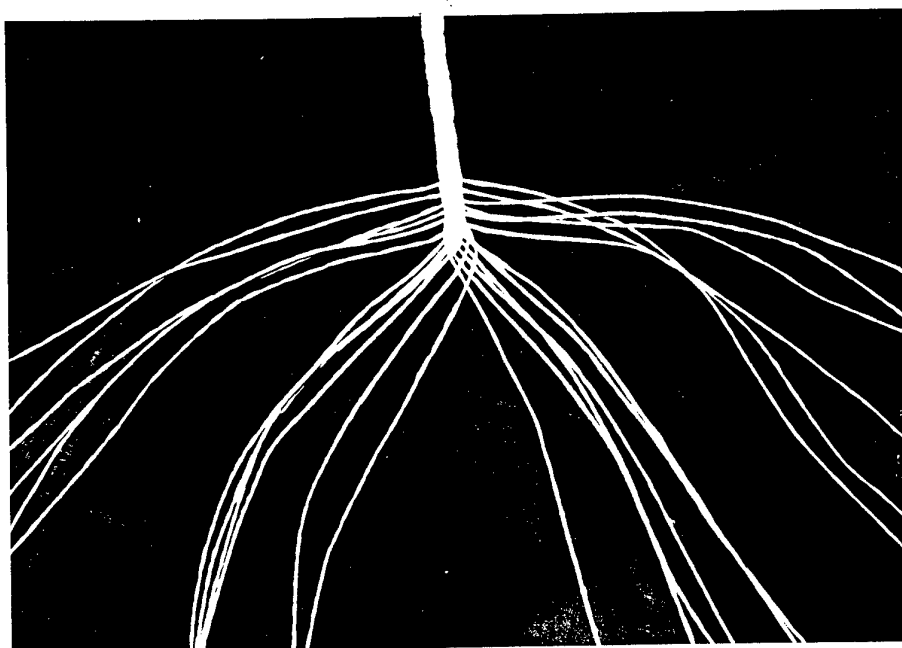


Fig. 3.4. The process of multifilamentary bar transposing.

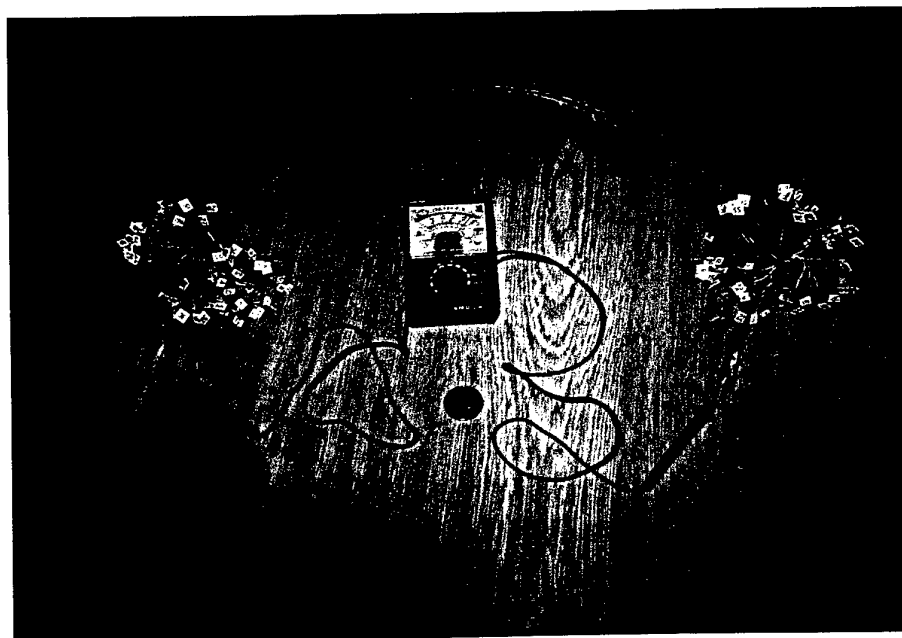


Fig. 3.5. Short-circuit control of the armature bar manufactured of composite high-purity aluminum wires.

The optimal filament diameter is then obtained from

$$d = \frac{\rho J}{1.11 f B} \quad (3.6)$$

The final cross-section of high purity aluminum in the multifilamentary wire equals 4.5 mm², packing factor is 0.21. The main bar (**Sample 1**) was manufactured of this multifilamentary strand. Figure 3.4 shows the process of multifilamentary wire transposing.

The main bar has undergone constant individual short-circuit control for all the 96 wires. The process of control is presented in Fig.3.5. The results of control before and after the bar laying down in the slot and impregnation are presented in Tables 3.1 and 3.2. They allow to conclude that with the accepted transposition scheme and due to absence of short-circuits, the bar is loaded only by the main current and the eddy currents and there are no circulating currents in between the elementary 0.3 mm wires within the bar length.

3.2. Fabrication of armature bar versions manufactured of copper and high-purity aluminum wires

Three more bars were manufactured for comparison with the test data of the main bar. They are laid down in the slots of the support structure. They are:

Sample 2. High-purity aluminum wires of 0.1 mm diameter with enamel insulation form a strand with 28 elementary wires and a twist pitch of 35 mm. Twenty four strands are transposed in a flat braid with a pitch 33 mm and a flexible final size 6×3.2 mm². Effective cross-section of high-purity aluminum equals 5.28 mm², packing factor is 0.27.

Sample 3. Copper wires of 0.071 mm diameter with enamel insulation form a twisted strand with 60 elementary wires. The strands have silk insulation. Twenty four strands are transposed in a square multifilamentary wire with a pitch 49 mm and final size 4.5×4.5 mm², packing factor is around 0.28.

Sample 4. High-purity aluminum wires of 0.1 mm diameter with enamel insulation form a strand with 28 elementary wires and a twist pitch of 15 mm. Twenty four strands are transposed in a square multifilamentary wire with a pitch 33 mm and final size 4.5×4.5 mm². Effective cross-section of high-purity aluminum equals 5.28 mm², packing factor is 0.26.

Table 3.1

Results of short-circuit control before the bar laying down.

	1"	2"	3"	4"	5"	6"	7"	8"	9"	10"	11"	12"	13"	14"	15"	16"	17"	18"	19"	20"	21"	22"	23"	24"	
1'	#																								
2'		#																							
3'			#																						
4'				#																					
5'					#																				
6'						#																			
7'							#																		
8'								#																	
9'									#																
10'										#															
11'											#														
12'												#													
13'													#												
14'														#											
15'															#										
16'																#									
17'																	#								
18'																		#							
19'																			#						
20'																				#					
21'																					#				
22'																						#			
23'																							#		
24'																									#

Table 3.2

Results of short-circuit control after the bar laying down and impregnation.

	1"	2"	3"	4"	5"	6"	7"	8"	9"	10"	11"	12"	13"	14"	15"	16"	17"	18"	19"	20"	21"	22"	23"	24"	
1'	#																								
2'		#																							
3'			#																						
4'				#																					
5'					#																				
6'						#																			
7'							#																		
8'								#																	
9'									#																
10'										#															
11'											#														
12'												#													
13'													#												
14'														#											
15'															#										
16'																#									
17'																	#								
18'																		#							
19'																			#						
20'																				#					
21'																					#				
22'																						#			
23'																							#		
24'																									#

1'-24' - right side strands; 1"-24" - left side strands.

3.3. Description of the armature of the high-speed electrical generator

Figure 3.6 presents an axial cross-section of the armature of high-speed electrical generator employing cryogenic cooling system for the winding and iron screen. A double-layer helical armature winding 1 is laid down on the outer surface of cylindrical support structure made of fiber-glass laminate 2. The construction is mounted on a cylinder 3 separating the armature cryogenic zone from the space, occupied by the generator rotor. The whole unit is then epoxy impregnated and baked. Thus, the winding with all the non-metallic elements form a single unit. The winding is connected to the current leads 4 fixed on the separating cylinder in the stator cryogenic zone as well.

The outer armature shell 6, fabricated of a titanium alloy, envelopes the stator cryogenic zone and serves as its outer generator frame. To eliminate thermal stresses, this shell incorporates an elastic element (slyphon) 7. Both ends of the shell are welded to the end caps 8, which are sealed with ring-shaped seals on the separating cylinder in the warm zone. The cryogenic zone is protected against heat fluxes from any side by vacuum insulation. The vacuumed shell is welded from above and from both faces, and the cavity wherein the generator rotor rotates is sealed with the help of stationary seals 9 placed between the end shields and the separating cylinder and with the hydrodynamic capillary-type seals 10 along the rotor shaft. The figure shows the simplified view of combined bearing-sealing unit.

Liquid coolant is supplied into the cryogenic zone and the evaporated portion of the coolant is discharged from it via evacuated pipes 11 with pin-type connectors at their ends. Stator current leads 12 are located inside the pipes as well. All the metallic design elements of the stator except current-carrying ones are made of a titanium alloy.

There is proposed the following technology for the armature winding manufacturing. The winding support structure 2 is fixed rigidly on a separating cylinder 3. The winding 1 is being laid out on the support structure. The fiber glass cylinder with machined slots is used for laying down of the first layer of the helical armature winding. After that the system of cooling ducts is being organized and the second layer of the winding is being laid down. The helixes of the second layer have the opposite direction to the first layer. After the cooling ducts for the second layer are being formed, the electrical joints of the bars are made as well as all the interphase and phase connections and the cylinder with the winding is being bandaged on the outer surface with a thermal setting tape.

The winding insulation scheme is being based on the following principle. The winding conductors of each phase are laid with small spaces between them.

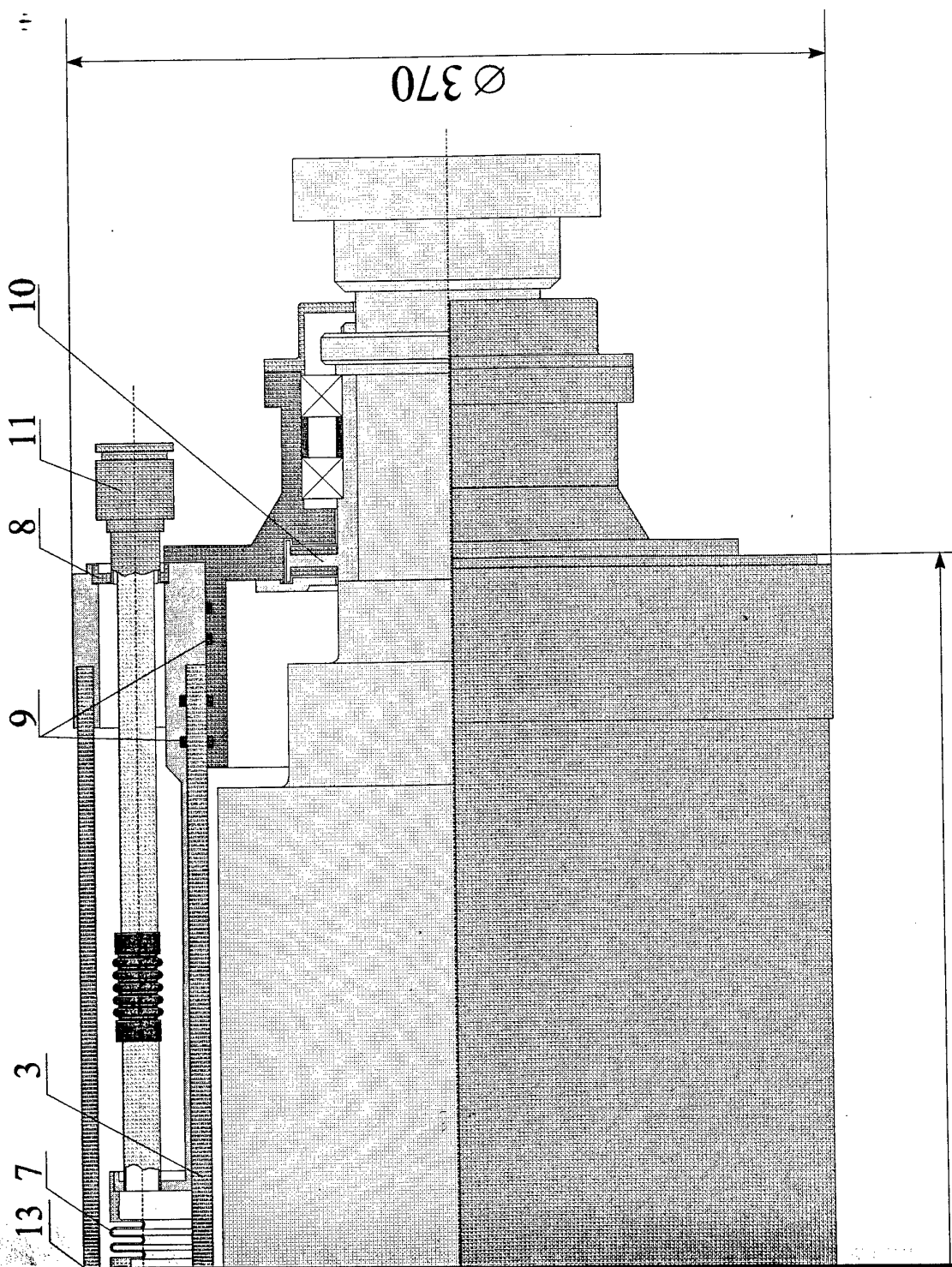
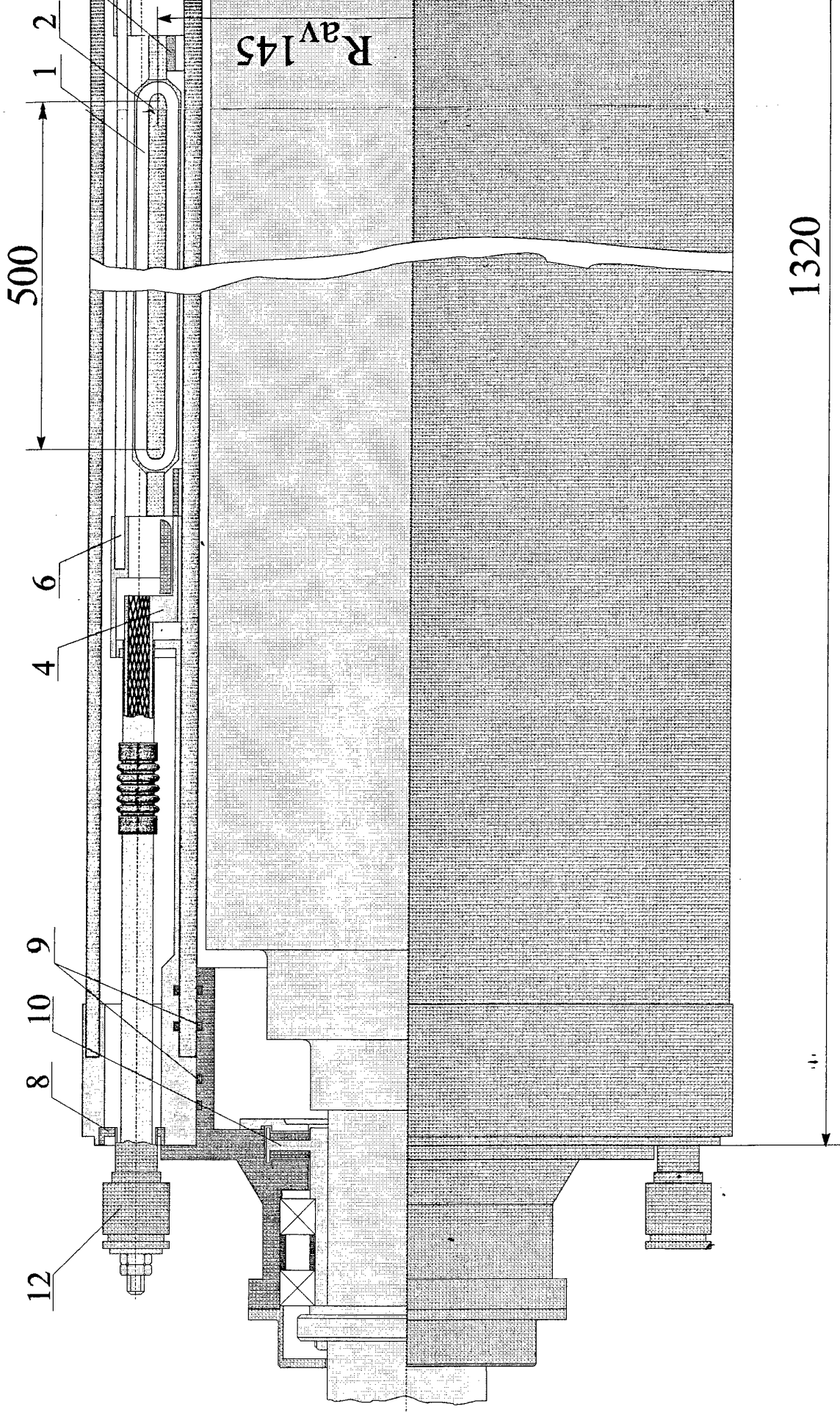


Fig.3.6. Hyperconducting armature of a high-speed generator with a single cryostat.



500

1320

Rav 145

1 2
4 6
8 9 10 12

Dielectric barriers are positioned between the extreme conductors of adjacent phases (semiphases), and the whole winding is filled by a thin layer of compound, which in this situation provides both electrical and mechanical strength of the winding. The scheme has undergone experimental investigation on a model and proved it stands in liquid nitrogen 10 kV of operating voltage level. It is worth noting that the developed insulation scheme is intended for operation in the liquid insulant medium. It means the coolants are to be either liquid nitrogen or liquid hydrogen, possessing high dielectric strength.

The volumes in the winding to form the cooling ducts are protected by special inserts with antiadhesive coating. The assembled unit is placed in a special form. The form is evacuated, filled with an epoxy and baked at 150° C for 1.5 hours. The withdrawn from the form monolithic unit is cleared from the inserts and extra epoxy. The winding cylinder is then assembled with a slide fix on the armature cryostat inner cylinder 3 and fixed in axial direction with a help of rings 13. Then the current connecting elements 4 are fixed on a cylinder 3 and are connected to the winding terminals. The ferromagnetic screen (if any) together with the shell 6 and the sylvphon 7 is assembled on the winding outer surface. End caps with preliminary welded tubes for the coolant inlet and outlet and for the current leads are welded into the shell 6. The assembled structure is covered by an outer cylinder (generator frame) and the end caps 8 are welded to it from both sides. Each welding procedure is being controlled for the absence of seal leaks at ambient and liquid nitrogen temperatures. The armature winding bus are fixed by bolts and have static seals.

3.4. Description of the delivery test fixture

The test fixture intended for the Contract delivery represents a part of a stator winding of the 5 MVA class alternator with superconducting field winding and hyperconducting armature winding. The DC field winding is intended to be manufactured of high-temperature superconductor and the AC armature winding is intended to be produced of high-purity aluminum. The armature winding bars are to operate under 400-800 Hz current and voltage frequency and in liquid hydrogen medium, used as a cooling and partially as an insulating liquid. As the armature winding bars are positioned in plastic slots, special measures are to be accepted to decrease the additional losses, caused by the components of the main magnetic flux. Therefore attention was paid to the elementary wire size and transposition scheme accepted. The final version of the armature bar has minimal total losses and thus minimal flow rate of coolant.

The test fixture with cryogenic armature bars is a part of an armature unit shown in Fig. 3.6, positions 1 and 2.

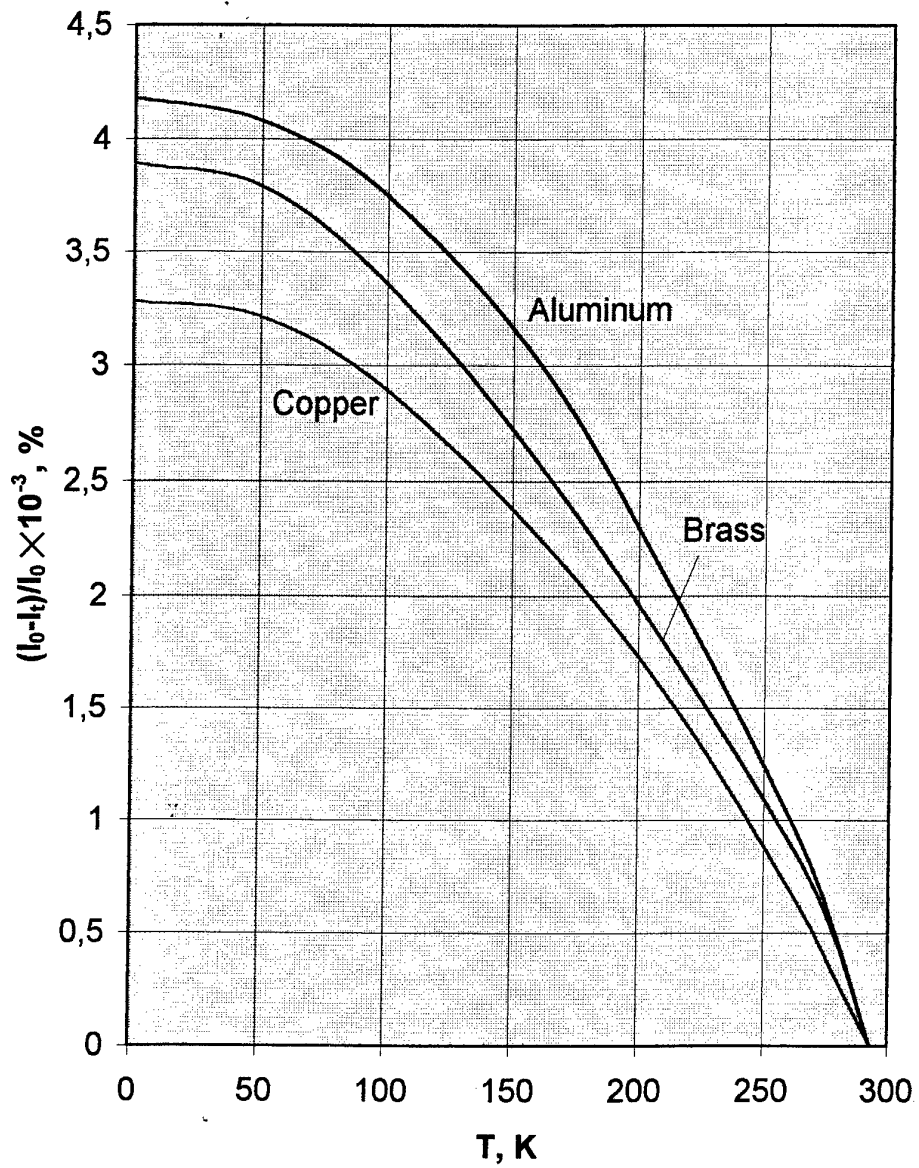


Fig. 3.7. Relative thermal deformation of the metals applied in electrical joint unit.

The support structure of the test fixture is a 1/3 part of a cylinder. It is manufactured of the fiber glass textolite. The four machined slots occupy 1/4 part of a cylinder. The slots represent themselves the helixes of one layer of the helical winding being investigated. The slots have cross-section $5 \times 5 \text{ mm}^2$. The slot helix portion is 470 mm. The four bars described above are 520 mm long in the insulated and transposed portion. Around 50-60 mm of non-insulated wire form the joint surface on both sides of each bar.

The support cylinder has $ID=292 \text{ mm}$, $OD=310 \text{ mm}$ and axial length 570 mm. The outer surface of the bars is opened to the coolant in accordance with the scheme of direct cooling, accepted for the developed helical armature winding version. The bars are epoxy impregnated.

In accordance with the accepted and tested insulating scheme the bars have no individual insulation to provide better cooling conditions. Dielectric barriers, as it was mentioned above, are positioned only between the extreme conductors of adjacent phases (semiphases) and are not applied in the model.

Special attention was paid to electrical joints. Though we have practical experience with high-purity aluminum wire soldering, still we do not consider this method reliable because of possible changes in the impurities content. Therefore the system of mechanical contact between the non-insulated part of the bars and the clips was applied. The previous investigations have shown this type of electrical contact to be a reliable one. The system of current connections of the bars consists of special copper clips on both sides of the support cylinder. It is the copper bus on one side with the cross-section of $35 \times 6 \text{ mm}^2$, organizing parallel connection of the investigated armature bars, and individual four copper clips on the other side with the cross-section $30 \times 6 \text{ mm}^2$. Thermal deformations of the contact unit were pre-determined in accordance with the curves of Fig.3.7. On the length of the joint elementary wires of high-purity aluminum are free from electrical insulation and fixed mechanically. Only the copper wire has soldered ends.

The test fixture with the bars and clips being fixed is presented in Fig.3.8. The test fixture ready for the delivery is shown in Fig.3.9 (the organic glass envelope is fixed on the test fixture outer surface to protect the bars during transportation).

4. EXPERIMENTAL INVESTIGATION OF CYLINDRICAL MODEL WITH THE BARS

4.1. Principles of the cooling scheme being investigated

When the armature winding manufactured of multifilamentary strands is being discussed, the armature bars may have either a direct cooling along the bar length, or they may be cooled by means of axial thermal conductivity from both sides. In the first case the bar cooling due to axial thermal conductivity will take place as well.

Specific feature of these variants lies in the fact that thermal conductivity of the bar is substantially non homogeneous in axial and tangential directions. The principles of the 2D linear model for the non-isotropic thermal conductivity of the bar structure and uniform distribution of losses along the bar length are presented below.

The bar heating is in this model characterized by the equation

$$\lambda_y \frac{\partial^2 \Theta}{\partial y^2} + \lambda_z \frac{\partial^2 \Theta}{\partial z^2} + q = 0, \quad (4.1)$$

where λ_y, λ_z - bar thermal conductivity in tangential and axial directions correspondingly,

q - specific volume losses in the bar,

Θ - temperature difference between the bar and the coolant.

The adopted scheme for calculations is presented in Fig.4.1,a.

The boundary conditions are presented as

$$\begin{aligned} \left[\frac{\partial \Theta}{\partial z} + \frac{\alpha_1}{\lambda_z} \right]_{z=l} &= 0, \\ \frac{\partial \Theta}{\partial z} \Big|_{z=0} &= 0, \\ \left[\frac{\partial \Theta}{\partial y} - \frac{\alpha_2}{\lambda_y} \right]_{y=0} &= 0, \\ \frac{\partial \Theta}{\partial y} \Big|_{y=h} &= 0, \end{aligned} \quad (4.2)$$

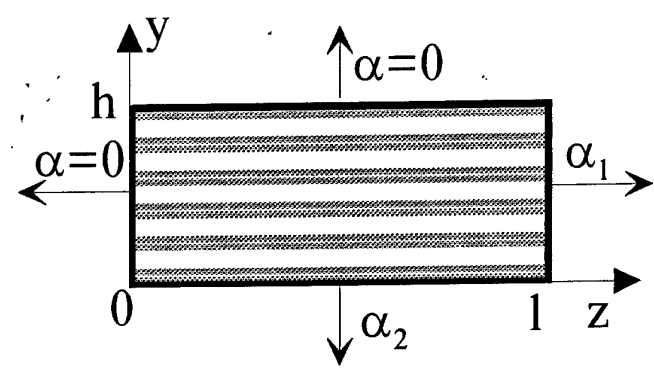


Fig. 4.1,a. An auxiliary scheme for thermal calculations.

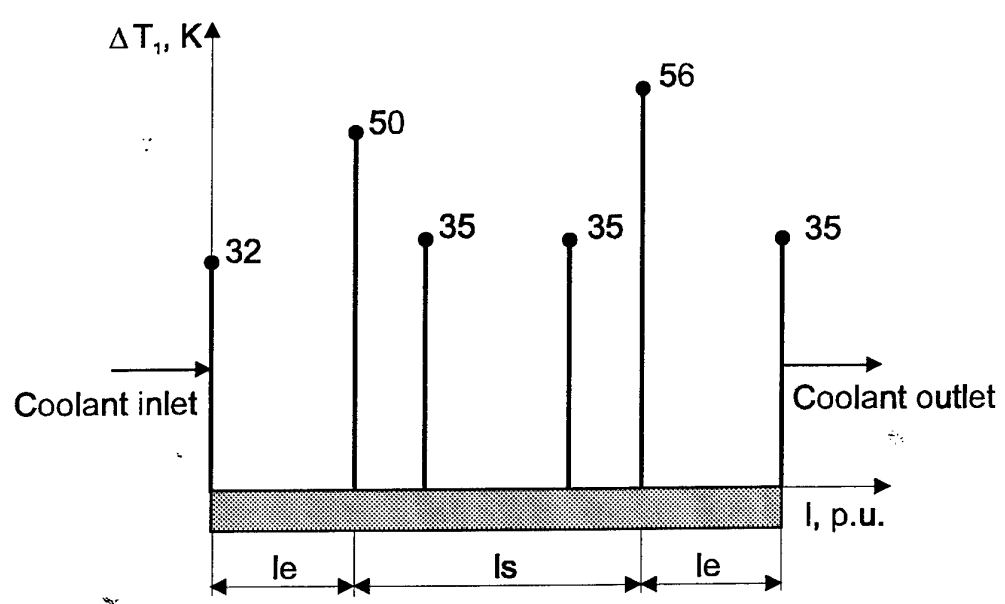


Fig.4.1,b. Overheatings of the multifilamentary armature bare of the 20 MVA superconducting turbogenerator (experimental data, 1982).

with α_1 - coefficient of heat exchange in the slot portion of the bar,
 α_2 - coefficient of heat exchange in the end portion of the bar (the winding was of
 a conventional lap geometry).

The equation was solved analytically:

$$\Theta(y, z) = \Phi(y)\Psi(z),$$

$$\text{where } \Phi(y) = M_1 \left[\frac{\lambda_y y}{\alpha_2} + y \left(1 - \frac{y}{2h} \right) \right], \quad M_1 = \left(\frac{\lambda_y y}{\alpha_2} + \frac{h}{3} \right)^{-1}. \quad (4.3)$$

$$\Psi(z) = M_4 e^{z\sqrt{M_2}} + M_5 e^{-z\sqrt{M_2}} + \frac{M_3}{M_2},$$

$$\text{where } M_4 = \frac{M_3}{\lambda_z M_2} \frac{\alpha_1}{\sqrt{M_2} - \frac{\alpha_1}{\lambda_z} - e^{2l\sqrt{M_2}} \left(\sqrt{M_2} + \frac{\alpha_1}{\lambda_z} \right)},$$

$$M_5 = \frac{M_4 \left(\sqrt{M_2} - \frac{\alpha_1}{\lambda_z} \right) - \frac{\alpha_1 M_3}{\lambda_z M_2}}{\sqrt{M_2} - \frac{\alpha_1}{\lambda_z}},$$

$$M_2 = \frac{M_1 \lambda_y}{\lambda_z h}; \quad M_3 = \frac{q}{\lambda_z}.$$

The computer program obtained on the base of these fundamental analytical expressions may be applied to calculation of thermal behavior of the armature bar, having direct cooling due to specific transverse heat conductivity λ_y and axial heat conductivity λ_z . Experimental results with temperature gradients along the armature bar of superconducting turbogenerator having direct cooling via the cooling ducts and axial cooling by heat conduction are presented in Fig. 4.1, b. As it is relatively difficult to carry out analytical determination of the components of heat conductivity, experimental evaluation of this parameter is extremely important.

In general the problem may be subdivided into two tasks: surface cooling of the bar by direct heat exchange with the coolant and adiabatic cooling of the bar by thermal conductivity via the electrical joints on the bar ends, immersed in coolant. The first problem was investigated experimentally on the cylindrical model for the

bar current carrying capability and for the disc models, with one bar surface opened to the coolant. The results of cryogenic tests of the bars with one surface opened to coolant are presented in Para.4.3. The results of investigations of the multifilamentary bar cooling by axial heat conduction and under pulse current supply are being discussed in Para.5.

4.2. Test-bed configuration

The test-bed comprises electrical, cryogenic and data acquisition equipment. Electrical scheme used during the tests is presented in Fig.4.2. A double cascade system was used as a source of current supply. It comprised two rotary power amplifiers 1 and 2. The resistances in the armature winding circuit of the first amplifier *AW1* and in the excitation current circuit of the second amplifier *FW2* are intended for the smooth regulation of the current in the circuit. The current control was performed by the voltmeter *mV1* and current shunt. The process of the current supply to the bar being investigated was performed by a personal computer *PC*, which regulated the stabilized DC current unit *S1*, switched in the circuit of the first rotary amplifier *FW1*. The investigated armature bar *Rb* was connected to the armature circuit of the second amplifier *AW2*. The signals from the temperature pick-ups, and the signals proportional to the investigated bar current and voltage drop were collected by the *PC*.

To protect the investigated armature bar from damage because of avalanche heating a special fast-response protection scheme was developed. In case the bar temperature exceeded the critical value the computer produced a control pulse for the low current relay winding *P2*. The N.O. contacts of the latter switched in the winding of the intermediate relay *P1* to the current supply. The N.O. contacts of the relay *P1* supplied the voltage to the switching off winding of the automatic field-suppression circuit-breaker *AFCB-30*. The latter in turn broke the electrical circuit with the investigated armature bar. The speed of the protection circuit operation was 0.1-0.3 s. Simultaneously the computer decreased to zero value the current in the excitation winding of the first rotary amplifier.

After each current supply the demagnetization of magnetic circuits of the rotary amplifiers was performed to exclude residual magnetization effect. During this procedure the circuit-breaker *AFCB-30* was released.

The cryogenic equipment of the test-bed comprised the cryostat for the low temperature experiments with the diameter of the cold part 300 mm and the volume of cryogenic liquid up to 100 l. The cryostat was equipped by current leads and by a special level meter, incorporating superconducting elements and

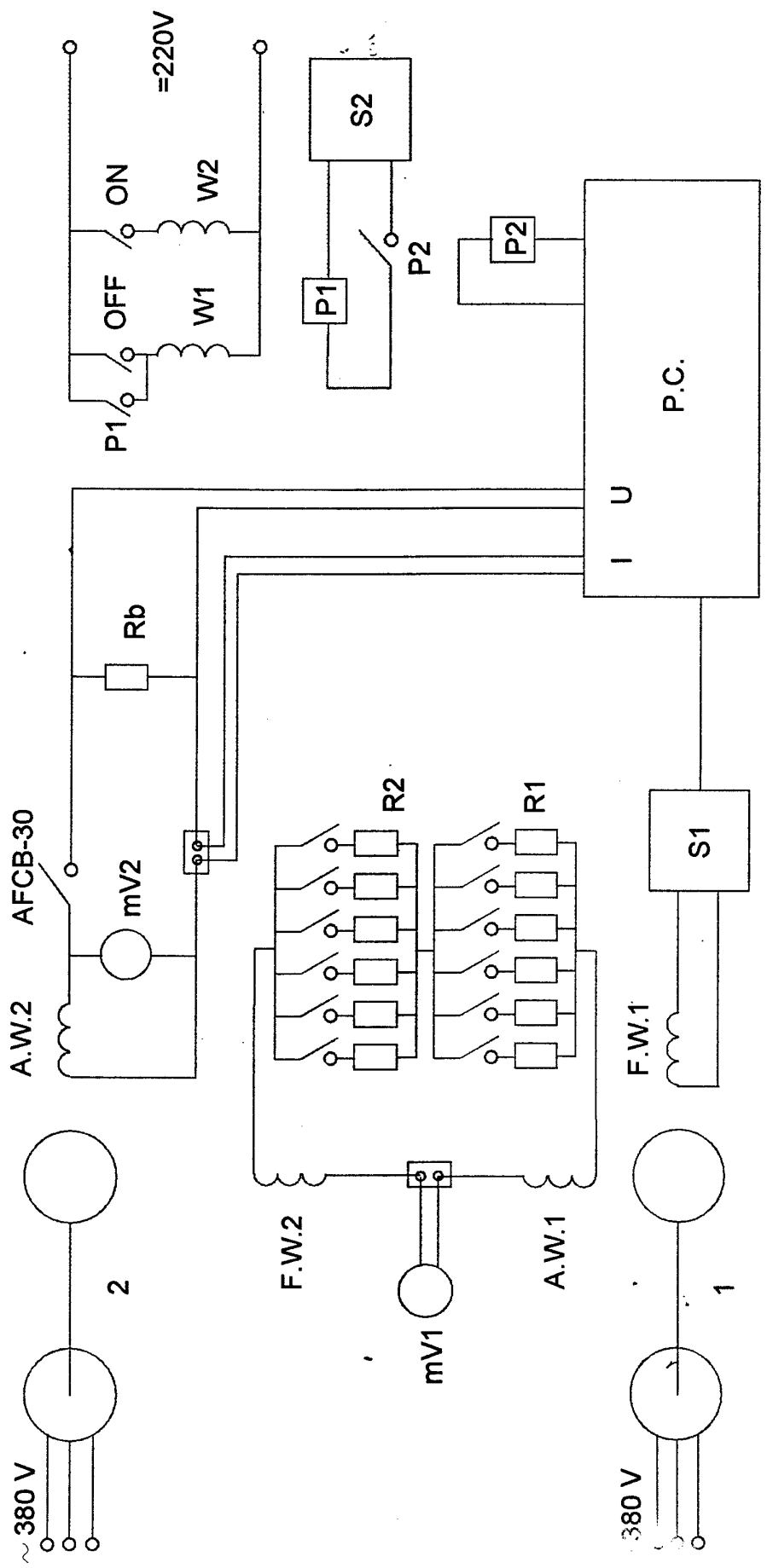


Fig. 4.2. Electrical scheme of the current supply system.

providing continuous measurement of the cryogenic liquid level along the height of the cryostat.

To supply the cryogenic liquid during experiments there were used a 500 l liquid nitrogen tank and a 500 l liquid helium tank, both equipped with level meters. A variety of vacuum pumps was involved in preparation of the cryogenic system for the low temperature experiment. The exhausted gas was stored in gasholders and transferred to the receivers with the help of compressors. The photos of the test-bed are presented in Fig. 4.3.

As it was mentioned already above, the test-bed was equipped with an IBM PC, responsible for the experimental data acquisition, processing and presentation in visual and graphical form. Details of the system and of its software are given below.

To provide high accuracy of measurements, the modified version of automatic fast-response system for experiment management was developed. The functions of the system is to measure the parameters obtained by various types of gauges and to manage the preset parameters of experiment.

Measurement is carried out with the help of PC 386 consisting of eight-digit interface cards installed in PC and eight cards for measurements, results processing and management of a mode of experiment, installed on a 16-channel cross-card (Fig.4.4, 4.5).

The developed multi-channel automated system for information registration and experiment management gives the opportunity to measure, process and display several parameters in a real-time mode. At the same time, the system provides experiment management in accordance with the preset program and protection of the test samples. In the presented investigations, the developed system was used to control sample current variation and to set voltage variation frequency and cycle during the variable-load tests. Protection of the tested sample was accomplished by load disconnection in case two of the studied parameters exceeded their preset values. In the discussed experiments those parameters were sample resistance value and resistance gradient value.

The software developed specifically for the purposes of these investigations gives the opportunity to manage the experiment, to register and process the values of various physical quantities measured by multi-channel data acquisition system, and ensures protection of the test samples. The software enables displaying the results of experimental studies both graphically and in a tabulated form. Presented in Fig.4.6-4.7 are the variants of displaying test results in the mode of visualization and processing of the data obtained. For temperature measurement

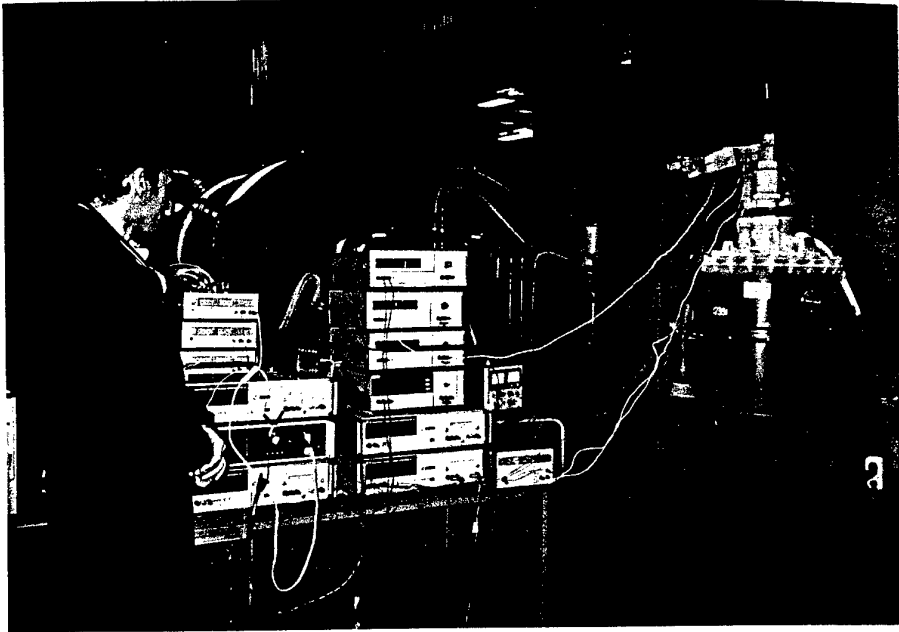


Fig. 4.3. Elements of the cryogenic test-bed and computer support of the experiment.



Fig. 4.4. Multi-channel system of test data registration with PC 386 DX.

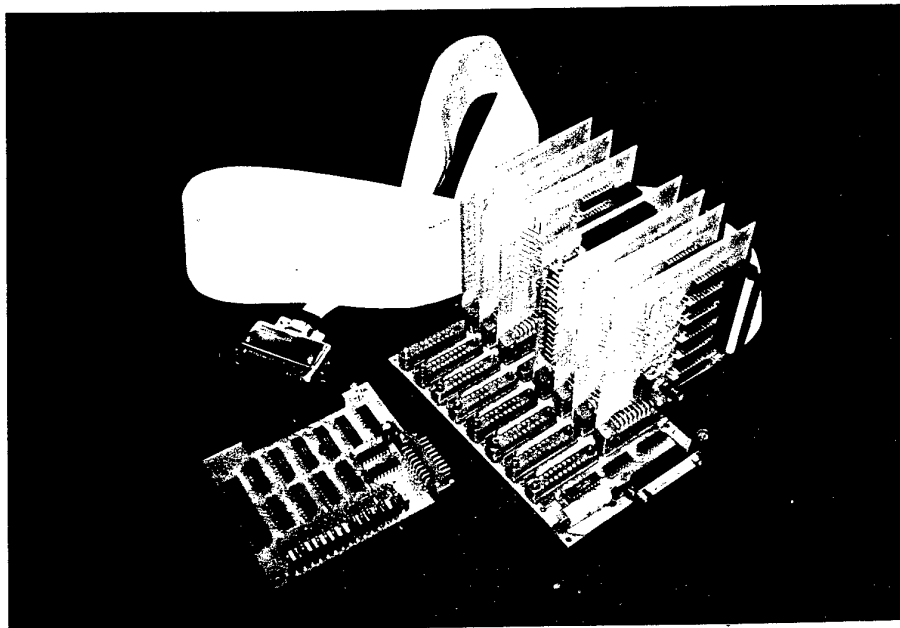
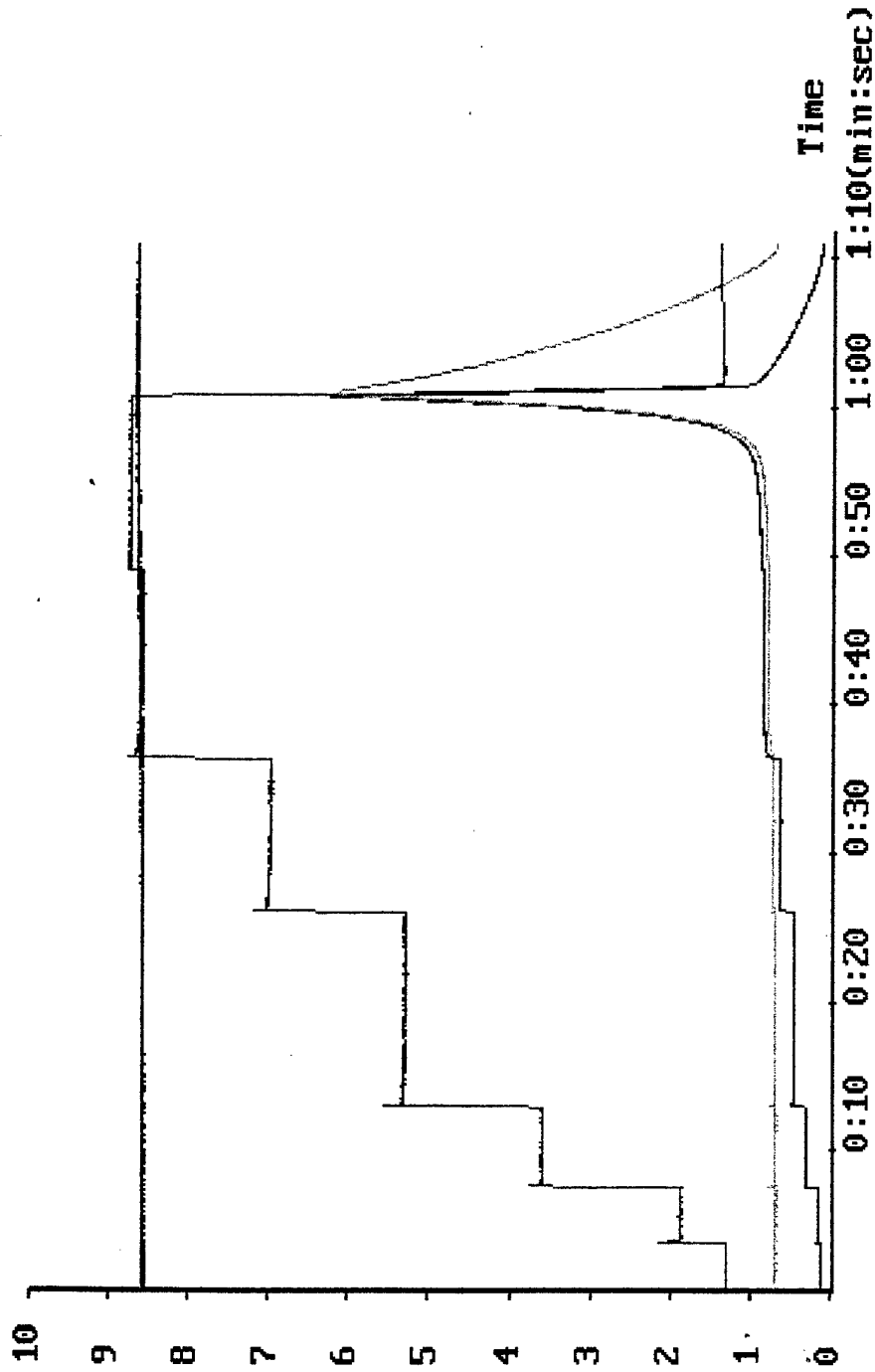


Fig. 4.5. The 16-channel cross-card with the cards for data processing and management of a mode of experiment.

E:\EXPER\DATA\2-2-2.REC

$U(2 \times 10^{-1} \text{ volt})$ $I(8 \times 10^{-3} \text{ amper})$ $T(2 \times 10^4 \text{ ohm})$



Alt-X Выход F4 Старт Alt-F3 Закрыть

304960b

Fig.4.6. Monitor presentation of test results in the mode of visualization.

E: \EXPER\DATA\1-2-4.REC

N	Время	Ток	Напряжение	Сопротивление	Температура
44	0:02	206.0	0.00333000	0.000016	4.365
45	0:02	208.0	0.00333000	0.000016	4.365
46	0:03	208.0	0.00333000	0.000016	4.365
47	0:03	246.0	0.01250000	0.000051	4.365
48	0:03	690.0	0.01250000	0.000018	4.365
49	0:03	1170.0	0.02130000	0.000018	4.365
50	0:03	1530.0	0.02850000	0.000019	4.365
51	0:03	1824.0	0.03440000	0.000019	4.371
52	0:03	1970.0	0.03790000	0.000019	4.377
53	0:03	1952.0	0.03790000	0.000019	4.371
54	0:03	1894.0	0.03720000	0.000020	4.377
55	0:03	1654.0	0.03130000	0.000019	4.371
56	0:03	1654.0	0.02610000	0.000016	4.365
57	0:03	1412.0	0.02180000	0.000015	4.365
58	0:03	1224.0	0.01840000	0.000015	4.365
59	0:03	1048.0	0.01540000	0.000015	4.365
60	0:03	892.0	0.01540000	0.000017	4.365
61	0:03	768.0	0.01300000	0.000017	4.365
62	0:03	650.0	0.01090000	0.000017	4.365
63	0:03	552.0	0.00930000	0.000017	4.365
64	0:04	468.0	0.00780000	0.000017	4.365

Fig.4.7. Monitor presentation of test results in the mode of data processing.

in the course of experimental study the calibration curves of thermoresistors were introduced into the control program in a tabulated form.

4.3. Experimental investigation of the armature bars at cryogenic temperatures

Experimental investigation of the armature bars, laid down in the test fixture, was based on the data obtained for critical modes of operation on the disc model bars. Possessing information about maximum permissible currents in the bars we did not exceed these values during investigations of the test fixture intended for the Contract delivery not to destroy the samples. Our practical experience has shown that during experiments with current variation the bars were destroyed practically instantly with an avalanche resistance growth in spite of the fast response protection system. It happened so with the directly cooled bars. As for the bars, cooled by heat conduction and discussed in Para 5, they displayed relatively slow resistance increase.

At first the test fixture has undergone the liquid nitrogen tests with determination of specific electrical resistance of the bars. The bars were loaded by current as well, but as the current value was not very high, temporary current leads with a temporary support were used (Fig.4.8), while the second cryostat was being prepared for the liquid helium tests.

During the liquid helium tests the second cryostat had a cap with mounted current leads and suspension system (Fig.4.9). The test fixture with the armature bars was suspended on special supporting studs in the cryostat and the bars were connected to the current leads. All the unit was covered by an insulating sheet to exclude its possible contact with the cryostat inner metallic surface.

There are three current leads from the current supply to the cold zone of the cryostat with the current carrying capability up to 5 kA. The leads are cooled by the coolant vapor. Two current leads are the hollow copper tubes with the cooling gas flowing through the inner ducts. The third lead is a copper braid positioned inside the stainless steel tube. To investigate the four bars the cryostat was once opened in the middle of the cold experiment to change the current lead connections from the first pair of the bars to the second one.

Experimental results of investigation of the bars under maximum current loads are presented in Fig.4.10-4.12 for the bar manufactured of the composite high-purity aluminum (Sample 1), in Fig.4.13-4.14 for the bars manufactured of high-purity aluminum (Samples 2 and 4) and in Fig.4.15 for the bar manufactured of copper (Sample 3). It should be mentioned that in spite of relatively high current density the copper bar displayed unstable temperature behavior. It will also have

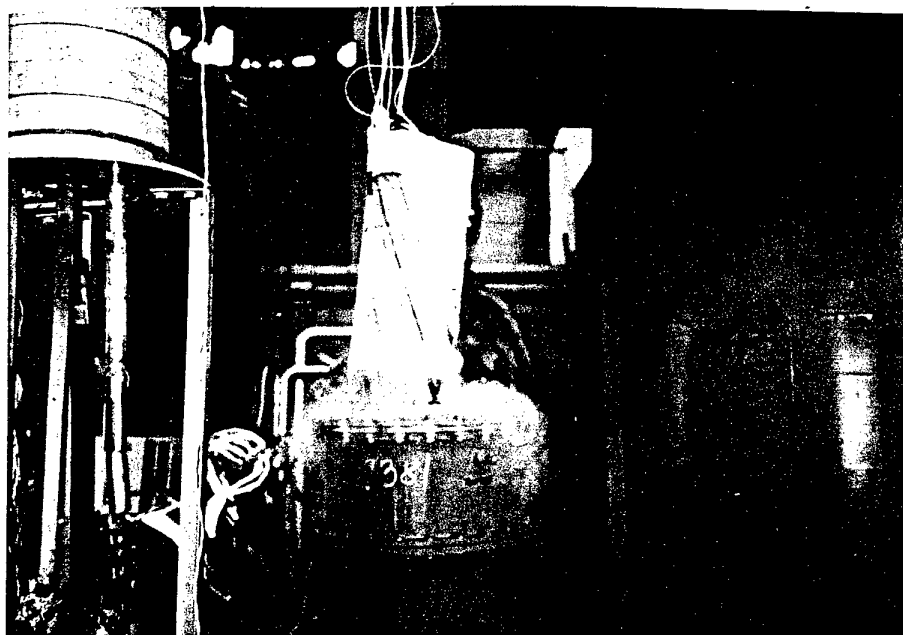


Fig.4.8. Cylindrical test fixture in the process of liquid nitrogen tests.



Fig. 4.9. Test fixture mounted on suspension system during the disconnection of the current leads.

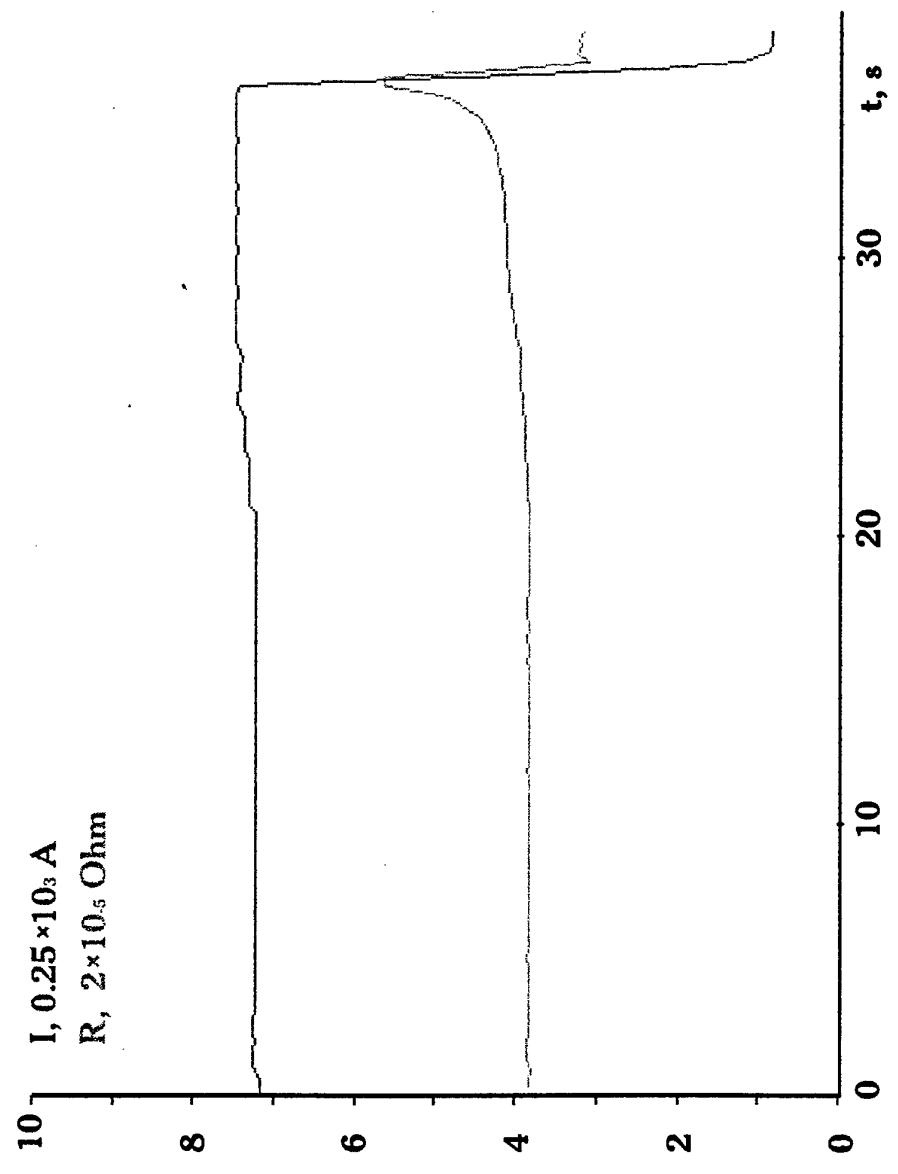


Fig. 4.10. Electrical current and resistance of the composite bar during liquid helium tests with maximum current value 1810 A.

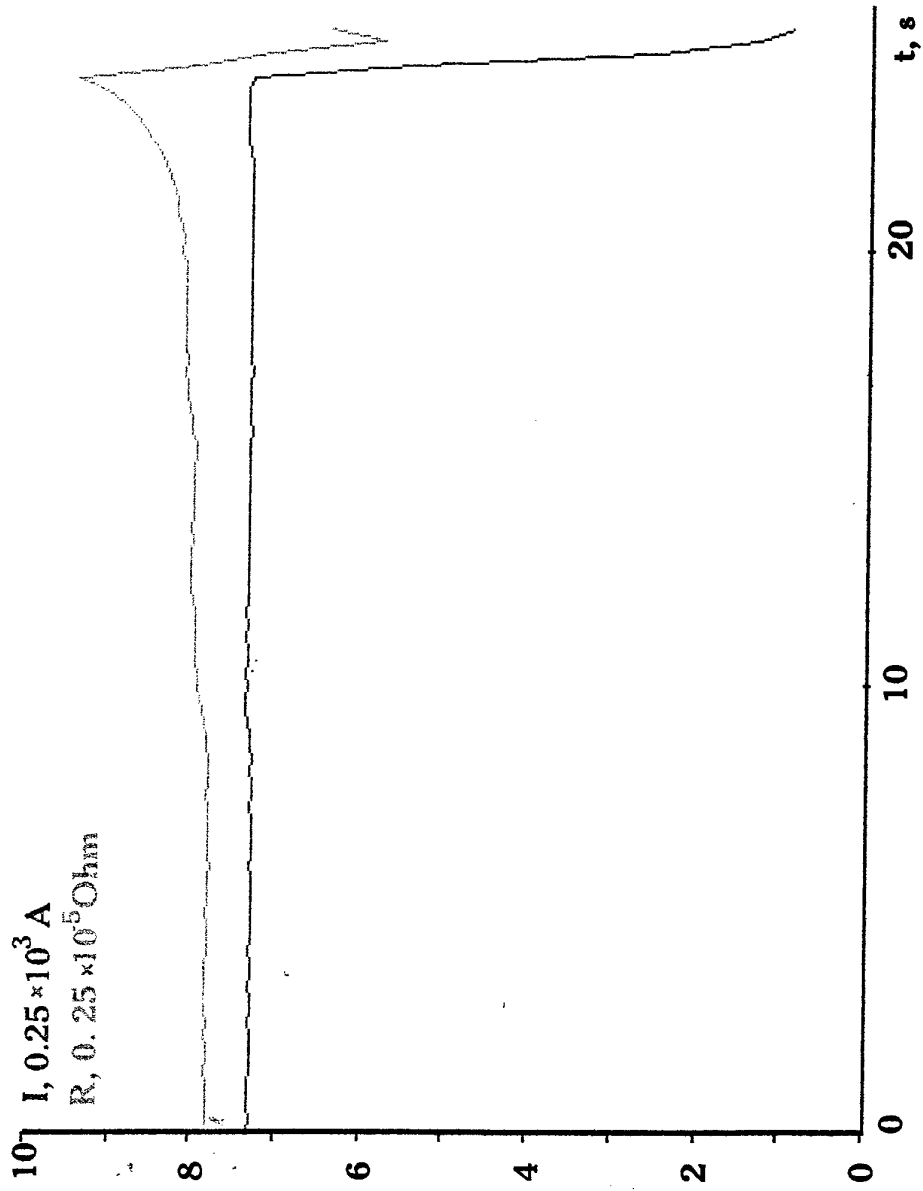


Fig. 4.11. Electrical current and resistance of the composite bar during liquid helium tests with maximum current value 1850 A.

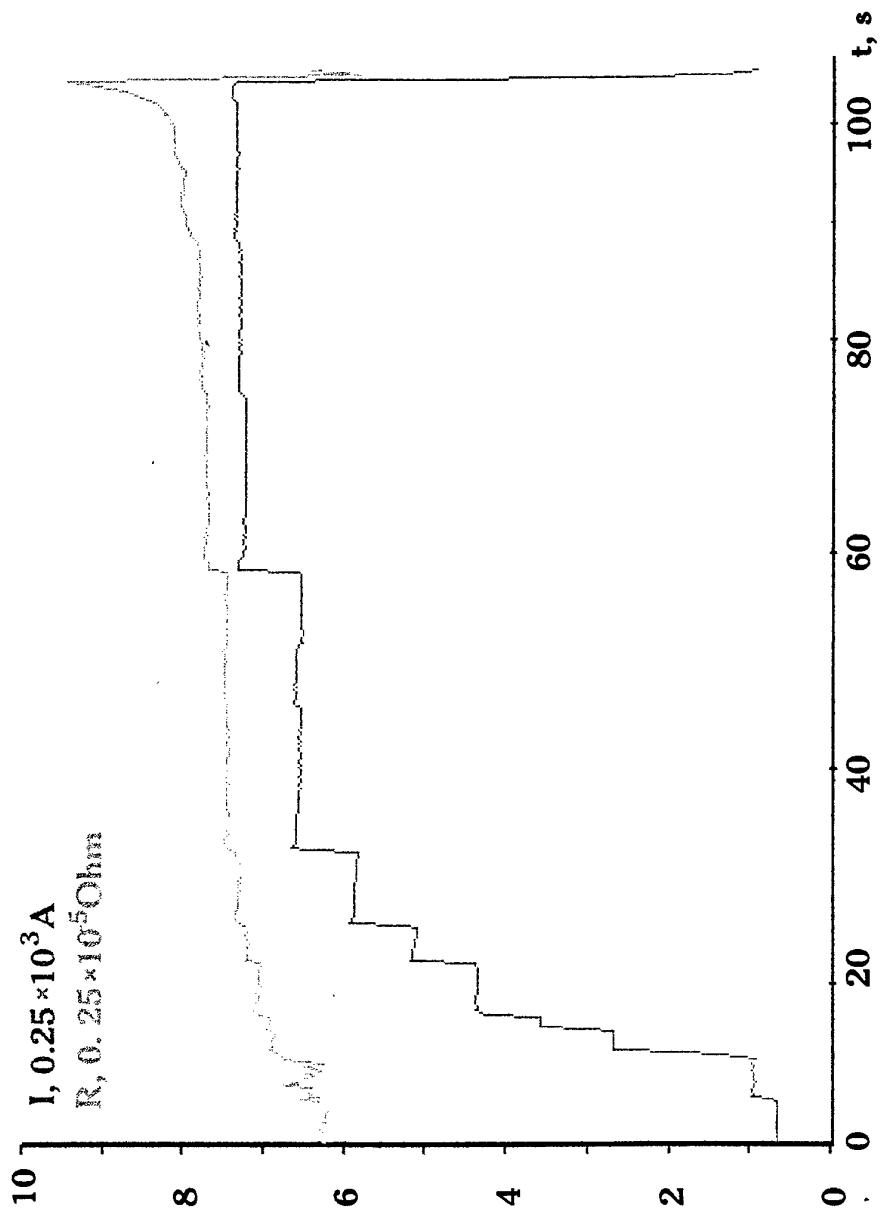


Fig. 4.12. Current variation with a subsequent electrical resistance increase during liquid helium tests.

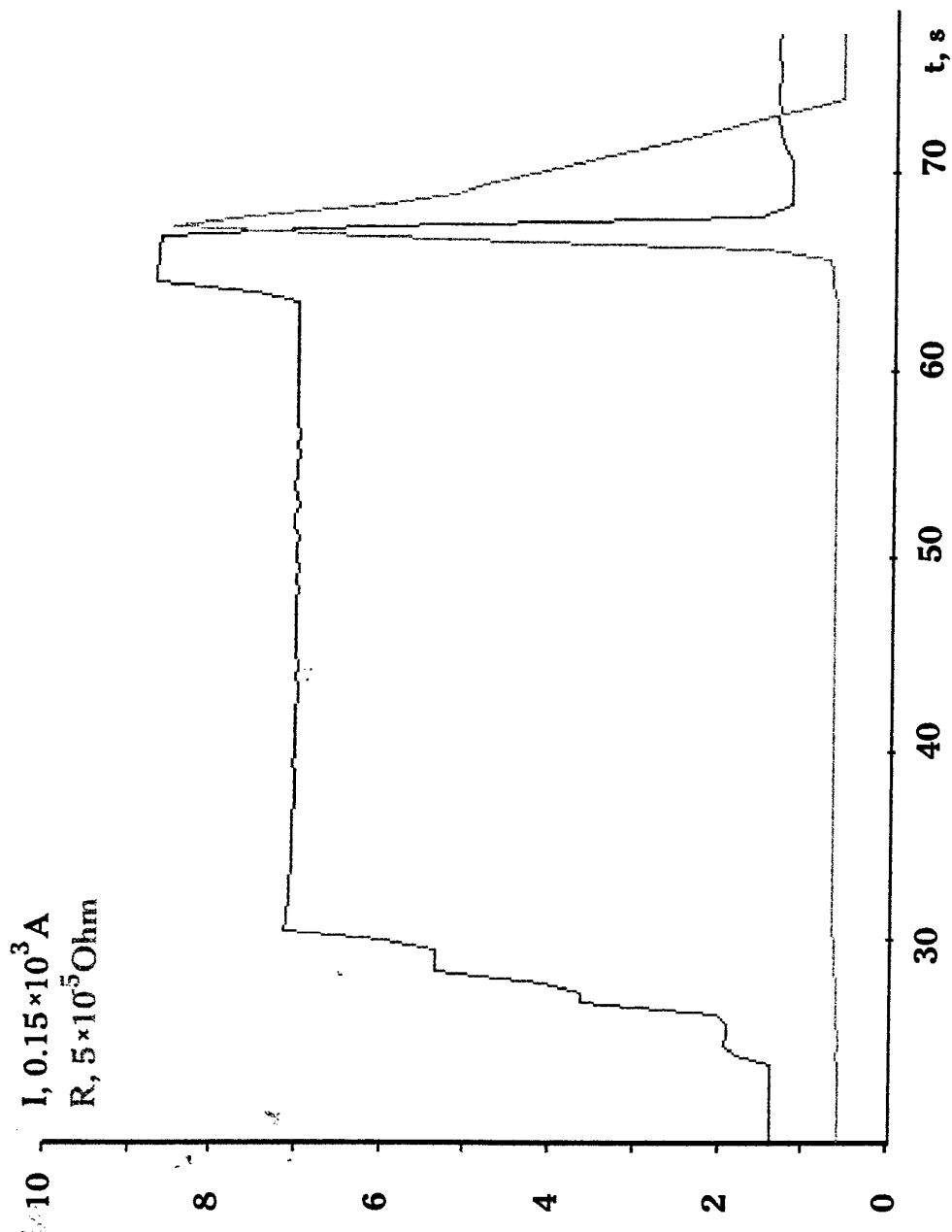


Fig. 4.13. Behavior of the bar of high purity aluminum during liquid helium tests at 1110 A of maximum current value.

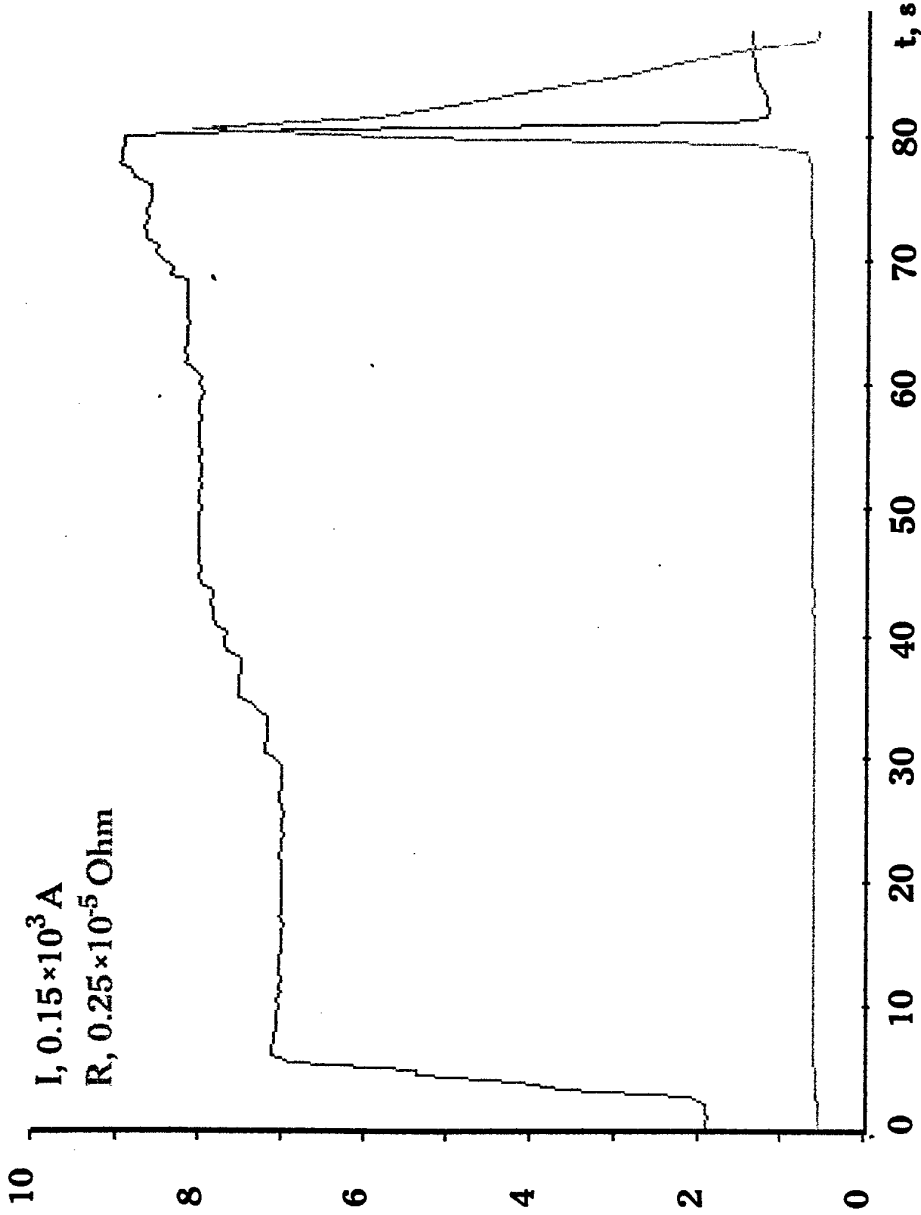


Fig. 4.14. Behavior of the bar of high purity aluminum during liquid helium tests at 1115 A of maximum current value.

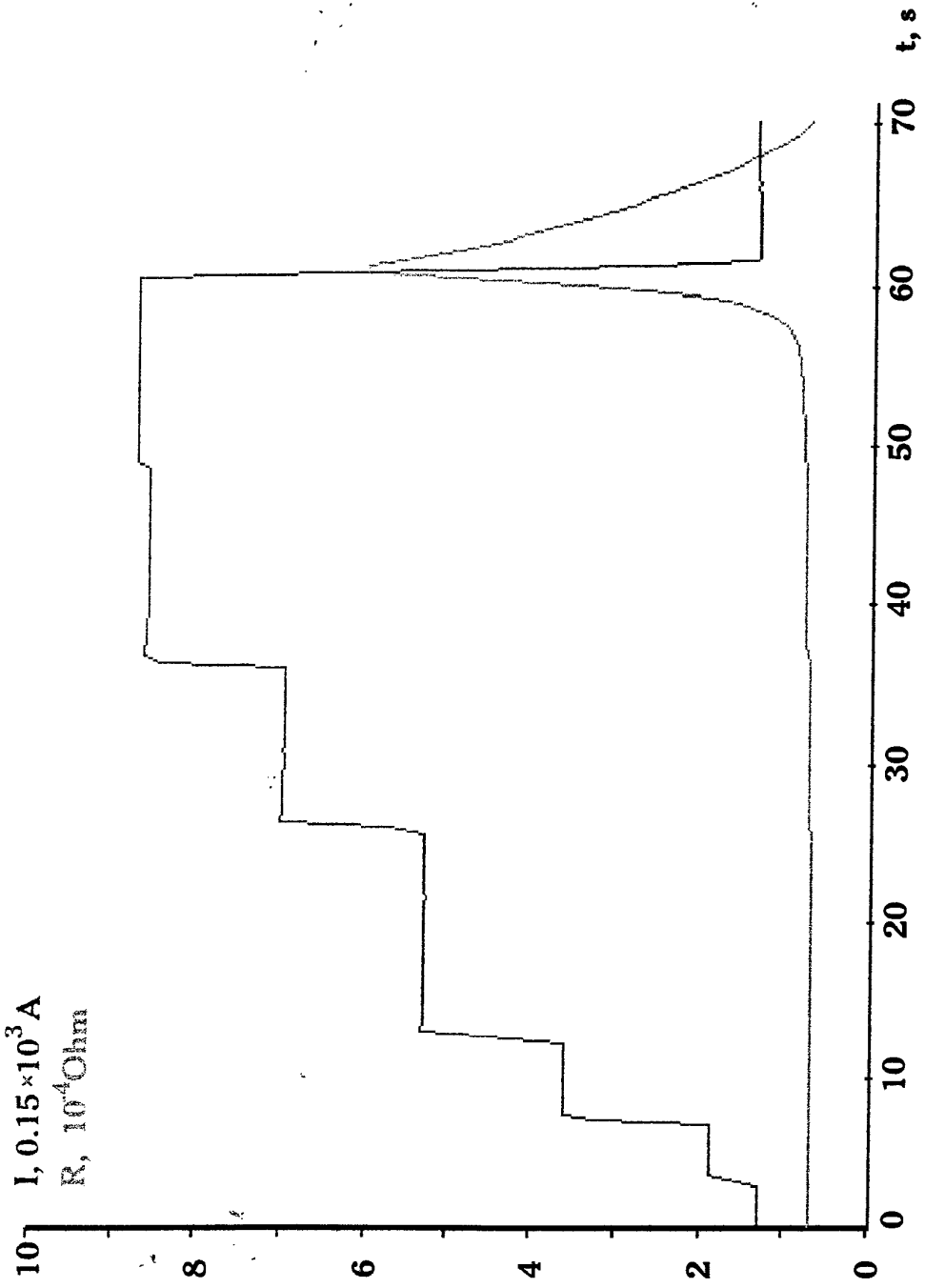


Fig. 4.15. Behavior of the copper bar during liquid helium tests at 1100 A of maximum current value.

relatively high circulating current losses in presence of main magnetic flux because of poor twisting of individual wires within the 60 wire strand.

During experiments with the armature bars there was carried out measuring electrical resistance of the composite wires, which may be represented as:

$$R_c = \frac{R_{Al} R_M}{R_{Al} + R_M}, \quad (4.5)$$

with R_{Al} - resistance of high-purity aluminum fibers, R_M - resistance of Al-Mn matrix.

The expression (4.1) may be transformed into

$$\rho_{Al} = \frac{\rho_c \rho_M S_{Al}}{\rho_M S_c - \rho_c S_M}, \quad (4.6)$$

where ρ and S - correspondingly specific electrical resistance and cross-section area. Indexes "Al" refer to high-purity aluminum, "M" - to the matrix material, "C" - to the composite itself.

At ambient temperature the matrix resistance has a certain influence on the total wire resistance

$$\rho_{Al} = \frac{3.4 \cdot 10^{-8} \cdot 4.5 \cdot 10^{-6} \cdot 2.7 \cdot 10^{-8}}{3.4 \cdot 10^{-8} \cdot 6.78 \cdot 10^{-6} - 2.7 \cdot 10^{-8} \cdot 2.37 \cdot 10^{-6}} = 2.3 \cdot 10^{-8} \text{ Ohm} \cdot \text{m}.$$

At intermediate liquid nitrogen temperature we have

$$\rho_{Al} = \frac{0.3 \cdot 10^{-8} \cdot 2.0 \cdot 10^{-8} \cdot 4.5 \cdot 10^{-6}}{2.0 \cdot 10^{-8} \cdot 6.78 \cdot 10^{-6} - 0.3 \cdot 10^{-8} \cdot 2.37 \cdot 10^{-6}} = 2.1 \cdot 10^{-9} \text{ Ohm} \cdot \text{m},$$

and the matrix resistance cannot be neglected, though if neglected the error may achieve 10 %.

At liquid helium (or hydrogen) temperature the influence of the matrix material for the composite wire discussed may be neglected due to the fact that

$$\rho_M S_C \gg \rho_C S_M, \quad (4.7)$$

and specific resistance of aluminum may be determined as:

$$\rho_{Al} \approx \rho_c \frac{S_{Al}}{S_c} = R_c \frac{S_{Al}}{l} \quad (4.8)$$

Similar results may be obtained for heat conductivity of the composite wire and its components, taking into account the $\lambda = f(T)$ dependencies for high-purity aluminum and Al-Mn alloys, presented in Fig.4.16. The heat conductivity of the matrix plays a certain role at ambient and even at liquid nitrogen temperatures but it may be neglected at liquid hydrogen and liquid helium temperature levels.

Experimental results of electrical resistance measurements for the armature bars, positioned in a test fixture, at different temperature levels are given in Table 4-1. An example of variation of electrical resistance and temperature of the composite high-purity aluminum bar during the low-temperature experiment is shown in Fig.4.17

Table 4-1

Specific electrical resistance of high-purity aluminum armature bars in Ohm·m

Temperature (T, K)	Sample 1	Sample 2	Sample 4
293	2.8×10^{-8}	2.7×10^{-8}	2.7×10^{-8}
77	3.0×10^{-9}	2.4×10^{-9}	2.5×10^{-9}
4.2	2.0×10^{-10}	2.5×10^{-10}	2.6×10^{-10}

The values presented in Table 4-1 are the average values of several resistances obtained at different current loads. Evaluation of Ohmic losses and determination of optimal filament diameters for minimal eddy current losses is carried out in Fig.4.18-4.20.

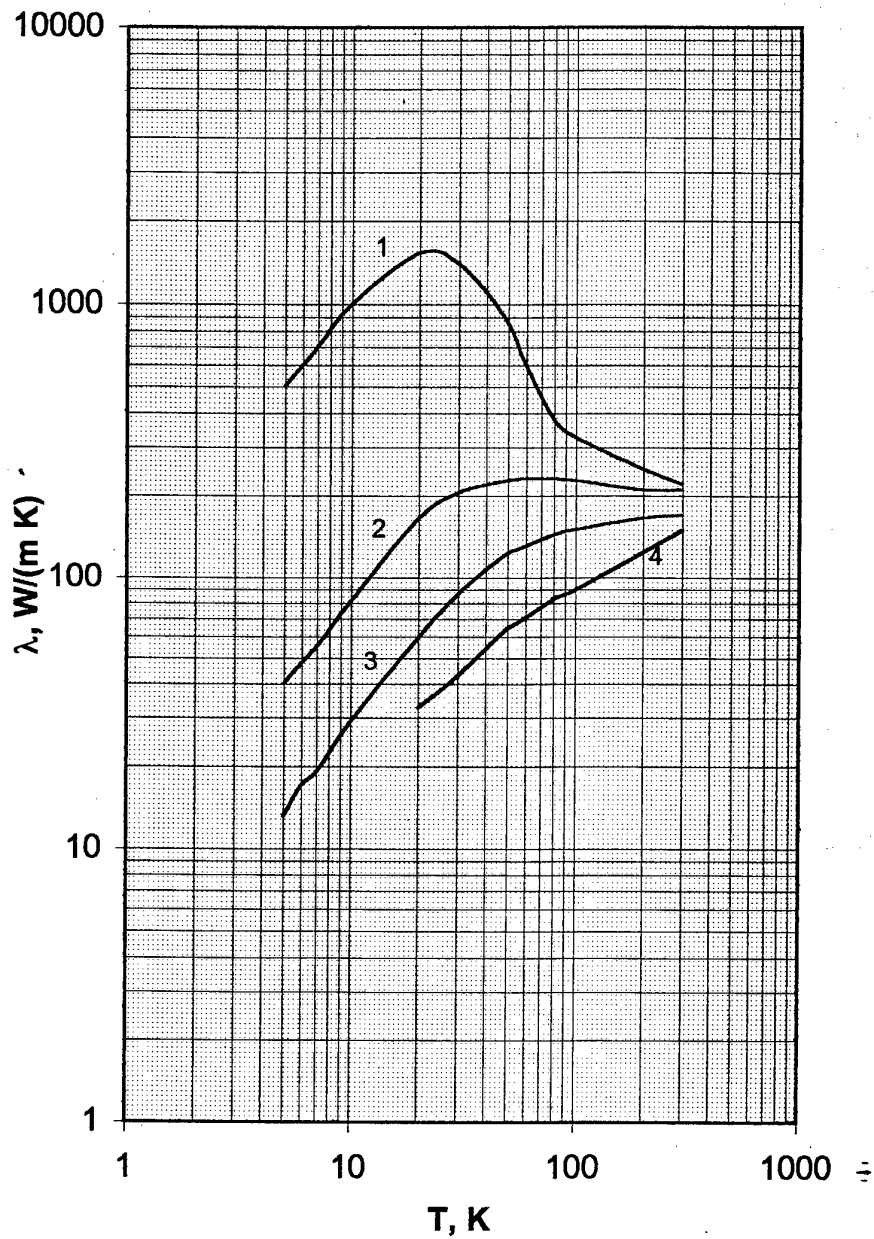


Fig. 4.16. Specific thermal conductivity of high-purity aluminum (1) and of different variants of Al-Mn alloys (2-4) as presented in technical literature.

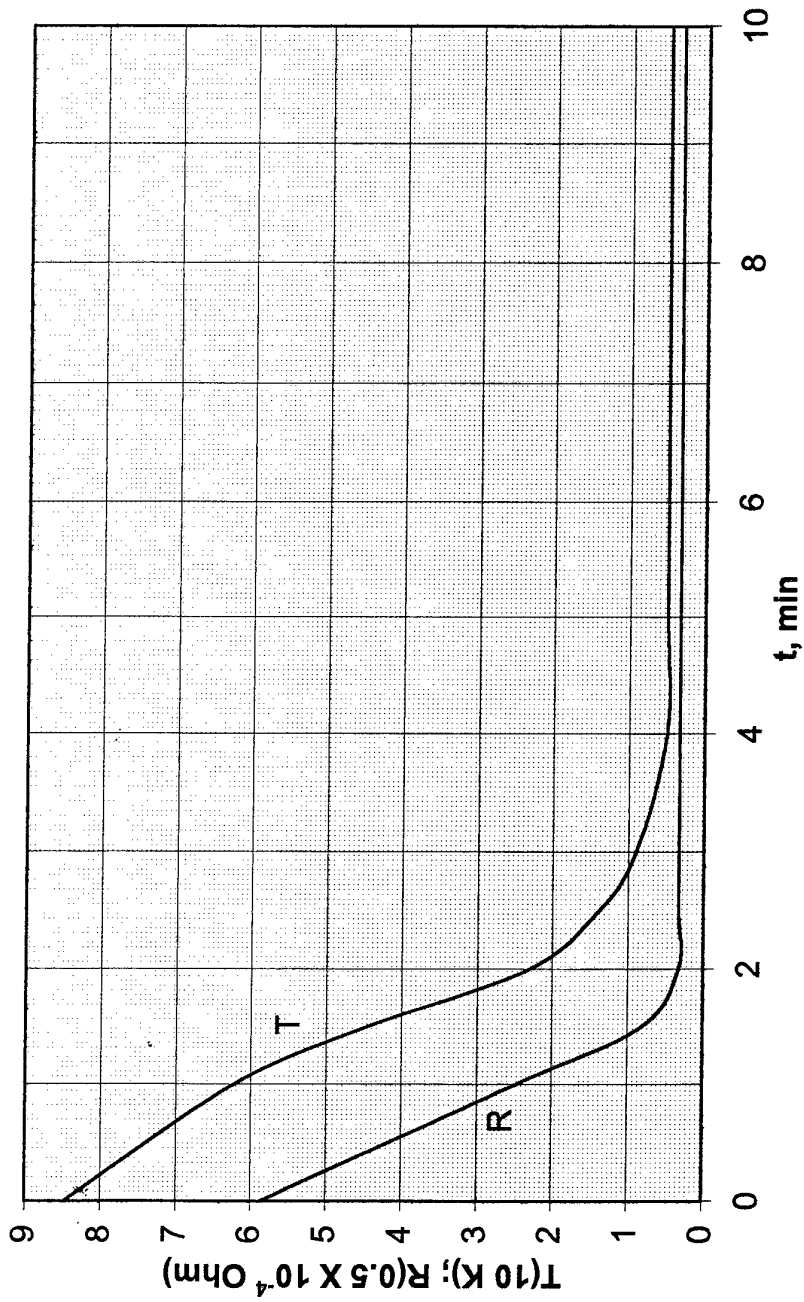


Fig.4.17. Variation of composite bar resistance and temperature during cryostat filling-in with liquid helium.

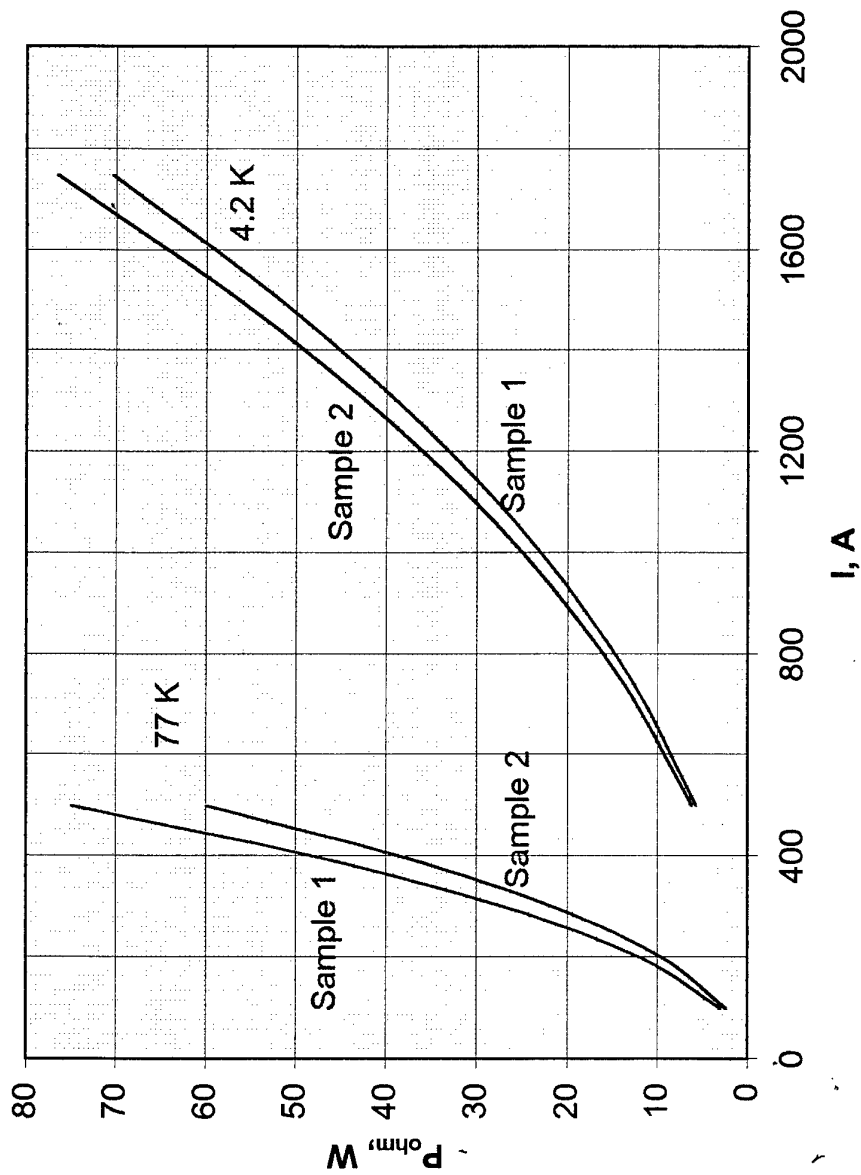


Fig.4.18. Ohmic losses in the armature bars manufactured of high-purity aluminum.

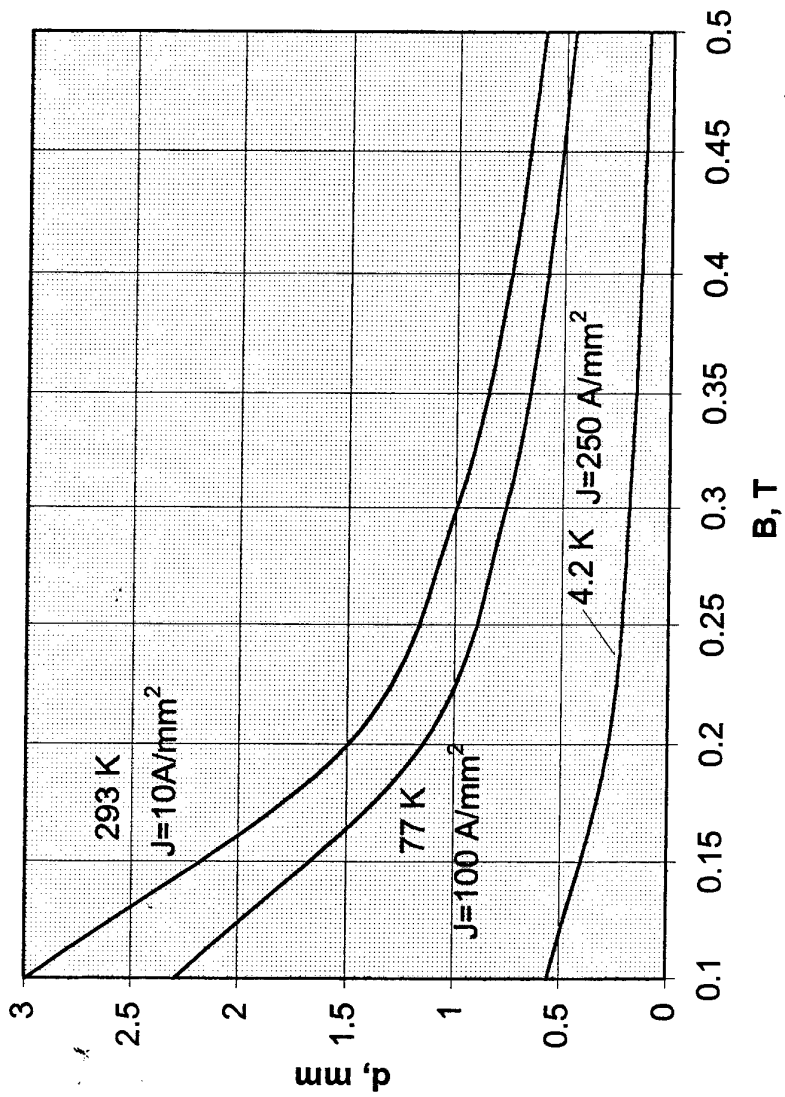


Fig.4.19. Optimal wire diameter for minimal eddy-current losses, $f=800$ Hz.

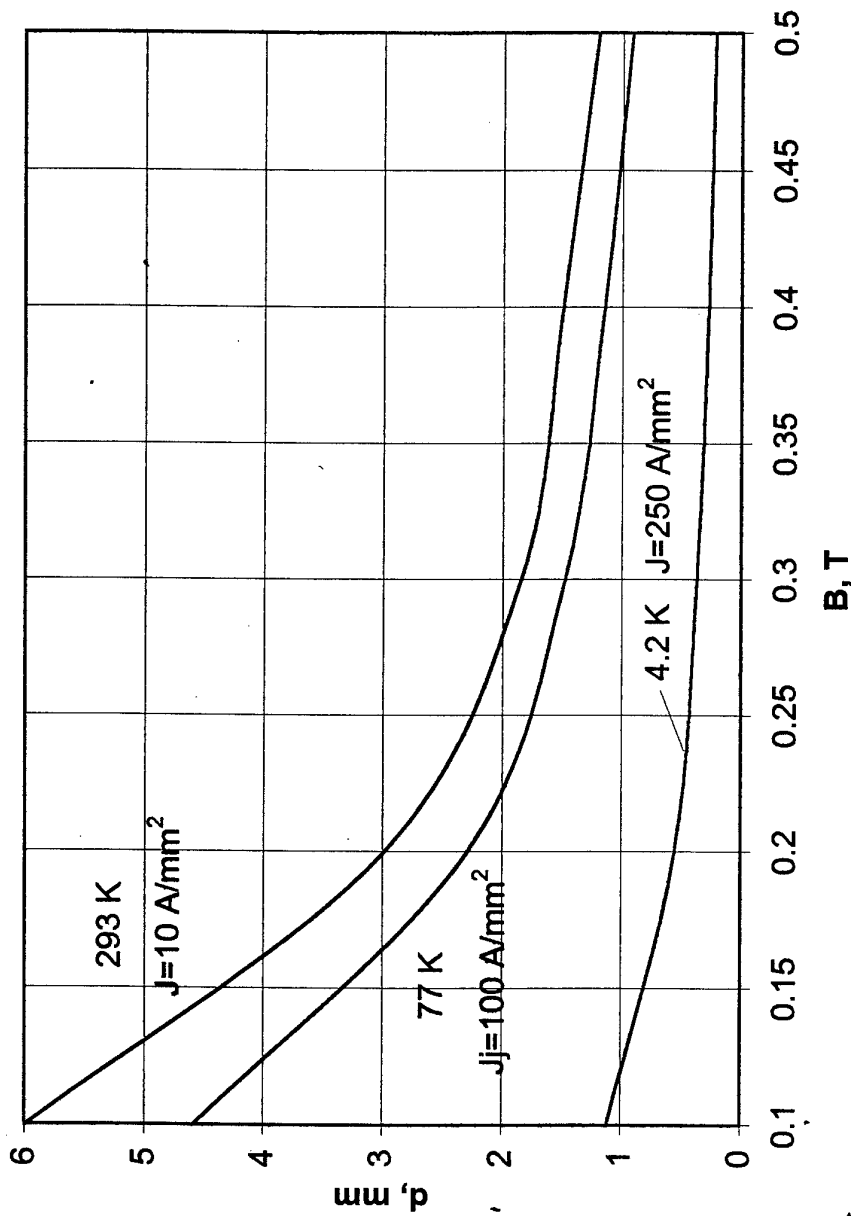


Fig.4.20. Optimal wire diameter for minimal eddy-current losses, $f=400 \text{ Hz}$.

5. EXPERIMENTAL INVESTIGATION OF THE DISC MODEL BARS

5.1. Specific features of heat conduction in multifilamentary wires

The Poisson equation for heat conductivity can be presented in general form as

$$l_x \frac{d^2 T}{dx^2} + l_y \frac{d^2 T}{dy^2} + l_z \frac{d^2 T}{dz^2} + q = 0. \quad (5.1)$$

In order not to mix up the presented below solutions with the one, given in Para.4.1, we here accept that

$$\lambda_y = 0; \lambda_z = 0 \quad (5.2)$$

and in accordance with the scheme presented in Fig.5.1 solve the equation

$$\lambda_x \frac{d^2 T}{dx^2} + q = 0. \quad (5.3)$$

The scheme (Fig.5.1) shows 1/2 of the bar length with the warm part positioned in the center of the bar.

The Ohmic losses in the unit volume of the armature bar are equal to

$$P_{ohm} = j^2 \rho dV = j^2 \rho S dx = \frac{I^2 \rho}{S} dx; \quad (5.4)$$

and eddy current losses may be determined as

$$P_e = \frac{1}{8} B^2 \gamma \omega^2 \frac{d^2}{4} S dx. \quad (5.5)$$

With the presented in Para 3 loss optimization we can accept that

$$P_{ohm} + P_e = 2P_{ohm},$$

The amount of heat, produced in the bar element dx , positioned on a distance x from the cold end of the half bar during the unit time interval depends on the amount of losses in the bar element and is equal to

$$(dq_x)_I = 2 \frac{I^2 \rho}{S} dx. \quad (5.6)$$

This heat is to be transferred to the bar cold end. The heat flux through the bar cross-section equals

$$q_x = -\lambda S \frac{dT}{dx}. \quad (5.7)$$

The difference of heat fluxes through the cross-sections x and $x + dx$ may be presented as

$$(dq_x)_\lambda = \left[-\lambda S \frac{d\left(T - \frac{dT}{dx} dx\right)}{dx} \right] - \left(-\lambda S \frac{dT}{dx} \right) = \lambda S \frac{d^2 T}{dx^2} dx. \quad (5.8)$$

In general the direction of heat flux in stationary mode is unknown, it depends on temperatures T_I and T_0 , and on the intensity of heat release. Nevertheless in each bar element the heat is to be balanced as:

$$(dq_x)_I + (dq_x)_\lambda = 0, \quad (5.9)$$

i.e.

$$\frac{d^2 T}{dx^2} + \frac{2I^2 \rho}{\lambda S^2} = 0 \quad (5.10)$$

We can thus obtain an expression for the temperature distribution $T=f(x)$ along the length of the half bar:

$$T = -\frac{2I^2 \rho}{\lambda S^2} \frac{x^2}{2} + C_1 x + C_2, \quad (5.12)$$

with C_1 and C_2 - constants of integration, determined from the boundary conditions, presented below.

In accordance with Fig.5.1 we have

$$\begin{aligned} T|_{x=l} &= T_1 = \text{const} , \\ T|_{x=0} &= T_0 = \text{const} . \end{aligned} \quad (5.13)$$

The integrating constants are then equal to:

$$C_2 = T_0 ; \quad C_1 = \frac{1}{l} \left[\frac{2I^2 \rho l^2}{\lambda A^2} + (T_1 - T_0) \right]. \quad (5.14)$$

As a result we can write down the following expression for the temperature distribution along the half bar:

$$T = -\frac{I^2 \rho}{\lambda S^2} x^2 + \left[\frac{I^2 \rho l}{\lambda S^2} + \frac{(T_1 - T_0)}{l} \right] x + T_0 . \quad (5.15)$$

The heat flux on the cold end of the half bar equals

$$q_0 = -I^2 \rho l^* + \lambda (T_1 - T_0) \frac{1}{l^*} , \quad (5.16)$$

where $l^* = \frac{l}{S}$.

Optimization of the adiabatic process in the bar means determination of the minimum of the function q_0 :

$$\frac{dq_0}{dl^*} = I^2 \rho - \lambda (T_1 - T_0) \frac{1}{l^{*2}} = 0 \quad (5.17)$$

with determination of the optimal parameter

$$l_{opt}^* = \frac{1}{I} \sqrt{\frac{\lambda (T_1 - T_0)}{\rho}} \quad (5.18)$$

or optimal co-relation for the bar geometry and current loads:

$$j l = \sqrt{(T_1 - T_0)} \frac{\lambda}{\rho} . \quad (5.19)$$

The heat flux to the cryocoolant for the unit current in the bar equals

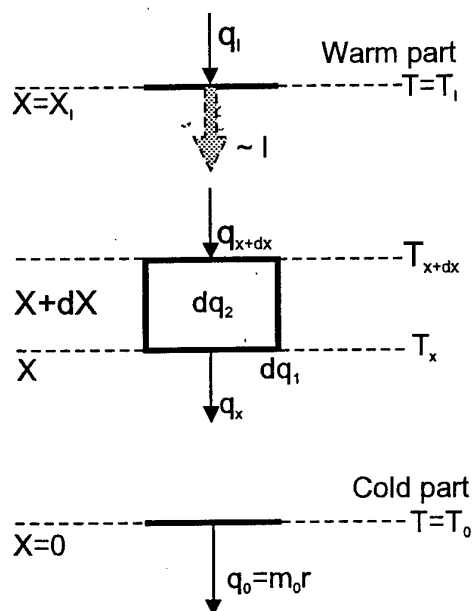


Fig.5.1. Principal scheme for calculations of heat behavior of the armature bar cooled by axial heat conduction.

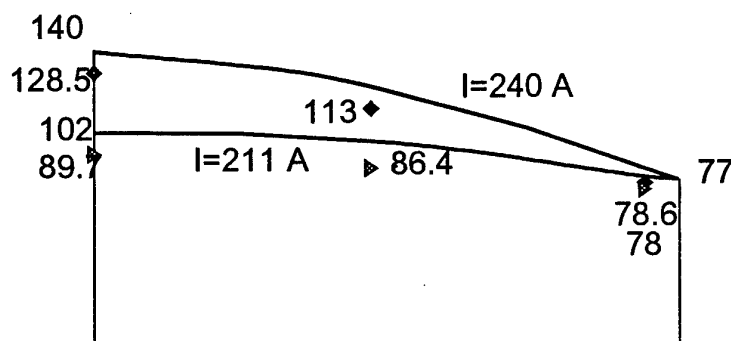


Fig.5.2. Calculated temperature variation in K along the armature half bar length with experimental points (composite high-purity aluminum sample).

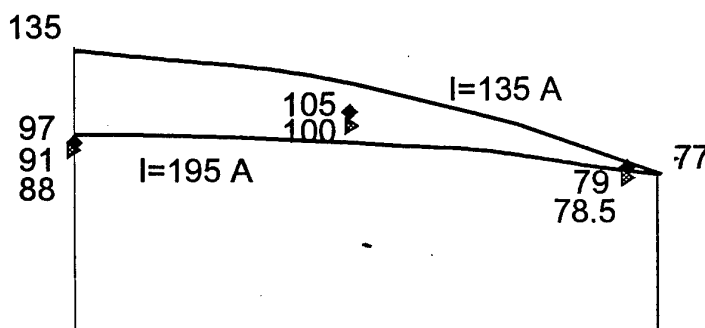


Fig.5.3. Calculated temperature variation in K along the armature half bar length with experimental points (high-purity aluminum sample).

$$\frac{q_{o \min}}{I} = \sqrt{\lambda \rho (T_i - T_o)} . \quad (5.20)$$

The presented formulas (5.4) - (5.20) refer to the heat behavior of the bar fed by AC, when the loss amount is determined by the components appearing under AC conditions.

In case of the experiment being discussed the bar was fed by DC and there were present only Ohmic losses. Then we can write down the expression for the temperature distribution in the experimental armature bar:

$$T = -\frac{I^2 \rho x^2}{\lambda S^2 2} + \left[\frac{I^2 \rho l}{2\lambda S^2} + \frac{(T_i - T_o)}{l} \right] x + T_o \quad ; \quad (5.21)$$

The heat flux on the cold end of the half bar under the experiment conditions equals

$$q_o = -\frac{I^2}{2} \rho l^* + \lambda (T_i - T_o) \frac{1}{l^*} , \quad (5.22)$$

and as a result we have the following expressions for the optimized bar parameters:

$$l_{opt}^* = \frac{1}{I} \sqrt{\frac{2\lambda}{\rho} (T_i - T_o)} , \quad (5.23)$$

$$j l = \sqrt{\frac{2\lambda}{\rho} (T_i - T_o)} , \quad (5.24)$$

$$\frac{q_{o \min}}{I} = \sqrt{2\lambda \rho (T_i - T_o)} . \quad (5.25)$$

The presented equations (5.21) - (5.25) were used when pre-calculating the bar experimental data accounting for the temperature difference due to presence of the wire enamel insulation and thin layer of epoxy:

$$\theta = \frac{j^2 \rho b \delta}{2\lambda} , \quad (5.26)$$

where λ_i is thermal conductivity of the insulating layers, and for the following relation

$$\frac{\rho}{\lambda} = \frac{(T_x - T_0) - (T_l - T_0) \frac{x}{l}}{\frac{I^2 x}{2S^2} (l - x)} \quad (5.27)$$

with λ of high-purity aluminum wire and the matrix material being determined in accordance with the Fig.4.16 by subdividing the armature bar into portions with constant temperature. Comparison of this data with experimental one is presented in Fig.5.2-5.3.

5.2. Armature bar cooling by means of heat conductivity

Aluminum armature winding bars with thermal insulation and indirect cooling system were investigated on a specially built double-sided model (Fig. 5.4). The model was a disk with the slots milled on both flat surfaces, wherein the aluminum bars were laid. For indirect cooling system studying, the bars were covered with temperature-insulating liners formed of asbestos that were held in place by bolted covers. Bar temperature was measured by thermoresistors located under the temperature-insulating liners. High-accuracy low-temperature thermoresistors of TBO-0.125 type were used for investigations.

Figures 5.5 illustrates the elements of the disc-type armature bar model. Shown in Fig.5.6 are the TBO-0.125 type thermoresistors prepared to be installed into the model. Fig. 5.7-5.8 presents the disc model prepared for the low temperature experiments and an enlarged view of the model after the low-temperature tests.

Both high-purity aluminum bars and bars of aluminum composite were subjected to testing. Bar surfaces were thermally insulated from environment, the heat being evacuated due to bar material heat conductance to current lead assemblies which were washed-over by coolant.

The experiments were carried out at temperature of liquid nitrogen, liquid helium and at intermediate temperatures with gas cooling. The parameters registered in the course of liquid nitrogen tests for pure aluminum bar and composite wire are presented in Fig.5.9-5.10. Fig.5.11-5.14 gives the most typical graph sections at different current values. Temperature values measured by thermoresistors positioned on a thermally insulated bar section can also be found on these Figures. Temperature T_1 corresponds to the point located just near the current lead assembly cooled by the coolant, while T_3 corresponds to the middle of thermally insulated bar section, i.e. the point most distant from the coolant.

The fact that temperature T_2 obtained in the tests with pure aluminum bar happened to be higher than T_3 can be attributed to the loss of tightness by this

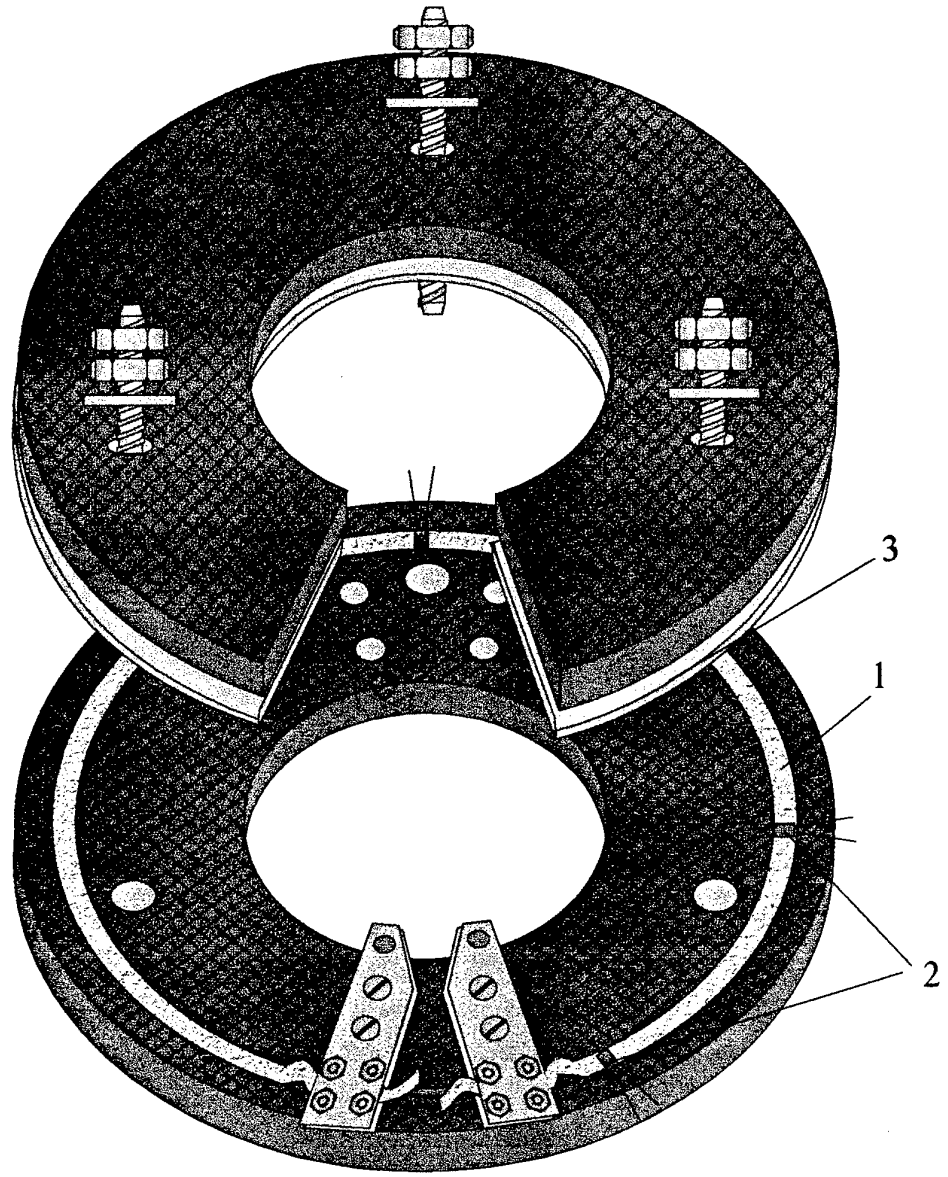


Fig. 5.4. The disk-type model of a stator bar.
1 - aluminum bar, 2 - thermoresistors, 3 - heat insulation

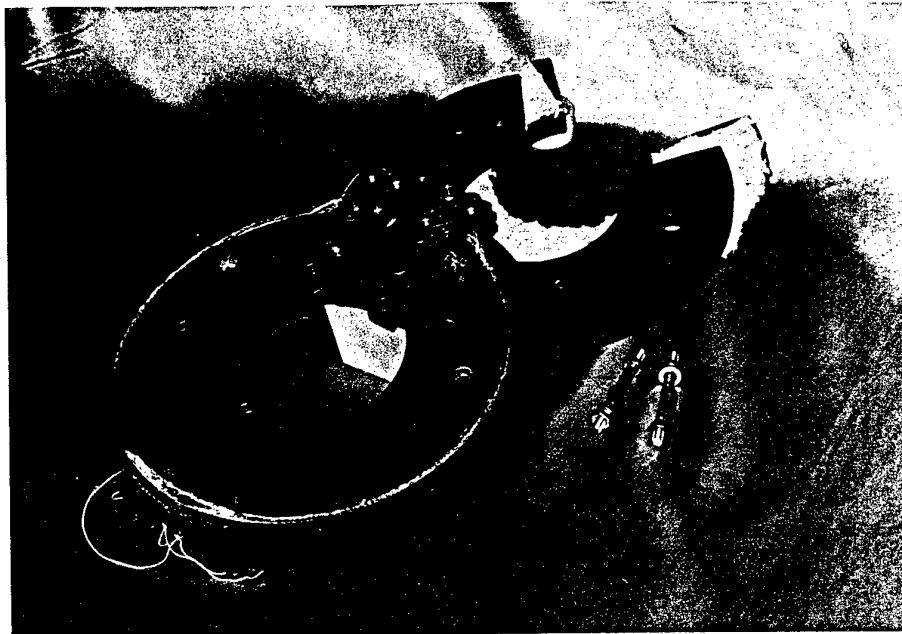


Fig.5.5. Elements of the disc-type armature bar model.

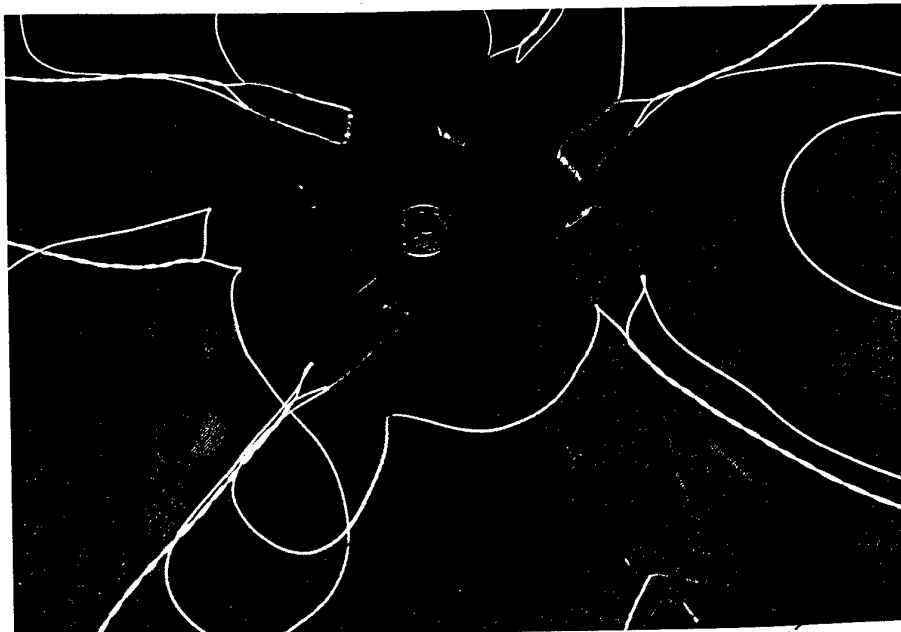


Fig.5.6 The TBO-0.125 type thermoresistors.



Fig.5.7. The disc model prepared for the low temperature experiments.

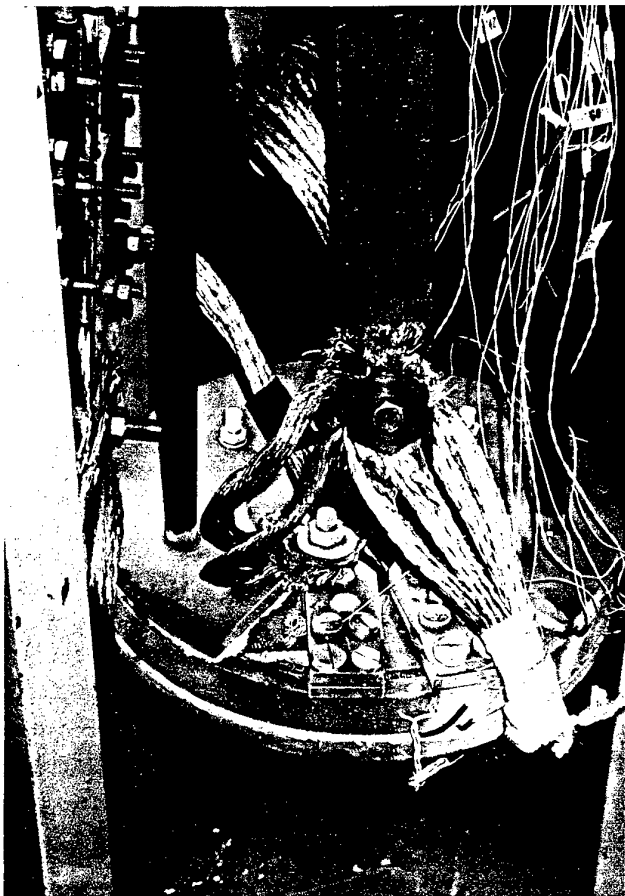


Fig.5.8. Enlarged view of the disc model after the low-temperature tests .

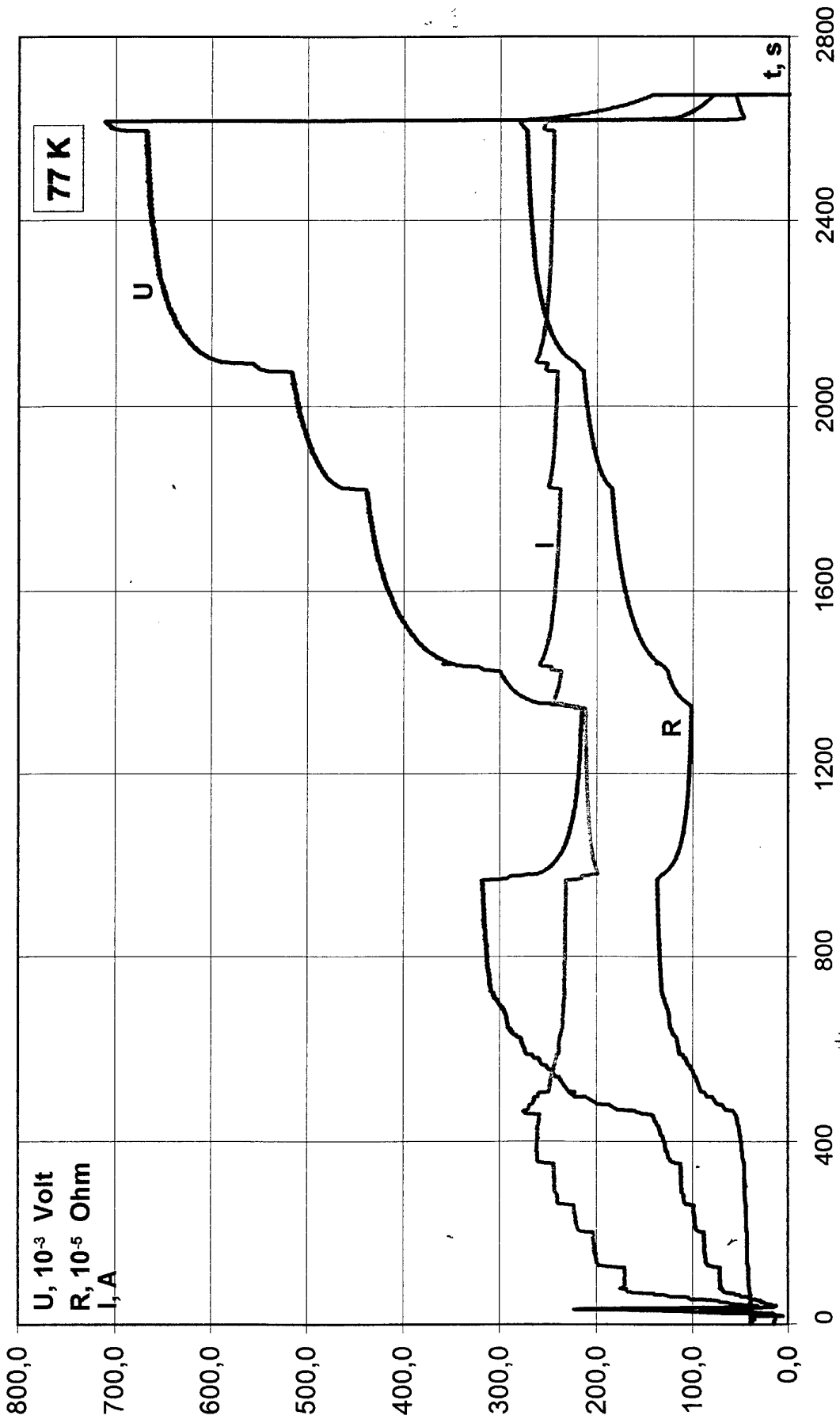


Fig.5.9. Registered composite bar parameter variation.

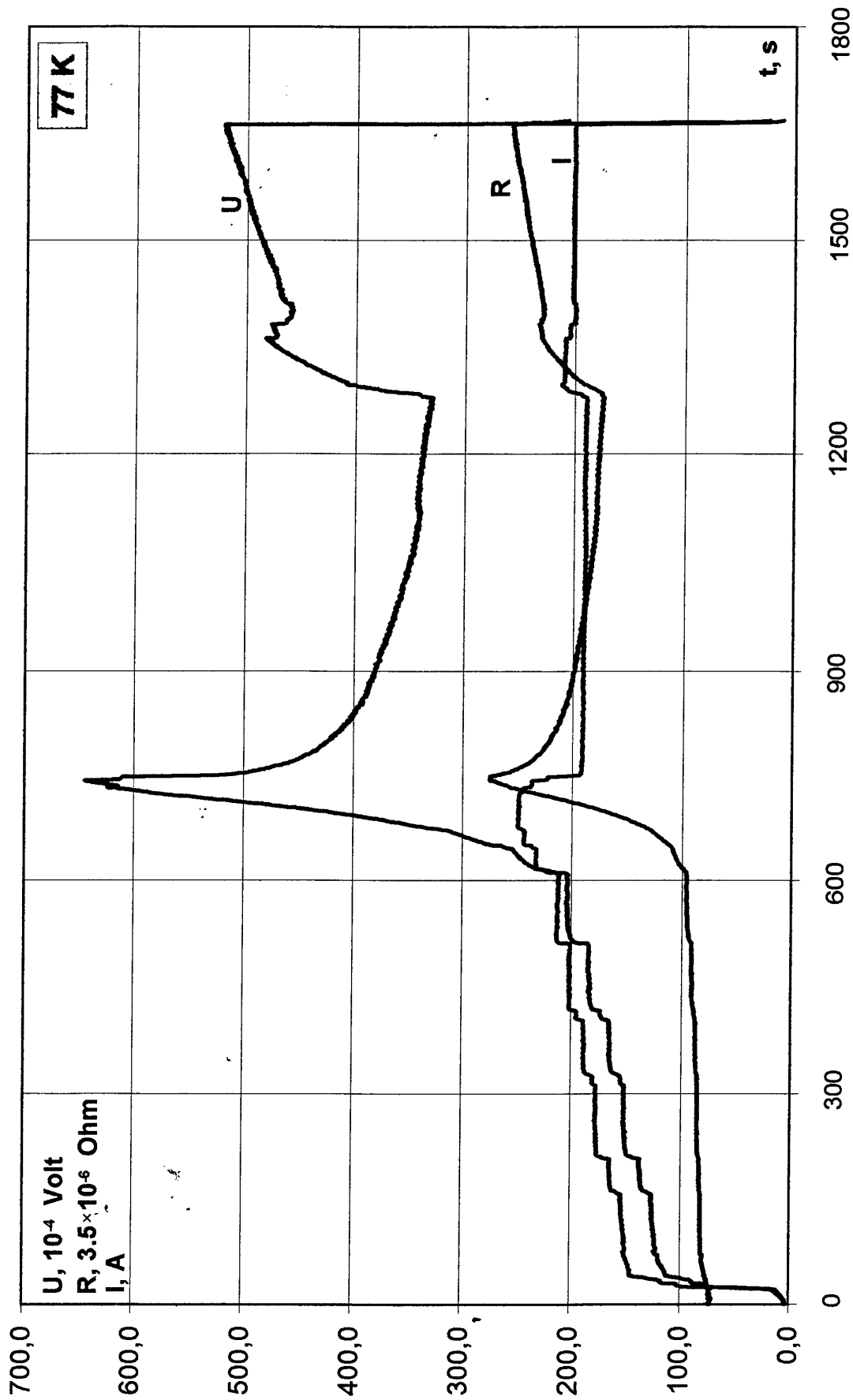


Fig.5.10. Registered high-purity aluminum bar parameter variation.

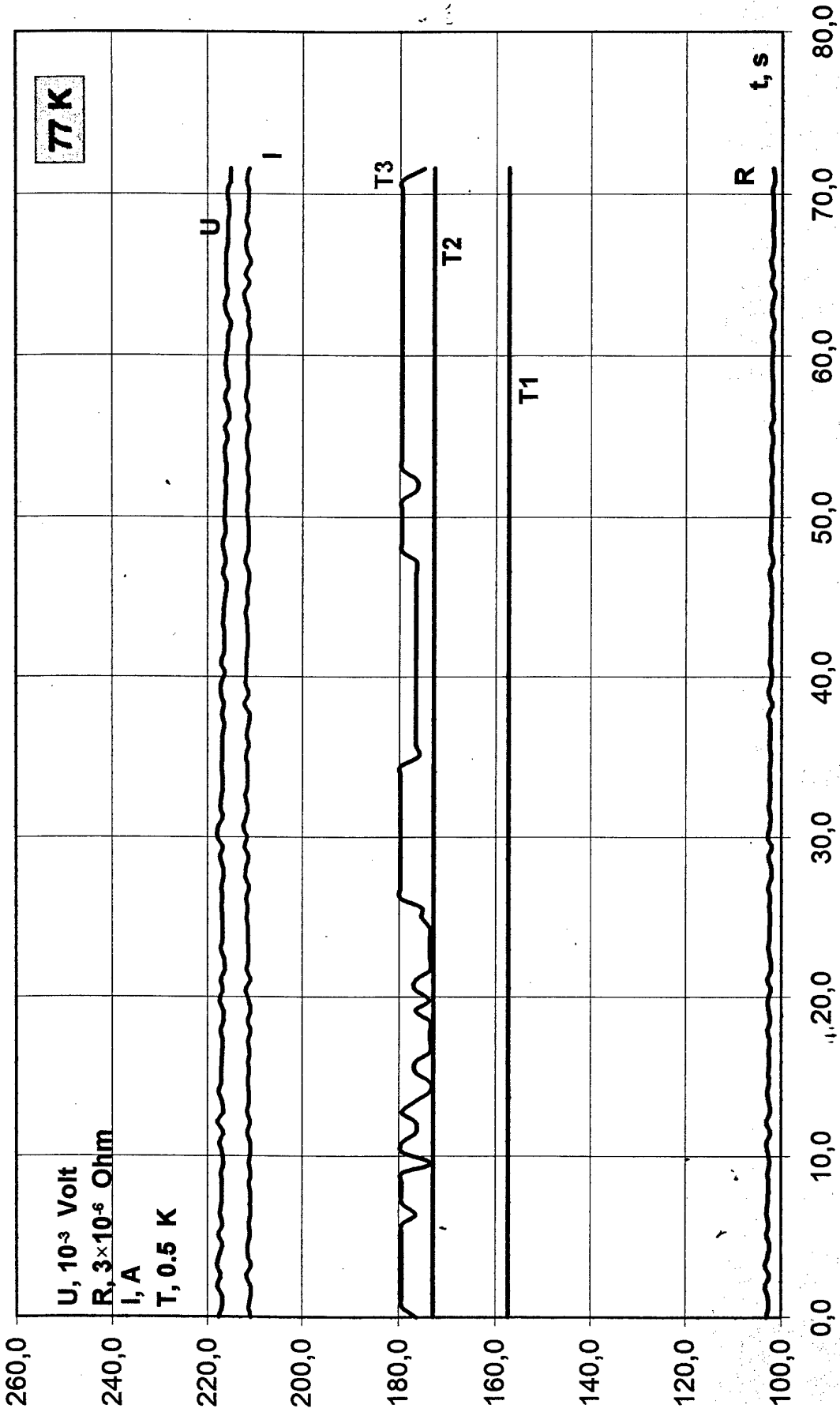


Fig. 5.11. Registered composite bar parameter variation at $I = 210$ A.

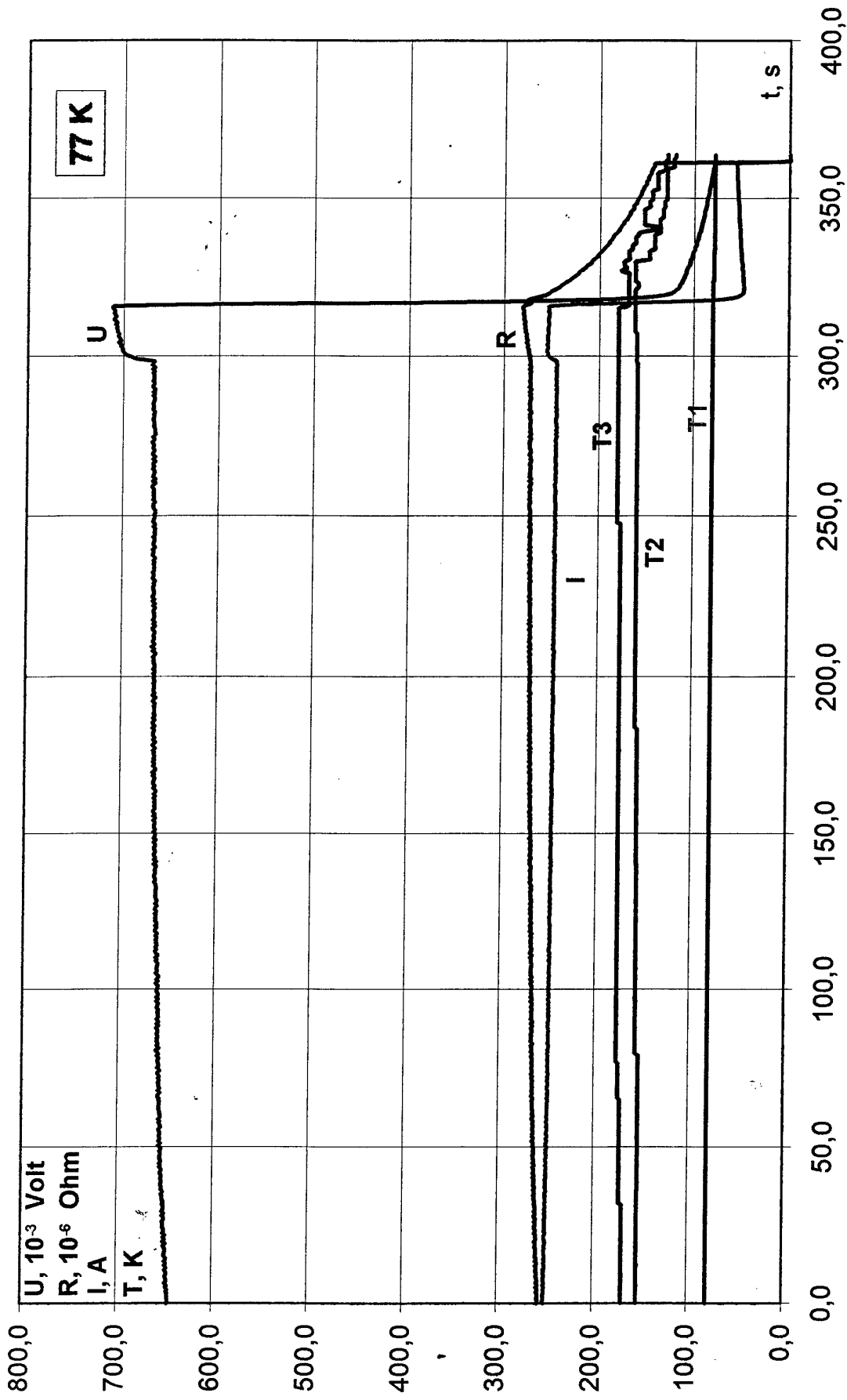


Fig.5.12. Registered composite bar parameter variation at $I = 250$ A prior to protection system action.

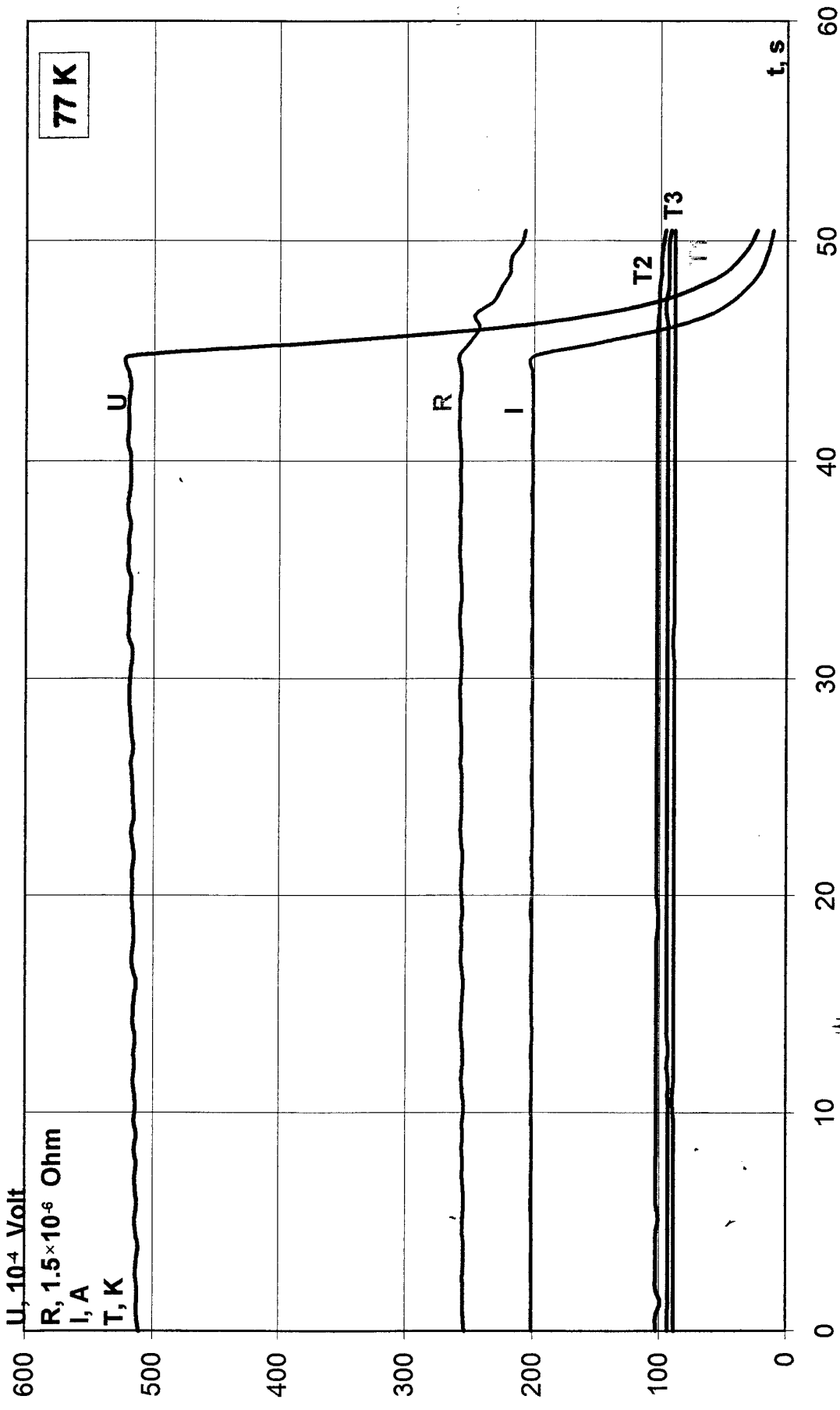


Fig.5.13. Registered high-purity aluminum bar parameter variation at $I = 200 \text{ A}$.

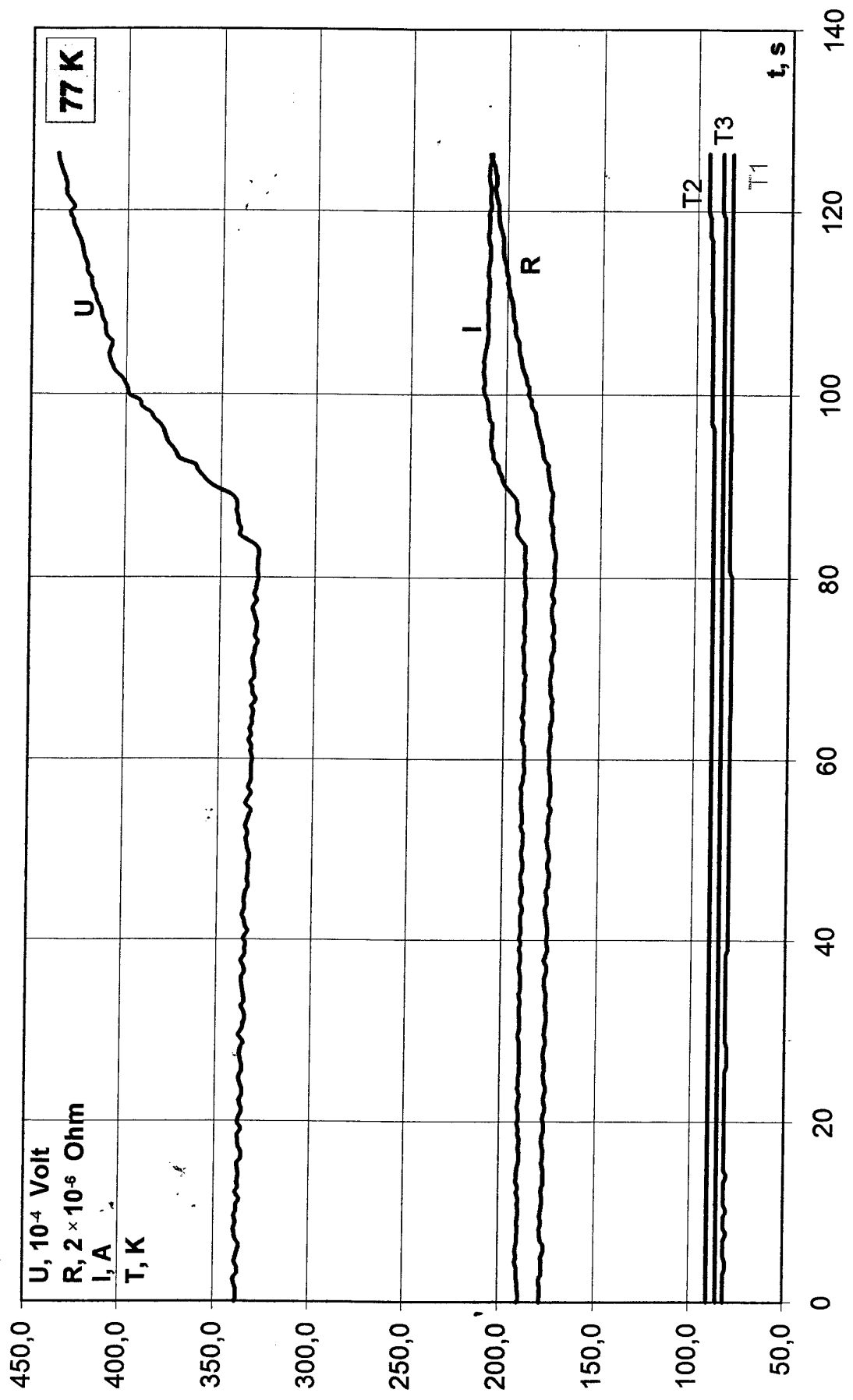


Fig.5.14. Registered high-purity aluminum bar parameter variation at $I = 190$ A and further current rise.

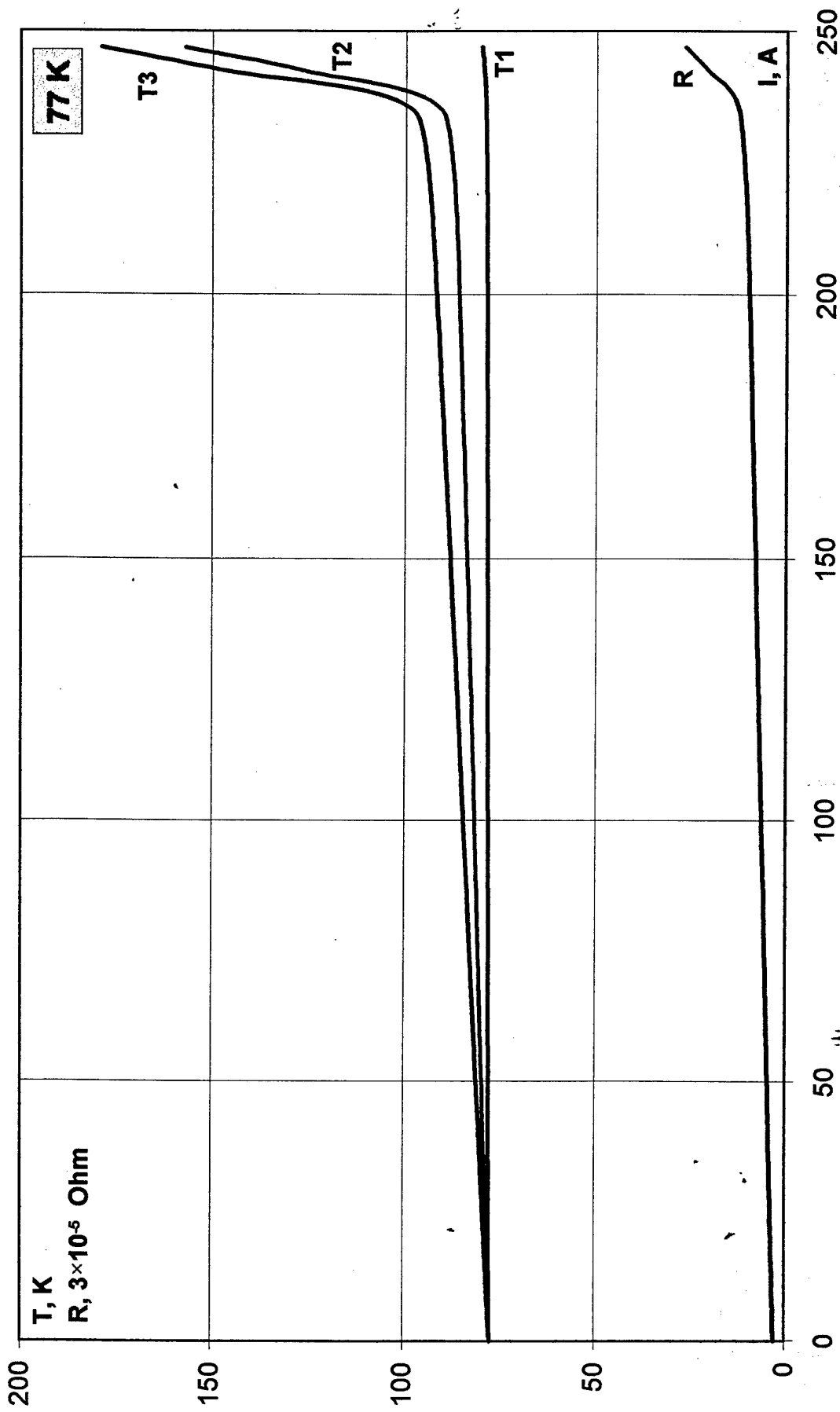


Fig. 5.15, a. Composite bar temperature and resistance as functions of current loading.

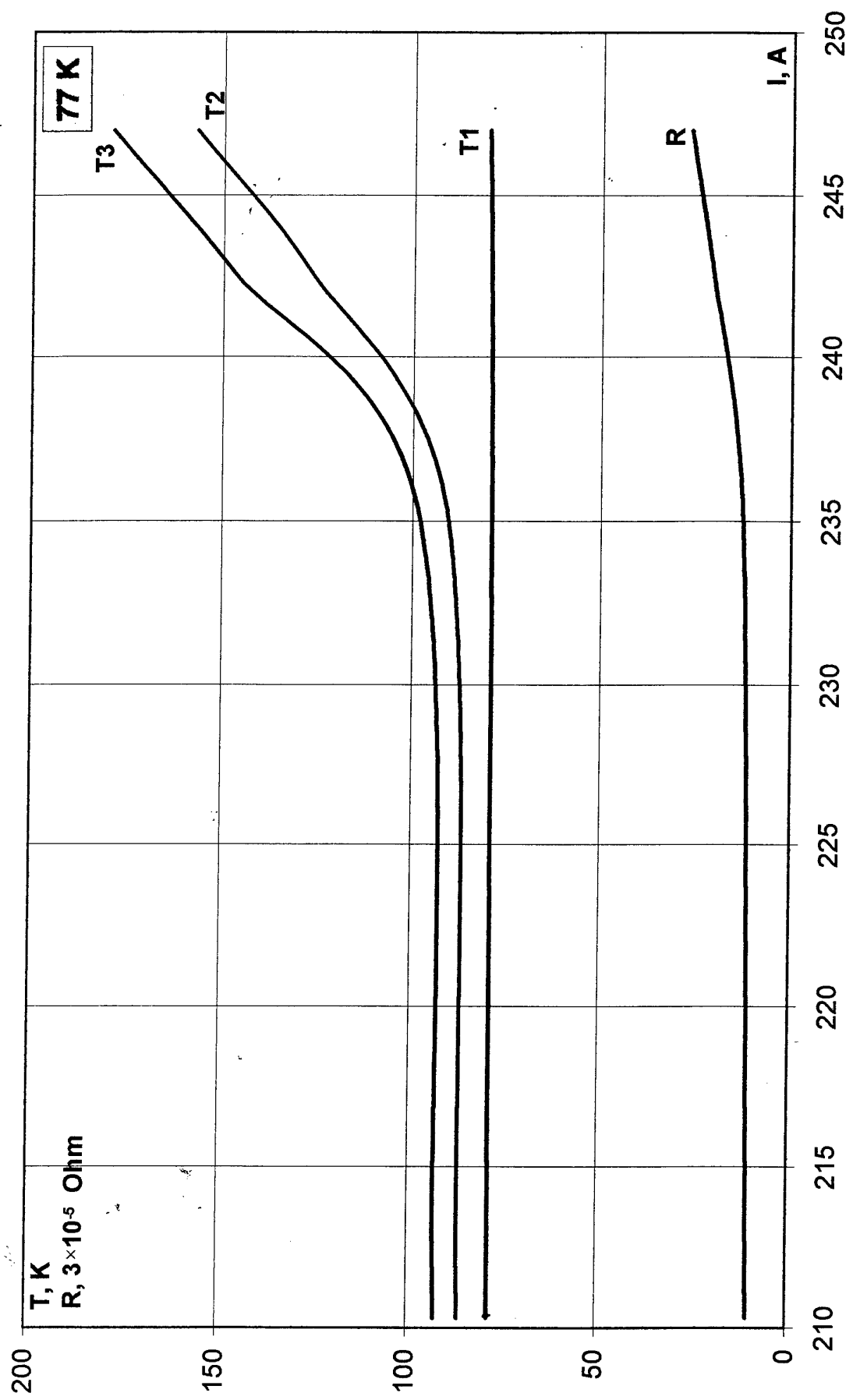


Fig.5.15, b. Composite bar temperature and resistance as functions of current loading.

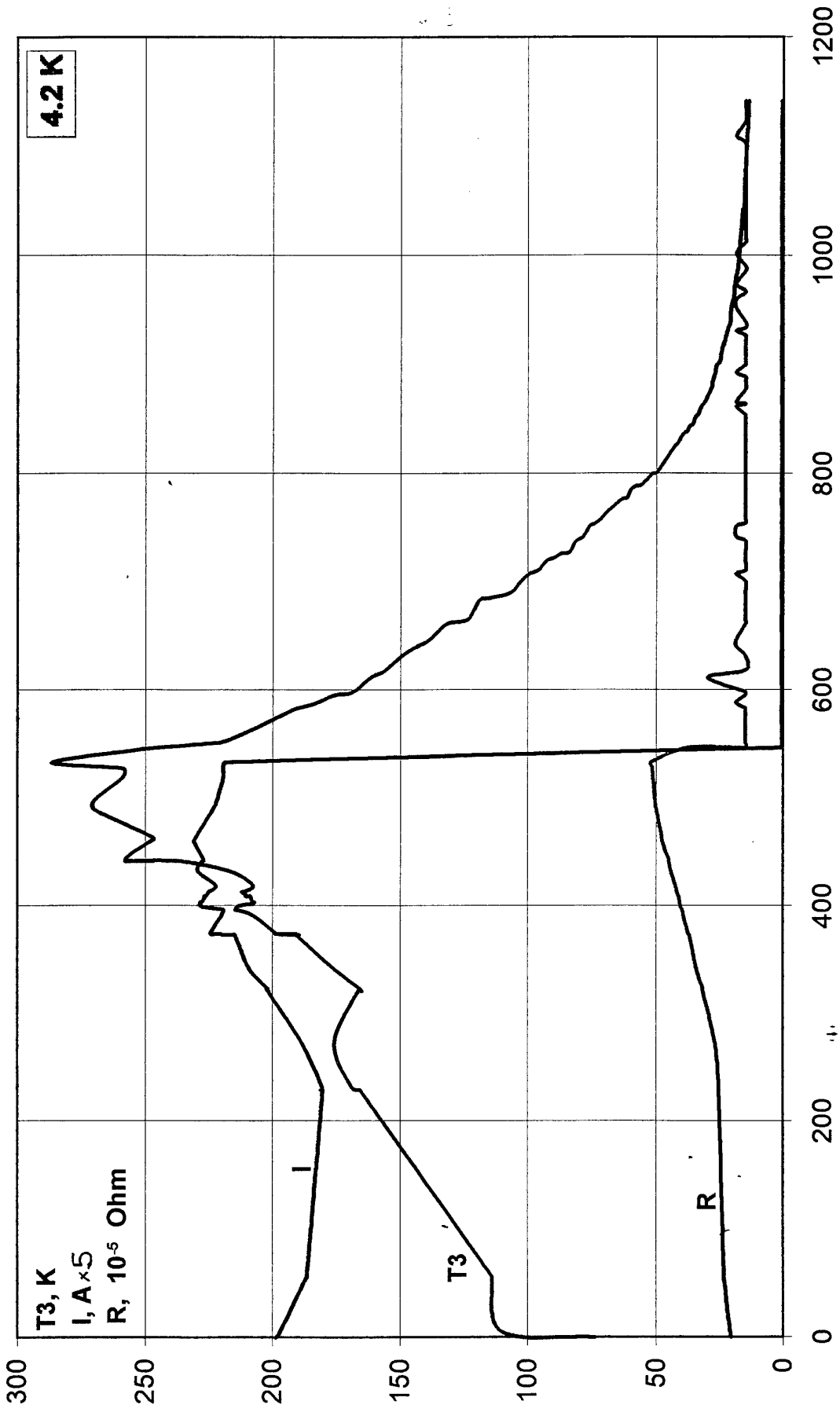


Fig.5.16. Parameter variation in liquid helium experiment on the bar of composite wire.

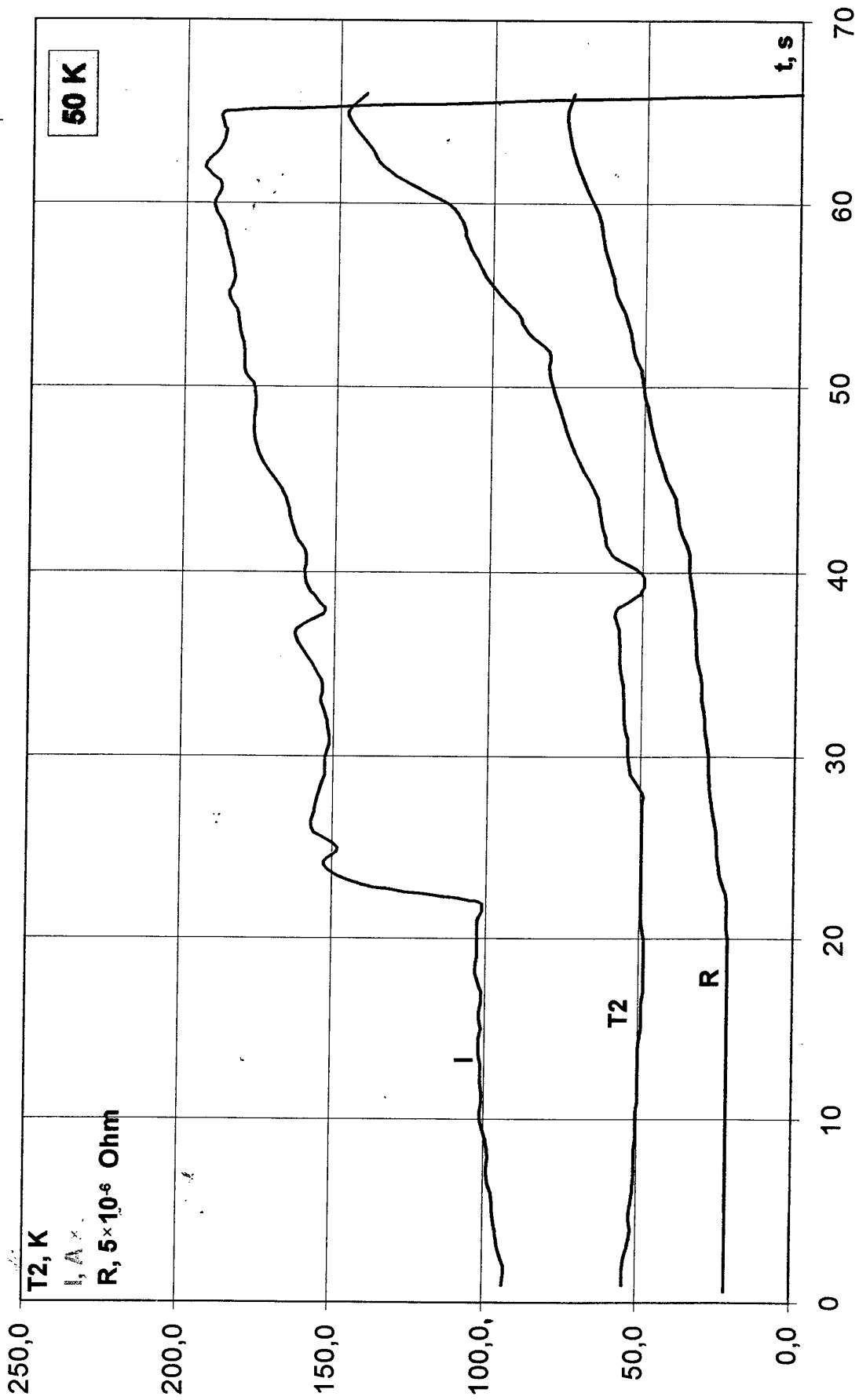


Fig.5.17. Parameter variation in the experiment on high-purity aluminum bar with gas cooling.

bar section. Fig.5.15 *a* and *b* shows the pattern of temperature variation on the thermally insulated bar section and resistance as a function of current. Fig.5.16 illustrates variation of temperature, resistance and current obtained in liquid helium tests for a thermally insulated section of composite bar. Presented in Fig.5.17 are the similar characteristics for high-purity aluminum bar at intermediate temperature. The coolant used in this experiment was gaseous He at temperature of about 50 K.

It is necessary to mention that the results of investigations carried out in accordance with the previous Contract on the bars with no thermal insulation and direct cooling system differ significantly from the present investigation results. Temperature of the directly cooled bars remained practically unchanged until current loading reached some critical point at which an avalanche growth of bar resistance and temperature occurred. But when studying the indirectly cooled bars we observed gradual growth of temperature with current loading increase. This is the evidence of a stabilizing effect of bar envelope and thermal insulation, which take up a considerable part of thermal loading from the bar itself due to their heat capacity.

5.3. Researches of a thermal behavior of aluminum armature bar for at pulse loads of different shape

High-power generators with high frequency of rotation are very often intended for operation in pulse mode. Therefore investigation of the armature bar behavior under the pulse current loads may present practical interest.

Investigation of aluminum armature bar behavior at pulse loads was performed using the programmed variation of the signals applied to the control power supply. Thermal condition of test samples at constant and varying loads were experimentally compared.

Experiments have been also conducted at varying loads with pulses of different duration. Figs. 5.18-5.19 demonstrate test results obtained for the bar of aluminum composite. During experiment (Fig.5.18) the load was increased gradually up to the moment of abrupt surge of sample resistance because of its heating-up. The initial stage of the experiment illustrated by Fig. 5.19 is in general similar to the previous one. But after the sample had been disconnected by the protection system because of an avalanche growth of its resistance it was subjected to a pulse load with the amplitude corresponding to the maximum current value causing the bar heating-up. From Fig.5.19 it can be seen that no heating is observed at pulse load application.

8

The experiments proved a strong dependence of bar behavior on a pulse load frequency. From Fig.5.20,a it is obvious (test with the bar of high-purity aluminum) that at load amplitudes close to the maximum ones and at a frequency about 0.2 Hz the bar resistance starts growing, what leads to an avalanche rise and results in power supply disconnection by a protection system.

The similar situation is depicted by Fig.5.20,b. If we gradually increase the pulse load amplitude, the bar resistance is found to grow quickly at the moment when the amplitude approaches its limiting values. Pulse load offers the possibility to reach higher current densities in the bar than those attained with DC. Fig.5.21 illustrates gradual current rise in a high purity aluminum bar. The avalanche-type growth of resistance is observed at 1850 A. But Fig.5.22 gives evidence that under pulse load of 0.3 Hz frequency the same bar shows no resistance growth even at the amplitude of 1900 A. However, at 0.2 Hz frequency and amplitude of pulse load equal to 2100 A (Fig.5.23) the quick rise (i.e. over one cycle) of resistance is manifested, and power supply is disconnected by a protection system.

The obtained results allow to conclude that in the pulse load mode of operation maximum current densities are higher than those obtained in steady state mode.

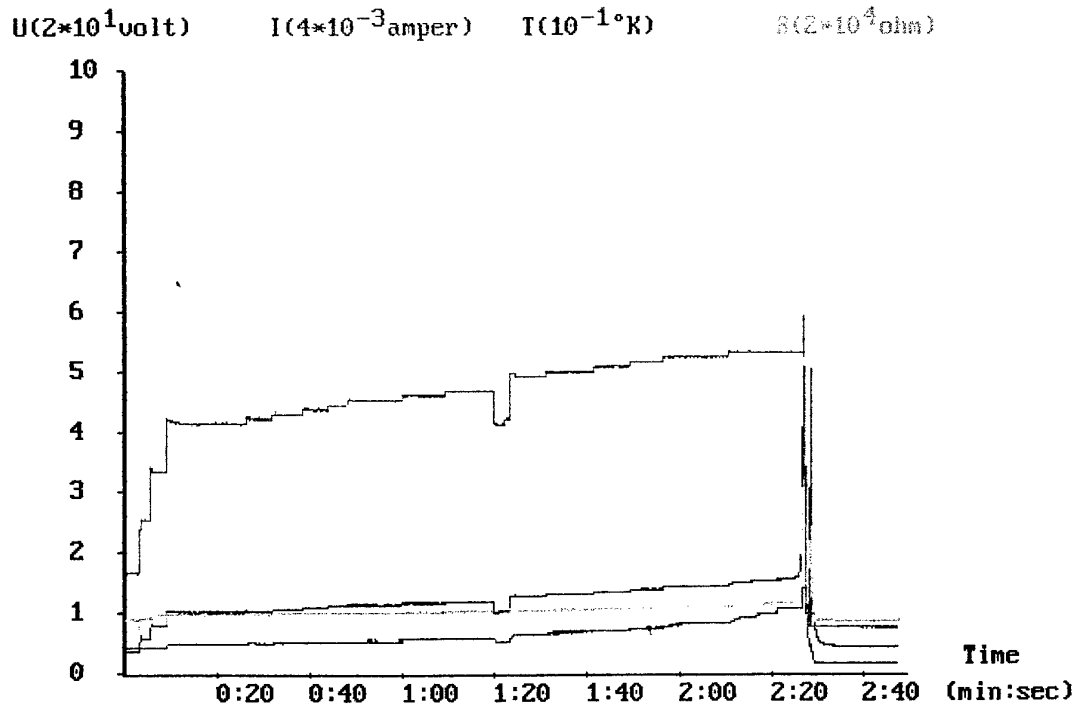


Fig.5.18. Experiment with current variation in the composit bar.

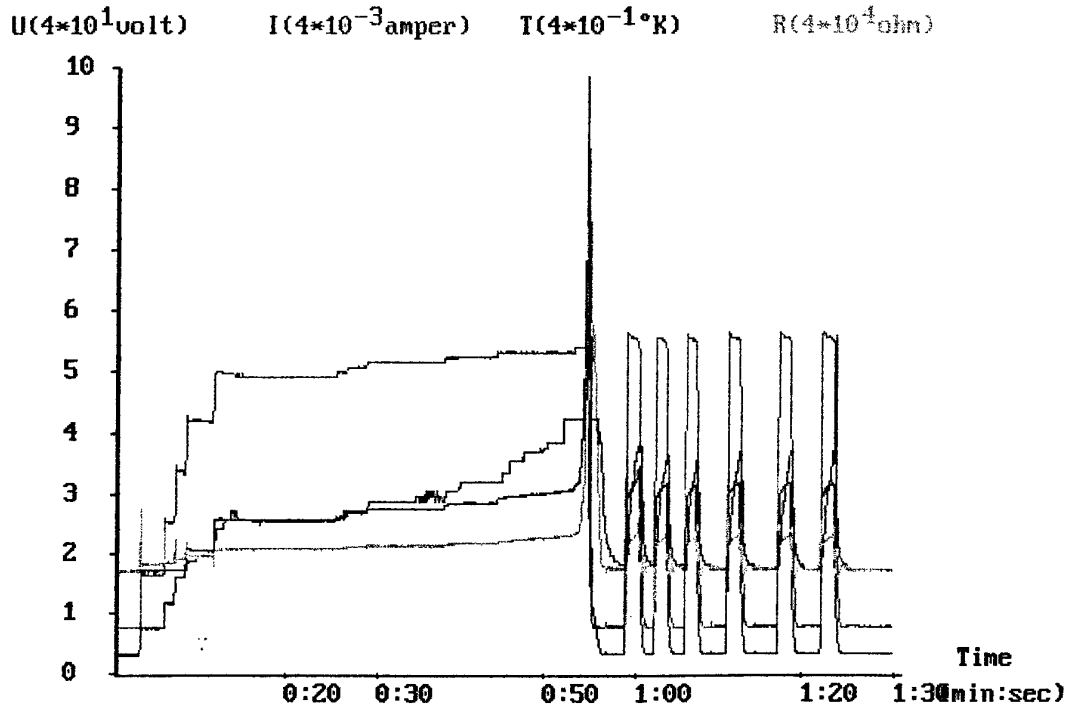


Fig.5.19. Experiment with current variation and pulse load in the composi ba

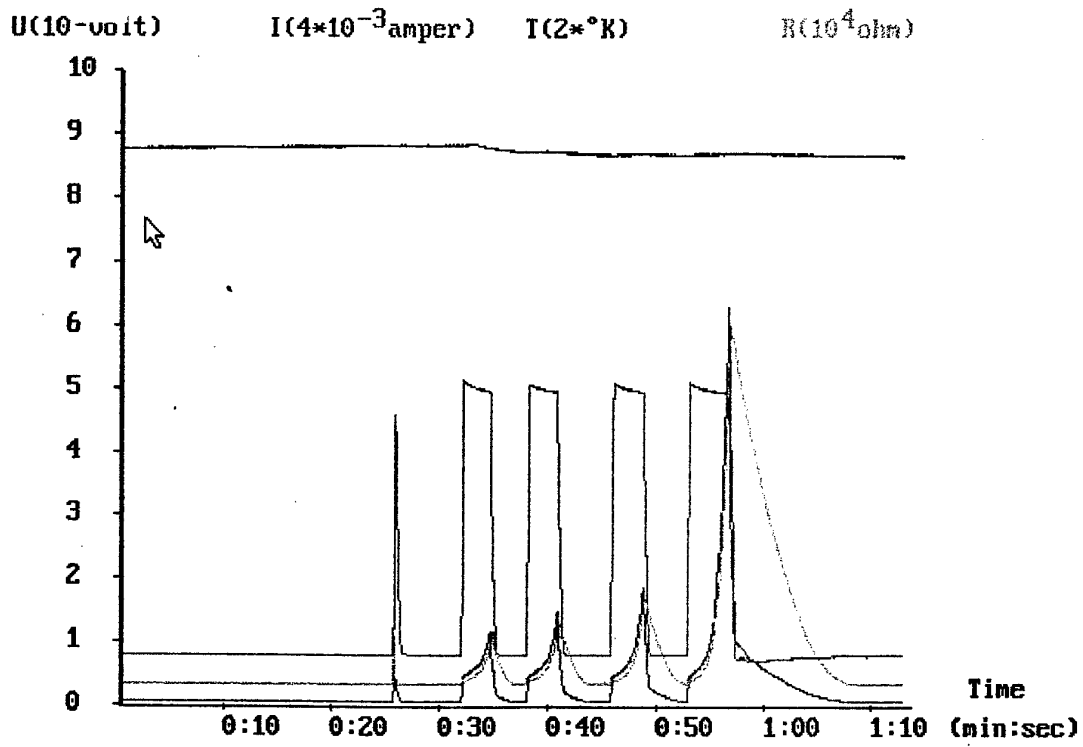


Fig.5.20, a. Experiment with pulse load in the high-purity aluminum bar.

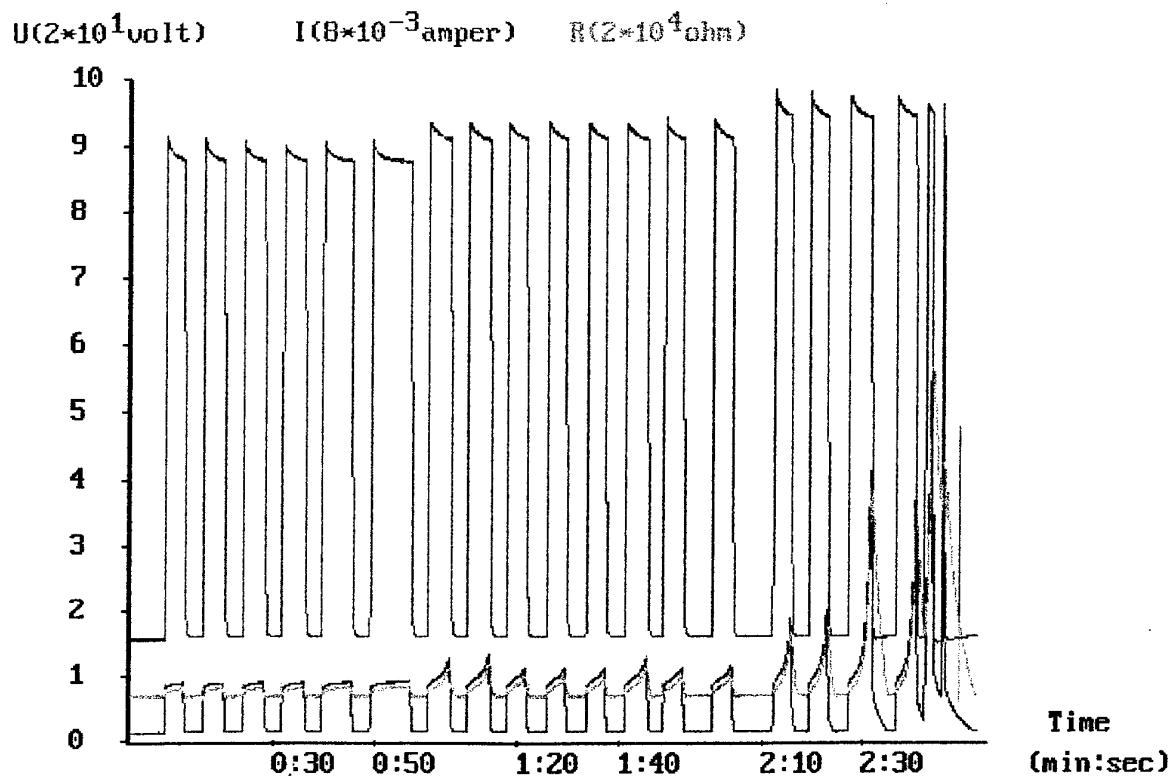


Fig.5.20, b. Experiment with pulse load in the high-purity aluminum bar.

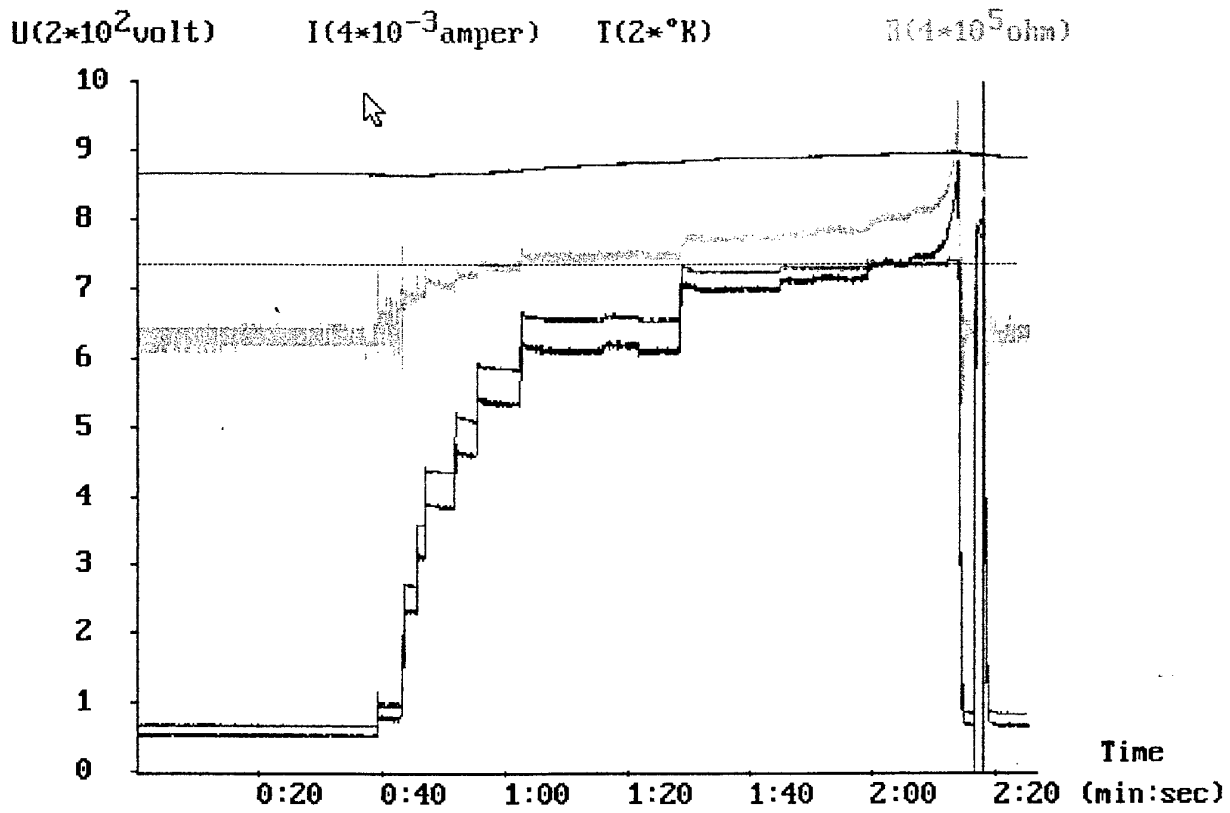


Fig.5.21. Current change in the high-purity aluminum bar with avalanche-type variation of resistance at 1850 A and after protection system operation.

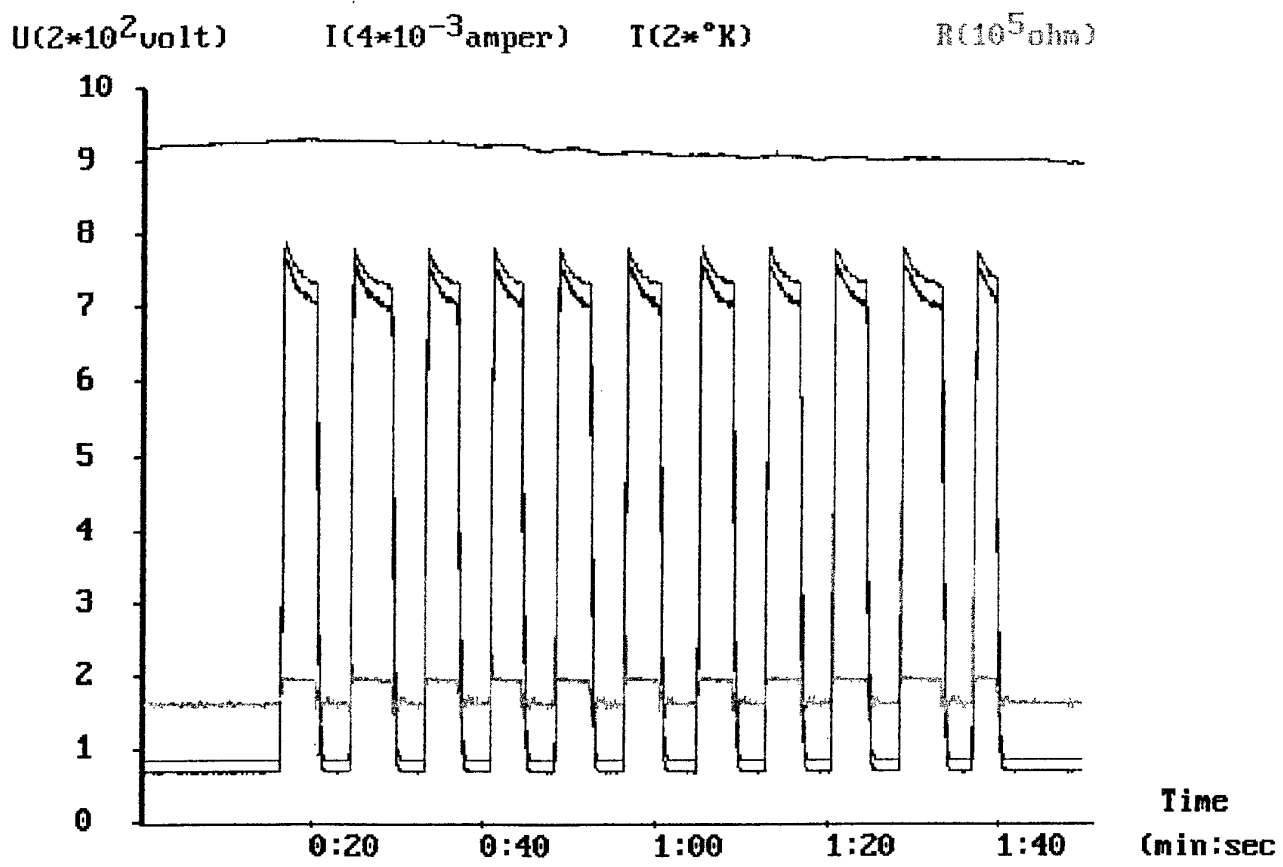


Fig.5.22. Experiment with pulse load of 0.3 Hz frequency in high-purity aluminum bar.

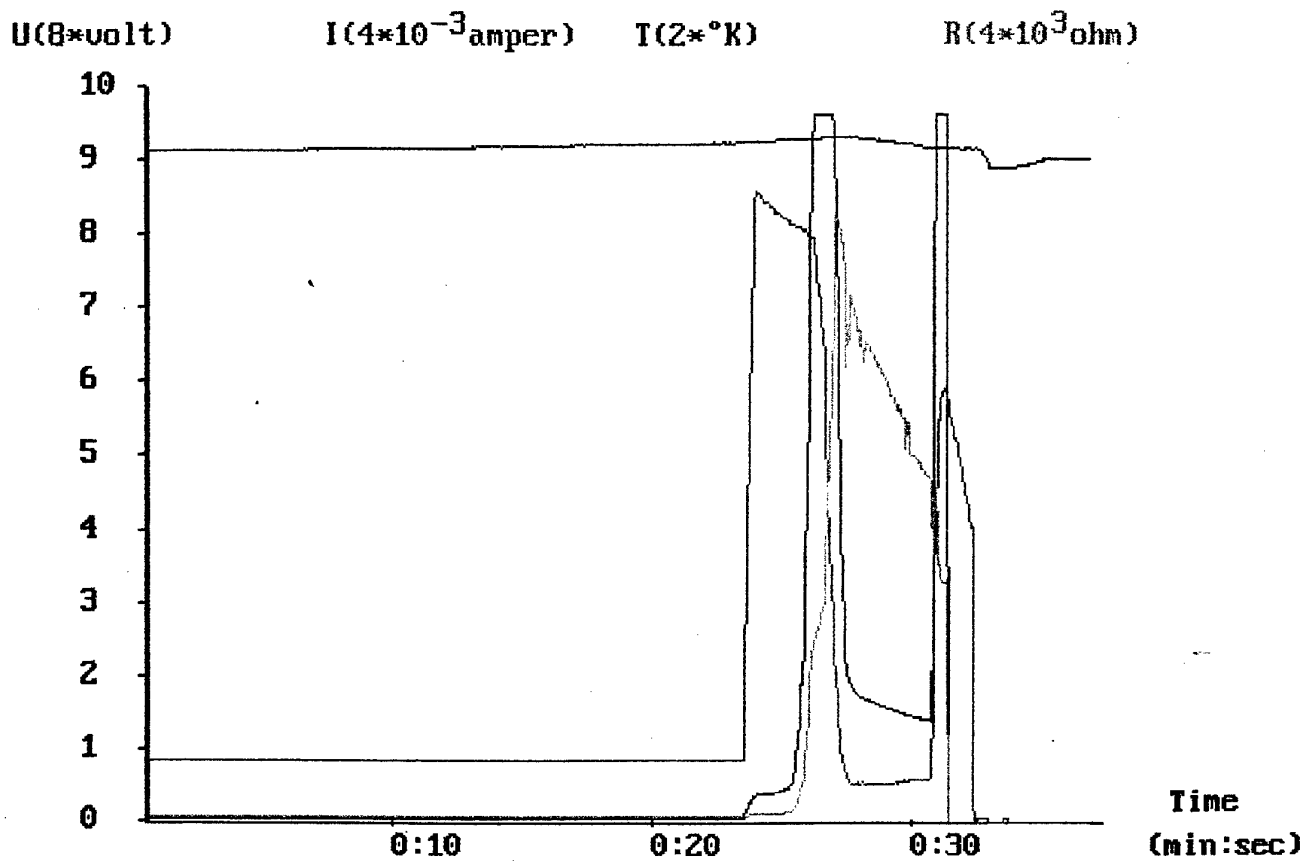


Fig.5.23. Experiment with pulse load and low frequency in high-purity aluminum bar.

CONCLUSIONS

1. There was developed a new technological process for the helical armature winding manufacturing with continuously wound phases and without any electrical joints along the phase length. The technological process is highly efficient for the windings manufactured of superconducting or hyperconducting rigid wires and tapes.
2. The technological process was verified by manufacturing of the helical armature winding model for the high rated alternator of 1-2 MVA class. The winding model has undergone a series of tests, including determination of parameters and 3D distribution of magnetic fields.
3. There was developed and manufactured a fraction of a helical armature winding of the 3-5 MW class alternator with the support structure of fibre glass laminate and armature bars of high-purity aluminum. The four armature bars are manufactured of composite high-purity aluminum wire with Al-Mn matrix, of high-purity aluminum strands and of electrotechnical copper strands (for comparison).
4. The test fixture with the helical armature winding fragment has undergone low temperature tests. There were registered the values of current, voltage and resistance and evaluation of the Ohmic and eddy current losses was carried out. The value of specific resistance of aluminum fibres in the composite high-purity aluminum bar equals $2 \cdot 10^{-10}$ Ohm·m and that of high-purity aluminum wires equals $2.5 \cdot 10^{-10}$ Ohm·m.
5. The successfully tested model with high-purity aluminum armature bars was sent to EOARD.
6. Because of complicated process of heat conduction in multifilamentary armature bars there were carried out theoretical and experimental investigations of the mode of armature bars cooling by axial heat conductivity. They have shown adequate co-relation of the calculations and tests. Moreover there was clarified an information about heat conductivity, presented in technical literature.
7. To evaluate heat behavior of the armature winding of an alternator, operating in a pulse load mode, there was carried out a series of tests on model armature bars. The tests have shown that the maximum current loads in the pulsed mode exceed the values obtained for the steady state modes. It allows to decrease the armature winding volume in case the alternator is to be used in pulse modes.

8. Theoretical and experimental investigations which were carried out allow to make a new significant step, approaching a highly reliable armature winding with minimal losses and improved cooling scheme.

REFERENCES

1. Criogenic aluminum armature bar for high power generators. Final report: Institute of Electrotechnical Problems. Department of Non Conventional Electrical Machines. August 1995.
2. Criogenic aluminum armature bar for high power generators. Preliminary report: Institute of Electrotechnical Problems. Department of Non Conventional Electrical Machines. October 1996.
3. Ph.G.Rutberg, L.I.Chubraeva, V.A.Tutaev et.al. 1 MW experimental hyperconducting alternator project. Preliminary evaluation. July 1993, 33 p.
4. Ph.G.Rutberg, L.I.Chubraeva, V.A.Tutaev et.al. Dual-use initiative high power laser assessments study - Prime electric power system. Final report: Institute of
5. Problems of Electrophysics of Russian Academy of Sciences. November 1993. Reference book on physical and technical bases of cryogenics. Ed. by M.P. Malkov. Moscow, Energie, 1973. (In Russian).
6. I.G.Kozhevnikov and L.A.Novitsky. Thermal and physical properties of materials at low temperatures. Reference book. Moscow, Mashinostroenie, 1982. (In Russian).
7. A.M.Arkharov, I.V.Marfenina and Eu.I.Mikulín. Cryogenic systems. Vol. 1. Moscow, Mashinostroenie, 1996. (In Russian).
8. I.A.Glebov, V.N.Shakhtarin and Yu.f. Antonov. Problem of the current leads to superconducting devices. Leningrad, Nauka, 1985. (In Russian).